

THE EFFECTS OF DARK ENERGY AND
BARYONS AND THEIR INTERPLAY ON THE
GROWTH OF STRUCTURE

Simon Pfeifer

A thesis submitted in partial fulfilment of the requirements of
Liverpool John Moores University
for the degree of
Doctor of Philosophy.
July 2020

Declaration

The work presented in this thesis was carried out at the Astrophysics Research Institute, Liverpool John Moores University. Unless otherwise stated, it is the original work of the author.

While registered as a candidate for the degree of Doctor of Philosophy, for which submission is now made, the author has not been registered as a candidate for any other award. This thesis has not been submitted in whole, or in part, for any other degree.

Simon Pfeifer
Astrophysics Research Institute
Liverpool John Moores University
IC2, Liverpool Science Park
146 Brownlow Hill
Liverpool
L3 5RF
UK

SEPTEMBER 2, 2020

Abstract

The discovery of the accelerated expansion of our Universe brought with it a new theoretical entity called dark energy. Within our standard model of cosmology, Λ CDM, this dark energy component is described by a cosmological constant with a small energy density that does not evolve with space or time. Attempts to attribute physical meaning to the cosmological constant have been unsuccessful, culminating in a collection of problems known as the “cosmological constant problem” and the “coincidence problem”. These have motivated alternative theories of dark energy that aim at relieving some of the theoretically unsatisfactory characteristics of the cosmological constant.

Over recent years, observational cosmology has made great leaps in constraining the parameters of the standard model of cosmology. However, with the increasing quantity and quality of data available, a few tensions between different observational probes have started to appear. These have only grown over time and are now of statistical significance. These tensions could have any of the following origins; they arise from unknown and unaccounted systematic errors in the data, from unknown errors in the theoretical modeling and/or from an incomplete model of cosmology. The latter possibility has added motivation for extending the standard model of cosmology, where alternate forms of dark energy are one of many available avenues.

The main aim of this work is to explore forms of dark energy with a greater degree of freedom than the cosmological constant. Specifically, dynamical dark energy (DDE) models which allow dark energy to evolve with time and are parametrised by two additional free parameters: w_0 and w_a . I investigate the current cosmological parameter constraints from a combination of observation data sets and devise a strategy to select

6 cosmologies of interest. I independently modified and ran a total of 12 simulations, evenly split between collisionless and hydrodynamic simulations.

Since dark energy affects the expansion history, geometric probes, such as Type Ia supernovae and baryon acoustic oscillations, can constrain the dark energy parameters in a conceptually straightforward manner. However, changes to the expansion history also affect the growth of structure which could make large-scale structure (LSS) statistics potentially powerful and complementary probes. The first part of this work investigates the effect that these cosmologies have on a variety of LSS statistics using large cosmological hydrodynamical simulations. I find that DDE can affect the clustering of matter and haloes at the $\sim 10\%$ level, which should be distinguishable with upcoming large-scale structure surveys. DDE cosmologies can also enhance or suppress the halo mass function (with respect to Λ CDM) over a wide range of halo masses. The internal properties of haloes are minimally affected by changes in DDE, however.

The second part of this work investigates the separability of the cosmology and baryonic physics. I quantify to what extent these two processes affect each other, or in other words, how correlated they are. I show that the impact of baryons and associated feedback processes is largely independent of the change in cosmology and that these processes can be modelled separately to typically better than a few percent accuracy.

Publications

In the course of completing the work presented in this thesis, the following papers have been submitted for publication in a refereed journal:

Simon Pfeifer, Ian G. McCarthy, Sam G. Stafford, Shaun T. Brown, Andreea S. Font, Juliana Kwan, Jaime Salcido and Joop Schaye. The BAHAMAS project: Effects of dynamical dark energy on large-scale structure. *arXiv e-prints*, art. arXiv:2004.07670, April 2020, *submitted to MNRAS*

Sam G. Stafford, Ian G. McCarthy, Rober A. Crain, Jaime Salcido, Joop Schaye, Andreea S. Font, Juliana Kwan and **Simon Pfeifer**. The BAHAMAS project: Effects of a running scalar spectral index on large-scale structure. *MNRAS*, *in press*, art. arXiv:1907.09497, Jul 2020

Shaun T. Brown, Ian G. McCarthy, Benedikt Diemer, Andreea S. Font, Sam G. Stafford and **Simon Pfeifer**. Connecting the structure of dark matter haloes to the primordial power spectrum. *MNRAS*, *in press*, art. arXiv:2005.12933, Jun 2020

Acknowledgements

First and foremost, I would like to thank my supervisor, Ian McCarthy. I am truly grateful for the mentoring you have provided, both professionally and unprofessionally. Working with you during a summer project, and the following Masters project, cemented my intentions to continue in academia. I remember you told me during our first conversation that your door would always be open, especially to talk about science. This has continued to be true despite increasing time constraints. Your subtle ability to motivate and your patient and easy-going attitude have been a great resource during my academic life.

I would also like to thank Andreea Font. You were happy to take me on as a summer student and without you I would not be here today. And thank you Rob Crain for your honest, down-to-earth advice. Both of you have been very supportive supervisors.

Additionally, I would like to extend a special thanks to Juliana Kwan. Firstly, for being a seemingly infinite source of knowledge and secondly, for the invaluable support you have given me. Thank you also to Jaime Salcido; the HPC group would not be the same without you. Your insight and attitude to life has been a fantastic source of joy.

One of my deepest thanks goes to my fellow PhD students, many of you I am proud to call my friends. Quite simply, I could not have done this without you. I am afraid of mentioning names in fear of missing anyone, but I trust that you know how grateful I am for all of you. My PhD has brought me to tears a few times but I am happy to say that these were due to laughter rather than some disastrous event. This is not to say that I never struggled, in fact I most definitely did. But my struggle was made bearable through the moral support from the tea breaks, pay-day lunches, nerf battles, mid-week

pub trips, games of football, coding problems, trips, jokes and the host of individual interactions that all of you made possible.

I would also like to extend my appreciation for everyone at the ARI. I feel privileged to have had the opportunity to complete my PhD in such a friendly and welcoming institute. I would like to give my thanks to Anna Hodgkinson and Danielle Coogan for being so incredibly helpful with any matter I raised with you. And thank you to Dan Harman and Ben Clark for making things work despite my unintentional attempts at breaking them.

Of course, I have to thank my parents. Thank you for nudging me in the right direction, for encouraging me, for your patience in times of hardship and for giving me the tools and the freedom to succeed on my own terms. Without your support, both material and moral, this would have been impossible.

And last but certainly not least, thank you Alys for believing in me even when I do not. Your love and ability to see the good in all the things around you have given me courage in times when I needed it most.

“The Universe, what a concept.”

- Dr. James Tooper

“I don’t know half of you half as well as I should like; and I like less than half of you half as well as you deserve.”

- J. R. R. Tolkien, *The Fellowship of the Ring*

“Dude, suckin’ at something is the first step to being sorta good at something.”

- Jake the Dog

Contents

Declaration	ii
Abstract	iii
Publications	v
Acknowledgements	vi
Contents	ix
List of Tables	xii
List of Figures	xiii
1 General introduction	1
1.1 The standard model of cosmology	1
1.2 Dark energy	7
1.3 Geometric probes	12
1.4 Large-scale structure	18
2 Computational Cosmology	25
2.1 Cosmological hydrodynamical simulations	25

2.1.1	Gravity solver	26
2.1.2	Gas dynamics	29
2.1.3	Subgrid physics	31
2.1.4	Initial conditions	33
2.1.5	BAHAMAS	35
2.2	Cosmological parameter selection	38
3	The effect of dynamical dark energy on large-scale structure	53
3.1	Introduction	53
3.2	Matter clustering	56
3.2.1	Matter power spectrum	56
3.2.2	2-point autocorrelation function	57
3.3	Halo abundance	60
3.3.1	Halo mass function	60
3.3.2	Halo number counts	64
3.4	Collapse of structure	66
3.4.1	Mass accretion	66
3.5	Halo structure	70
3.5.1	Radial velocity profiles	70
3.5.2	Total mass density profile	73
3.5.3	Slope of the density profiles	76
3.5.4	Concentration–mass relation	78
3.6	Summary	80

4	Impact of baryons and its effect on cosmology	85
4.1	Matter clustering	88
4.1.1	Matter power spectrum	88
4.2	Halo abundance	88
4.2.1	Halo mass function	88
4.3	Halo stucture	92
4.3.1	Density profiles	92
4.4	Summary	92
5	Summary and future work	95
5.1	Summary	95
5.2	Future work	98
A	Appendix	101
	Bibliography	105

List of Tables

2.1	The priors of the parameters used in the MCMC analysis.	41
2.2	The cosmological parameters of the 6 chosen cosmologies.	48

List of Figures

2.1	The w_0 - w_a parameter space constraints from different combinations of data.	43
2.2	The effect of A_{lens} on the $w_0 - w_a$ and $\Omega_m - \sigma_8$ parameter space. . . .	45
2.3	The evolution of the analytical quantities: $w(a)$, Ω_m , $H(a)$ and $D(a)$	50
2.4	The matter power spectrum of the initial conditions at $z = 127$	51
3.1	The total matter power spectrum of the collisionless simulations for the different cosmologies and redshifts.	55
3.2	The 2-point auto-correlation function of dark matter haloes for the different cosmologies and mass bins	58
3.3	The halo mass function of the collisionless simulations for the different cosmologies and redshifts.	61
3.4	The median fractional change in halo mass relative to matched haloes from the Λ CDM cosmology.	62
3.5	The number density of dark matter haloes for different cosmologies and mass cuts.	65
3.6	The mass of haloes from DDE cosmologies as a function of scale factor, normalised by the mass at present day.	67

3.7	The mass accretion rates of haloes from DDE cosmologies as a function of scale factor.	69
3.8	The stacked radial velocity profiles of dark matter haloes from DDE cosmologies.	71
3.9	Median radial total mass density profiles of matched haloes for the different DDE cosmologies for collisionless simulations.	74
3.10	The logarithmic slope of the median density profiles of dark matter haloes from DDE cosmologies.	77
3.11	The concentration-Mass relation of dark matter haloes for the different cosmologies.	79
4.1	The total matter power spectra for the different cosmologies from hydrodynamical simulations and the collisionless simulations with added baryonic effects.	89
4.2	The halo mass function for the hydrodynamical simulations and the collisionless simulations with added baryonic effects.	90
4.3	The fractional change in halo mass of haloes from the hydrodynamical simulations relative to their matched dark matter counterparts.	91
4.4	The median radial total mass density profiles for the different DDE cosmologies from the hydrodynamical simulations and the collisionless simulations with added baryonic effects.	93

Chapter 1

General introduction

The main objective of this work is to explore alternative theories of dark energy and investigate their impact on the growth of structure. In this chapter, I aim to provide an introduction and discussion of the cosmological background that will provide a foundation for the work presented in this thesis. I present a brief primer on the standard model of cosmology (1.1), review the broad topic of dark energy and the current state of the theoretical field (1.2), describe the range of geometric probes that are employed to constrain dark energy (1.3) and finally, explore the potential benefits of using the growth of large-scale structure as a complementary tool to constrain dark energy (1.4).

1.1 The standard model of cosmology

For the last two decades, we have, to a large extent, successfully described the behaviour of our Universe using the standard model of cosmology, the Λ CDM model. This term is, by and large, an umbrella term that encompasses a wide range of physical principles and encapsulates a set of theories that are used to describe the cosmological observations of our Universe. The Λ CDM model is a solution to general relativity for a homogeneous, isotropic Universe that contains ordinary and dark matter, with an accelerated expansion at late times described by dark energy in the form of a cosmological constant, Λ . The origin and immediate evolution is described with the Big

Bang model and an early period of rapid expansion, respectively. I will briefly outline the cosmological timeline and then present a more formal discussion of the Λ CDM model.

At the beginning of the cosmological timeline, the Universe was in a very hot, dense state before going through a brief phase of accelerated expansion termed inflation. This period of inflation caused the Universe to expand and cool, and stretched out the tiny quantum fluctuations present in the very early Universe into large scale density fluctuations which are the seeds for the collapsed structure we see today. Inflation is also used to explain other cosmological properties, such as the spatially flat geometry (the flatness problem) and the Gaussian perturbations which are almost scale invariant, which I will not discuss further here.

As the Universe continued to expand and cool, atomic nuclei were able to combine to form elements heavier than hydrogen (just a proton in the ionized state), in a process called Big Bang nucleosynthesis. The abundance of these elements places a variety of constraints on our cosmological model, including the baryon density and the number of relativistic species. The next drastic change happened when matter and radiation decoupled which allowed the radiation to free-stream across the Universe and be observed today as the Cosmic Microwave Background (CMB). The CMB serves as one of the most constraining observables that any cosmological model needs to be able to describe as it contains a wealth of information of the early Universe, such as the distribution and amplitude of primordial density fluctuations. The matter-radiation decoupling, also known as the era of recombination, allowed matter to recombine into neutral atoms and collapse under the force of gravity, having previously been hindered by the radiation pressure. This collapse of structure, described by general relativity, eventually leads to the formation of the stars and galaxies we see today.

At this stage it is worth introducing the constituents that make up the total energy budget of our Universe; radiation, matter and dark energy. I describe these here briefly but go through a more formal description later. Radiation dominates the energy budget at early times and plays a key role in structure formation until it free-streams after the matter-radiation decoupling. The matter in the Universe is typically split between

baryonic matter and dark matter. Baryonic matter is able to interact through all four of the fundamental forces (gravity, electromagnetic, weak and strong force) and makes up the majority of ‘ordinary’ matter (dust, stars, planets, etc.). On the other hand, dark matter behaves rather differently to baryonic matter and it is one of the more recent additions to the standard model of cosmology. Dark matter is assumed to interact purely gravitationally and takes up the large majority of the matter energy density budget of the Universe. Additionally, its velocity at decoupling is significantly lower than the speed of light and it is thus labeled cold dark matter (CDM). Lastly, we have the dark energy term that dominates the energy budget of our Universe today and is used to explain the current accelerated expansion of the Universe. In Λ CDM, dark energy is described by the cosmological constant, Λ , which is a repulsive force that does not evolve with space or time.

After this general introduction to Λ CDM, I would like to cover certain aspects more formally. It is often mused that the Λ CDM model can describe the Universe with only 6 free parameters, with a lesser advertised caveat that this simplicity is supported by a host of accompanying assumptions and approximations. While I cannot compile an exhaustive list of these, I will aim to cover the fundamentals that come together to form the standard model of cosmology.

One the most important concepts in cosmology is the ‘cosmological principle’ which states we do not occupy a special place in the Universe. If this is correct, it leads to the conclusion that that the Universe is isotropic and homogeneous on very large scales. By considering the cosmological principle, one can describe the the Universe in a 4-dimensional space using the Friedmann-Lemaître-Robertson-Walker space-time metric,

$$ds^2 = -c^2 dt^2 + a^2(t) \left[\frac{dr^2}{1 - kr^2} + r^2(d\theta^2 + \sin^2\theta d\phi^2) \right], \quad (1.1)$$

where the first term on the right-hand side corresponds to the temporal evolution, the second term in square brackets the spatial evolution in spherical coordinates and $a(t)$ is the scale factor, normalised to $a(t_0) = 1$ today. From Equation 1.1 it is possible to

construct the Friedmann equations by applying the field equations of general relativity (Friedmann, 1922),

$$H^2 = \frac{\dot{a}^2}{a^2} = \frac{8\pi G}{3}\rho - \frac{kc^2}{a^2} + \frac{\Lambda c^2}{3}, \quad (1.2)$$

$$\frac{\ddot{a}}{a} = -\frac{4\pi G}{3}\left(\rho + \frac{3p}{c^2}\right) + \frac{\Lambda c^2}{3}, \quad (1.3)$$

where ρ is density, p is pressure, G is the gravitational constant and H is the Hubble parameter. c is the speed of light which we include here but set to unity for the remainder of this Section. k is the curvature of space, defined such that $k = 0$ is spatially flat. Λ is the cosmological constant, also called the vacuum energy density, which we have already mentioned above. The overdot denotes the derivative with respect to time. The Friedmann equations are two of the most fundamental equations in cosmology as they describe the expansion rate and the acceleration of the expansion rate of the Universe, respectively, in the context of general relativity.

We can rewrite Equation 1.2 in the form

$$\frac{8\pi G}{3H^2}\rho - \frac{k}{a^2H^2} + \frac{\Lambda}{3H^2} = 1, \quad (1.4)$$

which we can use to define the dimensionless density parameters; $\Omega_m = \frac{8\pi G}{3H^2}\rho$, $\Omega_k = -\frac{k}{a^2H^2}$ and $\Omega_\Lambda = \frac{\Lambda}{3H^2}$. Using this we can write

$$\Omega_m + \Omega_\Lambda = 1 - \Omega_k, \quad (1.5)$$

which tells us that if the matter density and vacuum energy density sum to unity, then $\Omega_k = 0$ and the Universe must be flat. Similarly, we can define the critical density, $\rho_{crit} = \frac{3H^2}{8\pi G}$, as the density required for a flat geometry, with $\Omega_m = \frac{\rho}{\rho_{crit}}$. From these equations it is clear why much of modern cosmology is focused on measuring these quantities. Evidence from CMB experiments (de Bernardis et al., 2000; Jaffe et al.,

2001; Rubiño-Martin et al., 2003; Fowler et al., 2010; Hinshaw et al., 2013; Planck Collaboration et al., 2018), galaxy clustering (Chae, 1999; Alam et al., 2016) and supernovae (Scolnic et al., 2018) are consistent with a flat geometry and thus $\Omega_k = 0$ is assumed in Λ CDM. This assumption allows us to write $\Omega_\Lambda = 1 - \Omega_m = 1 - \Omega_b - \Omega_c$, where I have now split the matter energy density into its baryonic, Ω_b , and CDM, Ω_c , components. An additional contribution to the energy budget of the Universe comes from massive neutrinos, although they contribute very little and are typically not included in the standard cosmological model. They are important at early times, before recombination, when the majority of the neutrinos are still relativistic. For a reasonable sum of neutrino mass, $M_\nu = 0.1$ eV, 90% of massive neutrinos are non-relativistic by $z \lesssim 100$ (Ali-Haïmoud and Bird, 2013). To calculate the neutrino contribution to the energy budget, one can use the approximation $\Omega_\nu = M_\nu/(93.14h^2)$ which assumes that all neutrinos are non-relativistic and have the same mass (Lesgourgues and Pastor, 2006).

We are able to model these components by assuming that they are well described by a perfect fluid with an equation of state, $w = \frac{p}{\rho}$, with a density evolution of,

$$\dot{\rho} = -3H(\rho + p) = -3H(1 + w)\rho. \quad (1.6)$$

Using the Friedmann equations and the fluid equation with the equation of state, equations 1.2, 1.3 and 1.6 respectively, it is then possible to calculate the expansion of a spatially flat universe filled with a set non-interacting (except through gravity) fluids normalised at the present day,

$$\frac{H^2}{H_0^2} = \sum_{i=0} \Omega_{i,0} a^{-3(1+w_i)}, \quad (1.7)$$

where the sum is over each different constituent and w_i is the equation of state parameter of that constituent. For a flat Λ CDM model we have matter ($w = -\frac{1}{3}$), radiation ($w = 0$) and a cosmological constant ($w = -1$) which gives us a well known form for the expansion history,

$$H = H_0 \sqrt{\Omega_{m,0} a^{-3} + \Omega_{r,0} a^{-4} + \Omega_{\Lambda,0}}, \quad (1.8)$$

where H_0 is the Hubble constant measured at the present day. I have included the zero subscript for the density parameters here to emphasise that these are present day quantities and to be consistent with Equation 1.7. But I will omit them from now on as is usually the case, so that Ω refers to the present day quantity and $\Omega(a)$ to the quantity at that particular scale factor. I have also included radiation in Equation 1.8 for completeness. However, Ω_r does not contribute significantly to the evolution of the Universe at late times due to the rapid drop in its energy density as it scales with a^{-4} . It is also not included as one of the 6 free parameters that describe Λ CDM since its value can be calculated with great precision from the CMB temperature (Fixsen, 2009). So far, I have covered 3 parameters of the Λ CDM model: H_0 , Ω_b and Ω_m . Formally, Ω_{Λ} and Ω_c are not included as they can be trivially calculated from Equation 1.5 once the other parameters are known, and under our assumption of a flat Universe.

As mentioned above, it is thought that inflation generates the large scale density fluctuations which are visible in the CMB and set the seeds for the resulting collapse of structure. Therefore it is important to be able to characterise these fluctuations. Originally, before theories of inflation, a power spectrum of the density fluctuation was generally devised in an *ad hoc* fashion to contain properties that seemed necessary to retrieve the required formation of structure. This is typically called the Harrison-Zel'dovich spectrum which assumes that fluctuations are scale invariant (Harrison, 1970; Zeldovich, 1972; Peebles and Yu, 1970). With the onset of inflation models came further support for this particular form, although most inflation models predicted that the fluctuations are not quite scale invariant, resulting in the form of the primordial power spectrum,

$$P(k) = A_s k^{n_s-1}. \quad (1.9)$$

Equation 1.9 gives us two more parameters of the Λ CDM model; the amplitude of the primordial power spectrum, A_s , and the scalar spectral index, n_s . The Harrison-

Zel'dovich spectrum assumes that $n_s = 1$ while popular models of inflation, such as slow-roll inflation, predict $n_s \lesssim 1$. The latest constraints from CMB experiments place $n_s = 0.9652 \pm 0.0042$ (Planck Collaboration et al., 2018).

The last free parameter of the Λ CDM model is the optical depth of reionisation, τ . After recombination, the hydrogen gas goes through its last major phase change by being reionised by the very first stars that form in the Universe.

$$\tau = \sigma_T \int_0^{z_{rec}} n_e(z') dz \quad (1.10)$$

Equation 1.10 relates the optical depth to the electron column density, $n_e(z)$, where σ_T is the Thomson cross-section. Since reionisation occurs at a high redshift, the Universe is still relatively dense and photons from the CMB undergo Thomson scattering from the sea of free electrons that are now present. This removes anisotropies on small scales and introduces polarisation in the CMB signal. It also significantly affects the observed amplitude of the CMB signal which would have a subsequent effect on cosmological parameter estimation if not properly accounted for. As the Universe continues to expand, the electron density drops and so does the rate of Thomson scattering.

1.2 Dark energy

The accelerated expansion of the Universe in Λ CDM is described by the cosmological constant, Λ , which was introduced as a concept at the beginning of the 19th century. Λ was originally introduced by Albert Einstein in his field equations for general relativity in order to fix, what he thought of as, an undesirable property of his equations (Einstein, 1917). At that time it was thought that the Universe was static, however Einstein's field equations predicted a Universe that was collapsing due to gravity. Therefore he added Λ , a force that counteracted the force of gravity and resulted in a static Universe. Not long after, Edwin Hubble discovered that the Universe was in fact not static but expanding. Alexander Friedmann, and later Georges Lemaître, had already found

an expanding Universe was a valid solution to the Einstein's original field equations (Friedmann, 1922; Lemaître, 1927), making Λ unnecessary. The failure to predict cosmic expansion based on his field equations was referred to by Einstein as his biggest blunder. The need for Λ came back in 1998 when two independent teams discovered that the Universe was not only expanding but that this expansion was accelerating (Riess et al., 1998; Perlmutter et al., 1999). This acceleration required a force opposite to gravity and, hence, Λ was reintroduced.

The cosmological constant produces very accurate theoretical predictions as part of the Λ CDM model and its simplicity is an attractive feature. Although, attempts to link Λ to particle physics through quantum field theory have resulted in predictions of the scale of vacuum energy densities that are enormously larger than those observed for Λ (which has earned it the term of "the worst theoretical prediction in the history of physics") and is usually referred to as the cosmological constant problem (Adler et al., 1995; Hobson et al., 2007). It is in general difficult to reason why we live in a Universe with such a specific, tiny vacuum energy unless the anthropic principle is used, which argues that the conditions required to form the observable Universe are necessary for us to exist and make observations of them in the first place. Such arguments are rather unphysical and most likely not testable. This lack of physical interpretation of the cosmological constant has justified the search for alternative models for the accelerated expansion of the Universe.

Dark energy (DE) is commonly used as an umbrella term for any model that aims to describe the accelerated expansion of the Universe, of which Λ is the simplest. DE models can generally be split into two broad classes. The first of these deals with new kinds of energy in the form of scalar fields that can change with time and/or space. These can be of a form similar to the early period of inflation but with significantly different magnitude and time scales. The second class assumes that general relativity is, to some extent, incorrect or incomplete. These models are referred to as modified gravity (MG) and are sometimes viewed as separate from DE since they do not add an extra energy component, although I loosely group them together here. Popular models of MG employ a type of 'screening' mechanism in which gravity is forced to

agree with general relativity at small separations, high accelerations or in areas of high density (Khoury and Weltman, 2004; Hinterbichler and Khoury, 2010). This ensures that local experiments of gravity, such as those on solar system scales which support general relativity to very high precision, are not violated but the Universe is allowed to undergo accelerated expansion on large scales. The work presented here focuses on the first class and therefore the discussion of MG models remains brief.

Scalar fields introduce a new degree of freedom, replacing the vacuum energy that is constant in time and space, with a dynamical energy component. Due to this nature they are often referred to as dynamical dark energy (DDE), which I adopt throughout the thesis. A typical scalar field, ϕ , with Lagrangian, $\mathcal{L} = \frac{1}{2}\partial^\mu\phi\partial_\mu\phi - V(\phi)$, has a stress-energy that is expressed as a perfect fluid with (Wetterich, 1988; Peebles and Ratra, 1988; Ratra and Peebles, 1988)

$$\rho = \frac{\dot{\phi}^2}{2} + V(\phi), \quad p = \frac{\dot{\phi}^2}{2} - V(\phi). \quad (1.11)$$

This scalar field is usually assumed to be spatially homogeneous but a function of time and the overdot represents the derivative with time. $\frac{\dot{\phi}^2}{2}$ is the kinetic energy and $V(\phi)$ is the potential energy. Using equation of state, the scalar field has an equation of state of

$$w = \frac{p}{\rho} = \frac{\frac{\dot{\phi}^2}{2} - V(\phi)}{\frac{\dot{\phi}^2}{2} + V(\phi)}. \quad (1.12)$$

These types of scalar field models are referred to as quintessence (Frieman et al., 1995; Ratra and Peebles, 1988; Wetterich, 1988; Caldwell et al., 1998; Zlatev et al., 1999) and have some interesting properties. We can identify two regimes; if the potential energy dominates, $\frac{\dot{\phi}^2}{2} \ll V(\phi)$, we arrive at a cosmological constant-like dark energy with $w \approx -1$ that evolves very slowly and is similar to the slow-roll mechanism of inflation. Alternatively, if the kinetic energy of the scalar field dominates, $\frac{\dot{\phi}^2}{2} \gg V(\phi)$, the scalar field evolves very quickly and has $w \approx 1$.

The equation of motion for such a scalar field is described by the Klein-Gordon equation,

$$\ddot{\phi} + 3H\dot{\phi} + \frac{\partial V}{\partial \phi} = 0. \quad (1.13)$$

By looking at their dynamic evolution, these types of scalar fields can be separated into two classes (Caldwell and Linder, 2005). Models referred to as ‘freezing’ evolve rapidly before slowing over time, acting like vacuum energy at late times. Freezing models typically start at $w > -1$ and asymptotically evolve towards $w \approx -1$. This is true for potentials that evolve as an inverse power law or exponentially decrease with ϕ . This causes the slope of the potential to decrease faster than the Hubble friction term, $3H\dot{\phi}$, and therefore the Hubble friction dominates at late times in Equation 1.13. Alternatively, models referred to as ‘thawing’ are dominated by the Hubble friction at early times and evolve faster with time, acting less like a vacuum energy with time. A simple potential for which this is true is a potential, $V(\phi) = \frac{1}{2}m_\phi^2\phi^2$, with a field mass, m_ϕ . Thawing models typically start at, and then evolve away from, $w \approx -1$.

A particular subset of freezing models have been identified and labeled ‘tracker’ fields because of their particular characteristics (Wetterich, 1995; Ferreira and Joyce, 1997; Copeland et al., 1998; Zlatev et al., 1999). These fields track the energy density of the dominant component in the Universe, i.e. radiation at early times and then matter, before dominating the energy density at late times. Their late-time behaviour are insensitive to initial conditions and partially address the coincidence problem, which states that we exist in a special period in the evolution of the Universe when DE is transitioning to becoming dominant. By tracking the energy density of other components, the energy density is always decreasing and it becomes less coincidental that DE dominates at the present day.

Although these models aim to improve on the cosmological constant by associating them with physical scalar fields, they also introduce new considerations and model specific problems. They do not address the fine-tuning problem of having a specific, tiny vacuum energy density (Weinberg, 1989) but assume that the potential will even-

tually reach some small value in the future. In addition, to allow a slow roll behaviour, models require a very small field mass compared to mass scales in particle physics. This in turn requires the scalar field to be very smooth and so any scalar fields that allow non-homogeneity must do so on very large scales (Carroll, 1998).

Another avenue other than quintessence is that of k-essence models (Chiba et al., 2000; Armendariz-Picon et al., 2001). These modify the kinetic energy term in the Lagrangian and are mostly phenomenological. Their aim is to provide a dynamical model that does not depend on the fine-tuning of initial conditions or of the field mass, m_ϕ , to address the coincidence problem. The so-called ‘attractor’ solutions in k-essence are similar to the tracker models above in that they track the equation of state of the dominant energy component at early times. However, k-essence attractor models do not require tuning of the scale of their potential unlike the tracker models. Instead, they suffer from changes to the sound speed of perturbations that can be unphysical (Bonvin et al., 2006; Babichev et al., 2008).

It is clear from the brief descriptions of different DE models that there is no real consensus on the physical explanation of cosmic acceleration, nor a sufficiently general description of its behaviour. The common parameter that connects most DE models is the equation of state parameter, w . Since most of the models enable DE to evolve with time, it would be useful to be able to describe the temporal evolution of w . This has been attempted by simply Taylor expanding w with redshift, resulting in $w(z) = w + w'z$ (Cooray and Huterer, 1999). This form, and other similar prescriptions (Gerke and Efstathiou, 2002), work very well at low redshift and have just one additional parameter, which is generally preferred over more complex expressions. However, their behaviours at large redshifts tend to become unphysical. Additionally, one would like to be able to describe a large range of different DDE models. A common parameterisation of DDE was introduced by Chevallier and Polarski (2001) and Linder (2003),

$$w(a) = w_0 + w_a(1 - a), \quad (1.14)$$

where a is the expansion factor and w_0 and w_a are free parameters. One can recover

Λ by setting $w_0 = -1$ and $w_a = 0$. The benefits of this parameterisation are that one can generate the expansion histories very easily (as I will show below) and that it can mimic the expansion history of many DDE models.

Assuming a spatially flat Universe, the expansion history is described by the Friedman equation given in Equation 1.7, where the sum is of the energy densities of the constituents of the Universe, i.e. matter, radiation and DE. The temporal evolution of the energy density is described by a perfect fluid given by Equation 1.6. The solutions to Equation 1.6 are simple for matter and radiation with $w = 0$ and $w = \frac{1}{3}$, respectively. The solution is more complicated for the dark energy equation of state that evolves with time since the typical approximation of $\rho = \rho_0 a^{-3(1+w)}$ is only valid for constant w . One has to substitute Equation 1.14 into Equation 1.6 and solve the differential by integration. This results in some additional terms in the density evolution which have explicit dependencies on a ,

$$\rho_{\text{DE}}(a) = \rho_{\text{DE},0} a^{-3(1+w_a+w_0)} e^{-3w_a(1-a)}, \quad (1.15)$$

where $\rho_{\text{DE},0}$ is the dark energy density at the present day (Linder, 2003). Substituting Equation 1.15, using the relation for the dimensionless density parameter, $\Omega = \frac{8\pi G}{3H_0^2} \rho_0$, into Equation 1.2 results in an expression for the expansion history as a function of present day energy densities,

$$H(a)^2 = H_0^2 \left(\Omega_{\text{r}} a^{-4} + \Omega_{\text{m}} a^{-3} + \Omega_{\text{DE}} a^{-3(1+w_a+w_0)} e^{-3w_a(1-a)} \right). \quad (1.16)$$

This form for DDE is used throughout this work.

1.3 Geometric probes

With some of the general DDE models covered and their effect on the background cosmology described, I will show how these fold into observational cosmology, specifically geometric probes. Observations fundamentally rely on measuring the fluxes of

object and angles on the sky. These observations can then be converted into two separate distances, the luminosity distance and the angular diameter distance, respectively. Their concepts are well known; the luminosity distance, d_L , is the distance an object with a given luminosity, L , would have to be to produce a flux, $F = \frac{L}{4\pi d_L^2}$. The angular diameter distance, d_A , is the distance that a given physical separation, x , which is perpendicular to the line of sight, would have to be to subtend an angle on the sky, $\theta = \frac{x}{d_A}$ (given the small angle approximation). These geometric relations are related to the comoving distance, $r(z)$, through

$$d_L = (1+z)r(z), \quad d_A = \frac{1}{(1+z)}r(z). \quad (1.17)$$

DE folds into these equations through the comoving distance which can be calculated with

$$r(z) = \lim_{\Omega'_k \rightarrow \Omega_k} \frac{1}{H_0 \sqrt{\Omega'_k}} \sinh(\sqrt{\Omega'_k} \int_0^z \frac{H_0}{H(z')} dz'). \quad (1.18)$$

By affecting the expansion history, DE also affects the fundamental observable quantities. If one were to obtain accurate measurements of d_L or d_A along with accurate measurements of redshift, it would be possible to gain constraints on $H(z)$ and therefore $w(z)$.

Such direct reconstruction studies have been attempted through a variety of methods (Sahni and Starobinsky, 2006). Due to the plethora of DE models, it becomes challenging to test each and every model against observations. Therefore, these approaches aim to reconstruct DE from observations in a model independent fashion. This would determine DE properties that are not part of any single DE model but an underlying characteristic of DE that any given DE model would have to fulfill. The difficulty of these methods is that observation place constrains on $H(z)$ at only a few points in redshift.

Strong constraints on the expansion rate at the present day can be achieved by using Type Ia supernovae (SNe Ia) as standard candles, which is how the Universe was first confirmed to be undergoing accelerated expansion (Riess et al., 1998; Perlmutter et al.,

1999). The prospect of using SN Ia as standard candles had been discussed long before their actual application (Kowal, 1968; Colgate, 1979). Standard candles refer to objects with approximately fixed intrinsic luminosity which enables them to be used to infer distances simply through the inverse square law, i.e. the flux-luminosity relation given above. SNe Ia are not perfect standard candles and there are variations in their light-curves that introduce systematic errors. Empirical relations are used to correct for these variations and reduce the systematic error (Phillips, 1993; Riess et al., 1996; Tripp, 1998; Conley et al., 2011; Rubin et al., 2015). One benefit of using supernovae as standard candles is that they are very bright. They are bright enough to outshine their host galaxy and can therefore be detected over large distances.

Instead of the flux-luminosity relation, SNe Ia observations typically work with the well known distance modulus which is given by

$$m - M = 5 \log_{10} \left(\frac{d_L}{10 \text{pc}} \right), \quad (1.19)$$

where m and M are the apparent and absolute magnitude, respectively. It is clear that by measuring m and inferring M from the SNe Ia light-curve, correcting for systematic errors, we can gain a measure of the physical distance to the supernova and therefore constrain cosmological parameters (March et al., 2011). The current constraints from SNe Ia and other standard candles has placed constraints of $H_0 = 74.03 \pm 1.42 \text{ km s}^{-1} \text{ Mpc}^{-1}$ (Riess et al., 2019). This constraint comes from observations of objects that are at low redshift and are thus labeled ‘local’ measurements. That also means that they can only give good constraints on the expansion rate at the present day rather than as a function of redshift.

Baryon acoustic oscillations (BAO) form another geometric probe that is useful for constraining DE. Predicted over half a century ago (Sunyaev and Zeldovich, 1970; Peebles and Yu, 1970), they have been detected and measured in a range of surveys (Eisenstein et al., 2005; Cole et al., 2005; Padmanabhan et al., 2007; Percival et al., 2007; Beutler et al., 2011; Ross et al., 2015; Delubac et al., 2015; Alam et al., 2017; de Sainte Agathe et al., 2019). The physics of BAO are very well understood from a

theoretical perspective which makes them easier to model and allows for systematic errors to be accounted for. The BAO signal originates from the interactions of baryons and photons before the era of recombination. As I have mentioned in Section 1.1, high density regions in the primordial Universe form the seeds for structure collapse. Baryons want to collapse onto high density regions due to gravity but photons want to free-stream out of high density regions, smoothing out any density peaks. However, since the radiation and baryons are coupled and the radiation energy density in the early Universe dominates, a shock is induced that forms spherical shells of baryon-photon fluid which move outward from the centre of high density regions. Once the Universe cools and recombination occurs, the radiation pressure is removed as photons free-stream and the shells of baryons are left behind, ‘frozen’ in space. DM does not undergo the same process as it is not coupled to the photons, although it is weakly coupled to the baryons through gravity, which allows the DM to collapse onto the high density regions. After recombination, we are then left with high densities of DM at the centre of over-dense regions which are surrounded by shells of high density baryons. Since structure forms from such high density regions, we expect to find an increases number of galaxies that are separated by the characteristic size of the shells, referred to as the sound horizon. This sound horizon scale is called a standard ruler, just like SNe Ia are called standard candles, because it is of a well known size.

The size of the sound horizon at recombination depends on Ω_b , Ω_r and the age of the Universe at recombination. These can be measured very precisely from the CMB and result in a size of the sound horizon at recombination $r_s = 147.18 \pm 0.29$ Mpc (Planck Collaboration et al., 2018). The BAO signal, the increased density on scales of the sound horizon, shows up in the excess of the clustering of galaxies separated by the sound horizon distance. By measuring the clustering of galaxies over a large volume, one can measure the angular separation on the sky, $\Delta\theta_s$, on which this clustering appears and link it to the angular diameter distance through,

$$\Delta\theta_s = \frac{r_s}{d_A}. \quad (1.20)$$

The BAO signal is spherically symmetric and so can also be measured along the line

of sight through the redshift range the BAO signal extends,

$$\Delta z_s = \frac{H(z)r_s}{c}. \quad (1.21)$$

This is more difficult to measure than the angular signal since it is measured along a 1D line element rather than a 2D surface. BAO require large samples of galaxies to be measured with statistical significance, so in order to reduce the statistical error in the BAO measurements the transverse and line of sight measurements can be grouped together through (Eisenstein et al., 2005)

$$D_V(z) = \left[(1+z)^2 d_A^2 \frac{cz}{H(z)} \right]^{1/3}. \quad (1.22)$$

D_V is referred to as the dilation scale and is essentially a geometric mean of two line of sight and one radial directions. By combining these with high accuracy (spectroscopic) redshift measurements, BAO can sample the expansion history over a large range of redshift and place powerful constraints on DE.

The last observational probe I will discuss in this section is the CMB. The CMB presents an incredible amount of information about our Universe inscribed in the shape of its angular power spectra (temperature, polarization and their cross-correlation). Through the interaction of baryons and photons in the early Universe, the (temperature) power spectrum is made up of oscillations from which many physical properties can be extracted. However, the redshift of the CMB is very large, $z_* \approx 1100$, and the energy density of DE is thought to be comparatively low compared to matter and radiation at that time. Therefore DE has very little part in imprinting its characteristics in the CMB power spectrum at recombination. But DE has had a significant role in the evolution of the Universe, especially at late times, that has affected the CMB signal for us, the observers, at the present day. It is a signal that has experienced the entire evolution of the Universe since recombination, and this property is why the CMB can be a useful geometric probe for constraining DE.

The main DE constraint comes from measuring the angle subtended by the sound hori-

zon, the one responsible for the BAO signal, at the surface of last scattering,

$$\theta_* = \frac{r_s(z_*)}{r(z_*)}. \quad (1.23)$$

This probes the entire expansion history from $z = 0$ to the redshift of recombination, z_* , through the comoving distance to the surface of last scattering, $r(z_*)$. Note that the distance to the surface of last scattering on its own effectively only probes the integrated expansion history. This means that different DE models, e.g. models that behave wildly different at low redshift, cannot be distinguished if their integrated expansion history are the same. In other words, the functional form of $H(z)$ would be allowed to be very different shapes as long as they have the same integral. Changes in the distance to the surface of last scattering, through changes to the integrated expansion history, would shift the peaks of the oscillations in the CMB angular power spectrum by changing their angular size on the sky. The angular location of these peaks can be measured with high precision. In fact, the specific location and relative amplitudes of the peaks also places constraints on Ω_b and Ω_c which determine $H(z)$ (see Equation 1.8).

A second effect of the CMB is the integrated Sachs Wolf effect (Sachs and Wolfe, 1967). This occurs due to the evolving gravitational potential that CMB photons travel through on their way to the observer. Simply put, photons are compressed (blue-shifted) as they enter a gravitational potential and stretched (red-shifted) as they leave. If the potential were to evolve, the photons would experience an unequal amount of compression and stretching. In an expanding Universe and when DE dominates, potential wells grow weaker (with respect to a matter dominated Universe) as the photons travel through and therefore they undergo net compression. This induces additional power in the CMB power spectrum on large scales and can be detected through cross-correlation with the positions of clusters, since these correspond to the largest gravitational potentials (Fosalba et al., 2003; Giannantonio et al., 2008).

1.4 Large-scale structure

Large-scale structure (LSS) forms an important part of cosmology. It is a framework that describes and measures the growth of structure in the Universe. Importantly for the work presented here, it allows the structure to be used as a tool to test cosmology. In the context of constraining DE, the straightforward approach is to try to constrain the expansion history, $H(a)$, directly as DE only affects this quantity (see Equation 1.8). This is usually done through geometric probes, discussed above, which measure the expansion rate at a particular redshift. However, LSS offers an independent and complementary approach to constrain cosmology. As I will show below, the effects on the expansion history filter through and affect the growth of structure, opening an avenue to constrain $H(a)$ through LSS. Additionally, LSS can make it possible to distinguish different models of DE which would not be possible using geometric probes. For example, scalar field DE and MG models can be made to produce the same expansion history. However, their effect on LSS should be different since, in addition to the effects on $H(a)$, MG models change gravity by design and should therefore change the way structure collapses.

The basic premise of LSS statistics is to characterise the density and distribution of matter on scales larger than galaxies. As mentioned in Section 1.1, the CMB is the earliest observable snapshot of our Universe and we typically characterise its features, primarily its temperature fluctuations which correspond to fluctuations in density, using the matter power spectrum, $P(k)$. The matter power spectrum fully characterises a Gaussian random field of density fluctuations such as the one predicted by inflation.

$$\delta(\bar{k}) = \int d^3\bar{x} e^{-i\bar{k}\cdot\bar{x}} \delta(\bar{x}) \quad (1.24)$$

$$\langle \delta(\bar{k}) \delta(\bar{k}') \rangle = (2\pi)^3 P(k) \hat{\delta}(\bar{k} - \bar{k}') \quad (1.25)$$

In the equations above, $\delta(\bar{k})$ is the Fourier transform of the overdensity, $\delta(\bar{x}) =$

$\frac{\rho(\bar{x}) - \rho_{mean}}{\rho_{mean}}$ with ρ_{mean} being the mean density, $\hat{\delta}$ is the Dirac-delta function and the overline marks vector quantities. The power spectrum is the Fourier transform of the 2-point correlation function, which is explained further in Section 3.2, given by

$$\xi(x) = \langle \delta(\bar{x}_2) \delta(\bar{x}_1) \rangle = \int \frac{d^3k}{(2\pi)^3} e^{i\bar{k} \cdot (\bar{x}_2 - \bar{x}_1)} P(k). \quad (1.26)$$

In the linear regime, k modes evolve independently along with the background evolution of the Universe. $P(k)$ can therefore be linearly evolved by

$$P(k, a) = D(a)^2 P(k), \quad (1.27)$$

where $D(a)$ is the linear growth factor as a function of the scale factor, normalised to be unity at the present day, and $P(k)$ is the matter power spectrum at the present day. The linear growth factor is usually written as a differential equation

$$\ddot{D} + 2H(a)\dot{D} - \frac{3}{2}\Omega_m H_0^2 a^{-3} D = 0, \quad (1.28)$$

which has a popular approximation for a flat Λ CDM cosmology given in Peebles (1980) as

$$D(a) = \frac{5\Omega_m a^2 H(a)^3}{2} \int_0^a \frac{da}{a^3 H(a)^3}. \quad (1.29)$$

It can be seen in Equation 1.28 that the linear growth factor is directly affected by $H(a)$. It is through this relation that it is most clear that LSS can be used to constrain DE.

The matter power spectrum immediately at recombination is linear on effectively all scales. As structure starts to collapse on small scales due to the force of gravity, the power spectrum becomes non-linear on those scales. The scale on which $P(k)$ is non-linear increases with time due to hierarchical structure collapse. The linear matter power spectrum can be evolved with time using Equation 1.27 but predictions for

the non-linear matter power spectrum require N-body simulations, although perturbation theory can also be used to generate predictions into the mildly non-linear regime (Takahashi et al., 2012).

Another useful quantity to define using the power spectrum is the variance of the density field smoothed with a spherical top-hat window function,

$$\sigma^2(R, a) = \frac{1}{2\pi^2} \int_0^\infty k^2 P(k, a) |\widetilde{W}(kR)| dk, \quad (1.30)$$

where $\widetilde{W}(kR)$ is the Fourier transform of the spherical top-hat window function and R is the radius of the window function in real space. This can be used to define the common cosmological parameter σ_8 which is the density fluctuations on 8 Mpc h^{-1} scales, linearly evolved to the present day, and can be used to normalise the amplitude of the matter power spectrum.

One way to observationally measure the matter power spectrum is through weak lensing, a relatively new method that has seen much attention over recent years. The main concept of gravitational lensing is that any gravitational potential bends light causing a lensing effect along the line of sight. Weak gravitational lensing attempts to measure the lensing due to the LSS of the Universe, leading to minor distortions of observations of galaxies. This distortion can be expressed as a mapping of displacement vectors, δx , between the source plane, S , and the image plane, I , through a distortion matrix, A , such that

$$\delta x_S = A \delta x_I, \quad A = \begin{pmatrix} 1 - \kappa - \gamma_1 & -\gamma_2 \\ -\gamma_2 & 1 - \kappa + \gamma_1 \end{pmatrix}. \quad (1.31)$$

The distortion is described by the convergence, κ , and the shear, represented by the complex numbers (γ_1, γ_2) , with the total shear, $|\gamma| = \sqrt{\gamma_1^2 + \gamma_2^2}$.

To calculate the lensing of source galaxies by foreground structure, the shapes of the source galaxies are measured and averaged over nearby galaxies. The signal is very weak and therefore a large number of galaxies need to be observed. The lensing of objects between the source plane and the observer is not equal. It is described by a

weight function, $W(z)$, that describes the efficiency of the lensing as a function of redshift, where the efficiency is greatest approximately half way between source and observer. By calculating the lensing field it is possible to calculate the convergence angular power spectrum, P_l^κ which is related to the underlying matter power spectrum of the LSS between the source and observer through (Kaiser, 1992; Hu and Jain, 2004)

$$P_l^\kappa(z_S) = \int_0^{z_S} \frac{dz}{H(z)d_A^2(z)} W(z)^2 P(k, z). \quad (1.32)$$

Weak lensing contains geometric information from the angular distance and expansion history, and growth of structure information through the matter power spectrum which can be used to place constraints on DE. Theoretical predictions of the weak lensing signal mainly come from N-body simulation which is challenging for a number of reasons. Mainly, it is very computationally expensive to run simulations for every cosmology that one would like to make predictions for. In addition, baryonic effects must be considered since they strongly affect the power spectrum but are also expensive to include in simulations.

Weak lensing also suffers from some observational challenges. The statistical uncertainty can be expressed through (Kaiser, 1992)

$$\Delta P_l^\kappa = \sqrt{\frac{2}{(2l+1)f_{sky}} \left(P_l^\kappa + \frac{\sigma^2(\gamma_i)}{n_{eff}} \right)}, \quad (1.33)$$

where f_{sky} is the fraction of sky coverage, $\sigma(\gamma_i)$ is the standard deviation on the shear and n_{eff} is the effective number of galaxies per steradian with well measured shapes. It is clear that increasing the sky coverage will help to alleviate the impact of all the bracketed terms. This is the simplest way to lower the statistical error, by simply observing more galaxies. $\sigma(\gamma_i)$ and n_{eff} can be grouped together as a shape noise error which is the ability to measure the shape of galaxies accurately, which accounts for the main limitation in weak lensing surveys.

More traditionally, galaxy clusters are used as a powerful probe of structure growth. As the largest collapsed/collapsing objects in the Universe, their formation, distribution

and abundance can give vital insights into cosmology. Galaxy cluster distributions can also be used to place constraints on DE through the 2-point correlation function, and therefore the matter power spectrum (Equation 1.26). This also has a geometric component since distances between clusters have to be measured.

There are a few complications when trying to measure the power spectrum from a distribution of clusters. The first is that collapsed structures do not accurately trace the underlying matter distribution. They are biased tracers, where more massive structures are more strongly clustered because they form near high density peaks in the initial density field (Kaiser, 1984; Bardeen et al., 1986). While it is possible to use more accurate tracers of matter in N-body simulations by using the particles, this is not an option for observations. However, the bias can be accounted for by using the analytic forms of Cole and Kaiser (1989); Mo and White (1996) or functional fits to N-body cosmological simulations (e.g. Tinker et al. (2010)).

An additional complication arises due to the effect of redshift-space distortions (RSD) which applies specifically to observations. This effect occurs because measuring the redshift of a galaxy combines the effect of recession velocity due to the Hubble flow and peculiar velocity, resulting in systematic errors in the calculated distance. This causes objects to be stretched along the line of sight due to small scale velocity dispersion and large scale inflows. However, more recently RSD has been used to constrain cosmology. The theory on linear scales is well developed (Kaiser, 1987; Hamilton, 1998) but on non-linear scales it becomes more difficult. Popular methods involve fitting functions which are fit to cosmological simulation in the non-linear regime and splicing these to the well-known solutions in the linear regime (Hatton and Cole, 1999; Tinker, 2007).

Another crucial quantity for LSS is the abundance of collapsed objects, also referred to as the halo mass function (HMF) for DM haloes (see also Section 3.3.1). Fundamentally, it counts the number of collapsed objects as a function of mass within a given volume. Theoretical predictions for the HMF can be measured directly from cosmological simulations, and emulated (McClintock et al., 2019; Bocquet et al., 2020), or through analytic functions (Press and Schechter, 1974; Bond et al., 1991; Zentner, 2007) and

analytically inspired fitting function calibrated with N-body simulations (Jenkins et al., 2001; Warren et al., 2006; Tinker et al., 2008; Bhattacharya et al., 2011).

Observationally, the abundance of galaxy clusters can be measured using

$$\frac{d^2 N}{d\Omega dz} = \frac{r^2(z)}{H(z)} \frac{dn(M, z)}{dM} dM, \quad (1.34)$$

where N is the absolute number of clusters, $d\Omega$ is the solid angle, $\frac{r^2(z)}{H(z)}$ the comoving volume and $\frac{dn(M, z)}{dM}$ is the HMF. The abundance of clusters can be used to constrain DE through two components of Equation 1.34: the first is geometric since we need to know the comoving volume which depends on the expansion history. The second is through the growth of structure as this determines the number density of clusters.

Observations of galaxy clusters come with a range of systematic errors. The main source for the abundance of clusters is the determination of cluster mass. Traditionally, X-ray observations of clusters were used, under the assumption of hydrostatic equilibrium, to convert gas density and temperature profiles into an integrated mass profile. This underlying assumption has been continually scrutinised and the accuracy of such a method can only get tens of percent accuracy per cluster (McCarthy et al., 2003a,b; Poole et al., 2007; Hoekstra et al., 2012; Mahdavi et al., 2013; Sakr et al., 2018). Another source of systematic error comes from the determination of cluster redshift. By averaging over the redshift of cluster member galaxies, this error can be greatly reduced.

I have introduced the Λ CDM model and described a variety of extensions that replace the cosmological constant with another form of DE. This was followed by a discussion on how DE is typically constrained using geometric probes and, lastly, how LSS can be used as a complementary tool to constrain DE from the growth of structure. In Chapter 2 I motivate the use of hydrodynamic cosmological simulations as tools for accurate theoretical predictions of LSS and review a variety of simulation methods. I follow this with a review of the specific suite of simulations used in this work, BAHAMAS, and discuss my approach to selecting the DE cosmologies on which this

work is based.

Chapter 2

Computational Cosmology

2.1 Cosmological hydrodynamical simulations

The main aim of the work presented in this thesis is to investigate the effect of DDE cosmologies on LSS. I have discussed the theoretical background to DDE and LSS statistics as well as covered some of the observation methods employed to constrain DDE in Chapter 1. With that in mind, I will discuss my approach to generating theoretical LSS predictions in this chapter.

On very large scales one can use linear perturbation theory to calculate the distribution of matter. However, most LSS statistics require accurate modeling on non-linear scales for which this approach is inadequate. A more common approach is to use collisionless simulations to calibrate the so-called “halo model” (Peacock and Smith, 2000; Seljak, 2000; Cooray and Sheth, 2002; Mead et al., 2015), or to use these simulations to empirically correct linear perturbation models (e.g., Takahashi et al. 2012). These approaches, which can be accurate to $\approx 5\%$, are likely to be insufficient for the next generation of observational surveys like LSST (LSST Dark Energy Science Collaboration, 2012) and Euclid (Amendola et al., 2013), which aim to be able to measure statistics, such as the non-linear matter power spectrum, to within percent level accuracy (Huterer, 2002; Huterer and Takada, 2005; Hearin et al., 2012). Additionally,

baryons contribute a significant fraction of the total matter content of the Universe that is not modelled beyond the expansion history in the methods mentioned above. It has been shown that baryonic feedback processes not only affect the spatial distribution of baryons but also induce a back-reaction onto the dark matter distribution that should not be ignored (van Daalen et al., 2011; Velliscig et al., 2014; Mummery et al., 2017; Springel et al., 2018; Chisari et al., 2018; McCarthy et al., 2018; van Daalen et al., 2020). Hence, hydrodynamical cosmological N-body simulations are the only method that can model the matter distribution accurately and self-consistently down to highly non-linear scales as well as accurately include the effects of baryons. The work presented in this thesis makes extensive use of hydrodynamical cosmological simulations to generate predictions of LSS.

In this chapter, I present an overview of cosmological hydrodynamic simulations and in the latter half the specific setup used in this work. Specifically, I cover methods to model collisionless matter in Section 2.1.1, hydrodynamical modeling in Section 2.1.2 and the role of subgrid physics in Section 2.1.3. I cover the suite of simulations used in this work, BAHAMAS, in detail in Section 2.1.5 and explain the approach used to generate DDE cosmologies to simulate in Section 2.2. The analysis of those simulations is presented in Chapters 3 and 4.

2.1.1 Gravity solver

One of the main building blocks of cosmological simulations is the force of gravity. For N-body simulations, which follow only collisionless particles, gravity is the only force that affects the equations of motion of each particle. Given a set of N particles with mass of unity, positions, \bar{x}_i , and velocities, \bar{v}_i , the equations of motion at time t can be written as

$$\bar{v}_i = \frac{d\bar{x}_i}{dt}, \quad (2.1)$$

$$\bar{F}_i = \frac{d\bar{v}_i}{dt} = -\nabla\phi, \quad (2.2)$$

$$\nabla^2 \phi = 4\pi G \rho(\bar{x}, t). \quad (2.3)$$

Here, \bar{F}_i is the force on particle i due to the gravitational potential, $\bar{\phi}$, which depends on the density through the Poisson equation, Equation 2.3. Variables with an overline denote vector quantities.

The equation of motion above are with respect to physical coordinate. To show how DE affects the motion of particles, one can derive the peculiar velocity, $\bar{v} = \frac{d\bar{x}}{dt}$, from comoving coordinates, $\bar{r} = \frac{\bar{x}}{a}$, where a is the scale factor.

$$\bar{v} = \frac{d\bar{x}}{dt} = \bar{r} \frac{da}{dt} + a \frac{d\bar{r}}{dt} \quad (2.4)$$

By substituting the definition of the Hubble parameter from the Friedman equations (Equation 1.2) into Equation 2.4,

$$\bar{v} = Ha\bar{r} + a\bar{u} = H\bar{x} + a\bar{u}, \quad (2.5)$$

one arrives at an equation for the velocity that includes the peculiar velocity, $a\bar{u}$, and a ‘‘Hubble drag’’ term, $H\bar{x}$, which is how DE enters the equations of motion.

The equations of motions above are relatively simple, first-order ordinary differential equations that can be solved by numerically integrating the equations of motion in finite time steps. A popular integration method for this is the second-order ‘leap-frog’ integration which is a very lightweight and stable integration method that does not suffer from long-term error drift for oscillating systems, unlike the popular Runge-Kutta 4 method.

To evaluate the position and velocity of a i^{th} particle at a new time, $t_1 = t_0 + \Delta t$, using the leap-frog integration, one can evaluate the force at half the time-step, $\Delta t/2$, first;

$$\bar{x}_i(t_{1/2}) = \bar{x}_i(t_0) + \bar{v}_i(t_0)\Delta t/2, \quad (2.6)$$

$$\bar{F}_i(t_{1/2}) = \bar{F}[\bar{x}_i(t_{1/2}), t_0 + \Delta t/2]. \quad (2.7)$$

Using the force at the half time-step, it is possible to evaluate the position and velocity at t_1 ,

$$\overline{v}_i(t_1) = \overline{v}_i(t_0) + \overline{F}_i(t_{1/2})\Delta t, \quad (2.8)$$

$$\overline{x}_i(t_1) = \overline{x}_i(t_0) + (\overline{v}_i(t_0) + \overline{v}_i(t_1))\Delta t/2. \quad (2.9)$$

The only thing that is unknown in the equations above is a method for calculating the force on a particle. Since gravity is a long-range force, it is necessary to evaluate the gravitational force on a particle, i , given every other particle, j , in the simulation. The simplest way of achieving this is by summing the force contribution of all other particles through

$$\overline{F}_i = -G \sum_{j \neq i} \frac{\overline{x}_i - \overline{x}_j}{|\overline{x}_i - \overline{x}_j|^3}. \quad (2.10)$$

This becomes very expensive as the number of particles increases since the distances between all particles need to be calculated, making this method $O(N^2)$ for N particles.

In an alternative method proposed by Barnes and Hut (1986), the particles are placed into a data structure called an oct-tree (for 3D) based on their position. Oct-trees are a set of cells that each contain more cells and/or particles, where the top-most cell is simply the simulation box. Each cell has one function; if it contains more particles than a number n (where the originally proposed method had $n = 1$), it splits into 8 equally sized cells (with width of half the parent cell) and places its particles into the appropriate new cells based on their position. Once the oct-tree has been constructed, each cell contains either no particles, n particles, or a reference to its child-cells. In the latter case, the cell also contains the monopole and quadrupole moments of all the particles that lie within its child-cells (i.e. within its physical boundaries). To calculate the force on a particle, one can use the explicit method in Equation 2.10 for any other particles within its own cell, if any, as that number will be small. For the remaining particles, the algorithm ‘walks’ the tree, starting at the top-most cell, and evaluates the

condition $r > l/\Phi$, where r is the distance from the current particle to the centre-of-mass of the cell, l is the cell width, and Φ is an accuracy parameter usually called the opening angle. If the condition is met, the force contribution of all particles within that cell are approximated using multipole expansion. Else the algorithm repeats the above condition for each child-cell. This oct-tree method is significantly faster than the explicit method in Equation 2.10, scaling approximately as $O(N\log N)$. It also has the benefit of having a defined effective accuracy parameter, the opening angle, which ensures that the error on the force calculation does not become too large.

The last method discussed here is the particle-mesh (PM) method. To calculate the gravitational forces between a distribution of particles using this method, the particles are assigned to cells on a uniform grid. A popular method to achieve this is the cloud-in-cell assignment (Hockney and Eastwood, 1981). Once the mass of all particles have been assigned to cells, the forces can be calculated using Fourier transforms,

$$\phi_k = -4\pi G \frac{\rho_k}{k^2}, \quad (2.11)$$

$$\overline{F}_k = -i\phi \overline{k}, \quad (2.12)$$

where $\overline{\rho}_k$ is the Fourier transform of the density in the cells and the force in each cell is the Fourier transform of \overline{F}_k . The force on each particle can then be obtained by interpolating the forces in each cell appropriately using the particle positions. This method is much faster, scaling approximately as $O(N)$, but the force resolution is fixed and set by the size of the grid. Therefore, a high resolution grid is required to resolve small scale interactions.

2.1.2 Gas dynamics

The above methods are sufficient to model the dark matter content of the Universe. However, the more complex interactions of baryonic matter need to be included to get close to accurate predictions of physical observables. Baryonic matter is usually

modeled as an ideal fluid with the following set of equation that describe its evolution;

$$\frac{d\bar{v}}{dt} = -\frac{\nabla P}{\rho} - \nabla\Phi, \quad (2.13)$$

$$\frac{d\rho}{dt} + \rho\nabla\bar{v} = 0, \quad (2.14)$$

$$\frac{du}{dt} = -\frac{P}{\rho}\nabla \cdot \bar{v}. \quad (2.15)$$

These are the Euler equation, continuity equation and the first law of thermodynamics, respectively, where P is the pressure and u is the internal energy. Φ is the gravitational potential solved by a gravity solver described above.

There exist two separate schools of thought when it comes to solving these equations in cosmological simulations. The Eulerian approach discretizes space in a type of grid where cells store the values of conserved quantities (mass, momentum and total energy) and evolves the hydrodynamic equations by computing fluxes of primitive quantities (e.g. density, velocity and pressure) across the cell boundaries. This approach can accurately model shocks and dynamic instabilities in the gas but tends to fail at conserving scalar properties.

The second approach is the Lagrangian method of which smoothed particle hydrodynamics (SPH) is the most popular method. In SPH, the fluid is equally discretized in mass, where quantities are attached to particles and smoothed over a spherically symmetric kernel function. These kernels have a characteristic radius, a smoothing length, which typically depends on and scales inversely with the local density, such that low density regions smooth quantities over larger volumes. The smoothing length is usually set to be the minimum distance required for the kernel to encompass a set number of neighbouring particles, where the search for nearest neighbours can be conveniently combined with the oct-tree method described above. This convenient integration with particle-based gravity solvers makes SPH an attractive choice, achieving high resolution in dense regions (which often coincide with regions of interest such as galaxies). On the other hand, SPH does not work well in low-density regions due to the small

number of particles. Additionally, SPH cannot properly deal with shock fronts and fails to accurately model fluid mixing (Morris, 1996; Dilts, 1999; Ritchie and Thomas, 2001; Marri and White, 2003; Okamoto et al., 2003; Agertz et al., 2007; Kitsionas et al., 2009; Price and Federrath, 2010; Bauer and Springel, 2012; Sijacki et al., 2012). To combat the latter, an artificial conductivity or diffusion term can be introduced to mix quantities between neighbouring particles (Price, 2008; Wadsley et al., 2008).

2.1.3 Subgrid physics

Subgrid physics form a crucial components of cosmological simulations. I have described methods for modeling the gravitational forces and hydrodynamics of matter above, but there are a host of other astrophysical processes that these do not describe. The most limiting factor in cosmological simulations is that they model vast volumes of the Universe, therefore many astrophysical processes cannot be fully described since their interaction scales fall below the simulation's resolution scale (which can be of the order of ~ 1 kpc). The job of subgrid physics is to approximate the most important astrophysics in order to gain extra detail and produce more accurate theoretical predictions. I will cover some of the popular subgrid physics below.

The simulation methods described so far follow the properties of dark matter and baryons but do not include a prescription for radiation. Radiative cooling is implemented in most cosmological simulations and describes the cooling of primordial gas, consisting of hydrogen and helium, but more recently also includes cooling from metal-line emission. Computing the radiative cooling from the primordial gas is relatively simple and can be done on the fly, whereas metal-line cooling is more complex and one usually resorts to using pre-computed lookup tables (Katz et al., 1996). This radiative cooling allows gas to dissipate its potential energy and form dense regions. Additionally, photoionizing heating is also included which becomes very important for the era of reionisation and for the feedback processes outlined below. Usually, the era of reionisation is modeled by an ionising background radiation field that is simply 'turned on' at an appropriate redshift.

Another aspect of the Universe that has so far been ignored are the stars, whose lives can be split into three separate stages: star formation, stellar evolution and stellar death. The conditions for star formation require regions of cold, dense gas. Since gas is allowed to cool through radiative cooling and collapse into high density regions, these conditions should exist. However, the scales and complex physical processes of dense molecular clouds that determine star formation are still outside the reach of cosmological simulations. Therefore, empirical recipes serve as approximations to convert cold, dense gas into stars (Katz et al., 1996; Springel and Hernquist, 2003). In practice, gas particles in the simulation can undergo star formation if the right criteria are met, and turn into a new collisionless star particle that traces an entire stellar population. The criteria for star formation usually try to replicate the Kennicutt-Schmidt law which links gas density to star formation rate density (Schmidt, 1959).

Each stellar population can then evolve based on its mass, age and the chemical composition inherited from its gas particle. The stellar populations enrich the gas which becomes important for the metal-line cooling rates (Wiersma et al., 2009a).

Finally, the death of stars forms a crucial process in cosmological simulation. Supernovae and stellar winds from massive stars inject large amounts of energy and distribute metals into the surrounding gas. This energy injection causes galactic outflows of gas that help in dealing with the problem known as overcooling, a process in which too much gas is allowed to cool and form stars (see, e.g. Balogh et al. 2001). The overcooling problem results in a large fraction of baryons that are locked up in cold gas or stars which is significantly larger than observed values. The injected energy from supernovae heats the surrounding gas and stops it from collapsing into stars.

Relatively recently, black holes (BH) have become another corner-stone in modern cosmological simulations (e.g. see Sijacki et al. 2008 and references therein). At the centres of galaxies, there are thought to be supermassive BHs that give rise to active galactic nuclei (AGN) which accrete matter onto them and emit large amounts of high energy radiation, winds and jets. These causes the surrounding gas to heat up and drive galactic outflows that are more powerful than those created by supernovae. The combination of supernovae and AGN feedback is sufficient to counteract the overcool-

ing problem. The BHs can be implemented in the simulation as their own particle type (which results in a total number of four particle types; dark matter, gas, stars and BHs). So-called seed BH particles can be placed in any halo over a mass threshold and grow by accreting gas particles and merging with other BHs.

The final aspect of subgrid physics concerns the model parameters themselves. Some of the implementations of the astrophysical processes have forms that are too far removed from physical/observational analogue models and contain model parameters for which no observational equivalent exists. That means that some subgrid physics has to be calibrated. A typical calibration strategy is to choose a set of statistics, such as the stellar mass function, and vary the subgrid parameters until the simulation reproduces those statistics, as done in e.g. Illustris (Vogelsberger et al., 2013; Torrey et al., 2014), EAGLE (Crain et al., 2015), BAHAMAS (McCarthy et al., 2017) and IllustrisTNG (Pillepich et al., 2018). Of course these statistics cannot now be used as direct predictions. However, the philosophy is that if a set of fundamental relations can be matched then the subgrid physics accurately reproduces physically meaningful results and any other measured statistics are reliable theoretical predictions.

2.1.4 Initial conditions

Initial conditions (ICs) form an integral part of most simulations. In cosmological simulations, the aim is usually to create a distribution of particles with positions and velocities that have the same characteristics as the early Universe. An obvious choice is to use information from the CMB which can be described by its power spectrum and is motivated by the theoretical expectations that the early Universe resembles a Gaussian random field very closely (Bardeen et al., 1986). It is possible to generate a Gaussian random field with a given power spectrum with

$$\hat{\delta}_k = \sqrt{-2P(|k|)\ln(A)}e^{i\phi}, \quad (2.16)$$

where $\hat{\delta}_k$ is the density contrast in Fourier space and $P(|k|)$ is the desired power spec-

trum. A is a random number in the range $[0, 1]$ and ϕ is the phase given by a random number between $[0, 2\pi]$. This density can then be converted into a potential on a grid, $\Phi(\bar{x})$, in real space using

$$\Phi(\bar{x}) = \sum_k \frac{\hat{\delta}_k}{k^2} e^{i\bar{k}\cdot\bar{x}}. \quad (2.17)$$

Now particles can be assigned positions and velocities from the potential using the Zel'dovich approximation (Zel'dovich, 1970).

A choice to consider in generating ICs is the original distribution of particles onto which to imprint the desired power spectrum. One choice would be to use a regular lattice. For high density regions, the highly non-linear nature of gravitational structure collapse destroys any regularity in the original particle distributions. However, low density regions retain some of the regularity from the original lattice that could be undesirable. This effect has been claimed to be purely aesthetic and studies have looked into whether these significantly impact statistics of interest (see e.g. Joyce et al. 2005). The other option is to use a particle distribution known as a 'glass'. This can be generated by taking a random particle distribution and running a simulation for which the sign of the acceleration is reversed, i.e. the particles experience repulsive forces rather than attractive. Evolving such a system, including a damping of the velocities, over a long time until it reaches a relaxed state results in a 'glass-like' particle distribution that can be used for IC generation. This glass distribution has regularly spaced particles but does not contain the uniformity of a lattice.

To generate a power spectrum, one could use the fitting function of Eisenstein (1997). However, a more accurate approach is to use any of the publicly available 'Boltzmann' solvers (e.g. CAMB (Lewis et al., 2000) or CLASS (Lesgourgues, 2011)). These codes linearly evolve the power spectrum of primordial fluctuations to a specified redshift given a set of cosmological parameters.

The last thing to consider is the time, or redshift, at which to generate the ICs. It is of course beneficial to start the cosmological simulations at the lowest possible redshift

to save on computing time, assuming that the aim is to study the structure at present day. However, the method outlined above is only valid for linear power spectra. In other words, once structure collapses and becomes highly non-linear and therefore non-gaussian, even if one could generate an accurate non-linear power spectrum, the method above would fail to produce the right particle distributions from that power spectrum. It is possible to correct the Zel'dovich method above using Lagrangian perturbation theory which allows for more accurate initial particle positions and velocities, and allow for a lower starting redshift compared to the simple Zel'dovich approximation (see, e.g. Hahn and Abel 2011 and references therein).

2.1.5 BAHAMAS

With the core cosmological simulation methods outlined above, I now describe the BAHAMAS suite of simulations which are used exclusively in the work presented here. BAHAMAS is a set of cosmological hydrodynamical simulations that aim at studying the properties of massive dark matter haloes and their associated groups and clusters of galaxies. Therefore it uses a relatively large box size of $400 \text{ comoving Mpc } h^{-1}$ on a side and containing 2×1024^3 particles, equally split between dark matter and baryons. This enables BAHAMAS to be used as theoretical prediction of LSS in order to test cosmology.

The BAHAMAS simulations are descendants of the Overwhelmingly Large Simulations (OWLS) project, and the later cosmo-OWLS project, and share many of its physics implementation. The simulations use a modified version of GADGET3 (last described in Springel 2005), which uses a hybrid Lagrangian oct-tree and particle mesh method to solve gravitational forces and SPH for the hydrodynamics. The hybrid gravity solver uses an oct-tree to calculate the gravitational forces for relatively small separations and the particle mesh for large separations. While particle mesh methods are generally faster than tree methods, this hybrid approach allows the forces on small separations (where accuracy is most important) to be calculated with a defined error tolerance, and benefit from faster computation on large scales. In fact, the particle

mesh also benefits from an accuracy boost over the tree method as the constant mesh cell size will be smaller than the tree cells on the largest scales. `GADGET3` was also modified to include new subgrid physics as part of the OWLS project (Schaye et al., 2010).

The simulations include a subgrid prescription for radiative cooling and heating that follows the prescription in Wiersma et al. (2009b), where rates are computed element by element. These rates are then interpolated as a function of density, temperature and redshift from a pre-computed table that was generated using `CLOUDY` (last described in Ferland et al. 1998). These cooling and heating rates account for the CMB radiation and a background of X-ray and ultraviolet photoionising radiation, described by Haardt and Madau (2001). The era of reionisation is modeled by simply adding a background radiation field at $z = 9$. As mentioned in Section 2.1.3, cosmological simulations lack the resolution to follow the cold, dense gas needed for star formation. Therefore, dense gas with $n_H > 0.1 \text{ cm}^{-3}$ is given an effective equation of state of $P \propto \rho^{\frac{4}{3}}$. Any gas that is denser than this is allowed to undergo stochastic star formation, where the probability of converting a gas particle into a star particle is the fraction of the current time step and the gas-consumption time-scale (effectively a star formation rate) of that gas particle (Schaye and Dalla Vecchia, 2008). The stellar evolution, mass loss and chemical enrichment by Wiersma et al. (2009a) is used which models each star particle as a single stellar population with a Chabrier (2003) initial mass function. It traces 11 elements that significantly affect radiative cooling rates by distributing ejected mass, from Type II and Ia supernovae and Asymptotic Giant Branch stars, over the star particle's neighbours using the SPH kernel. The simulations also include subgrid models for stellar and AGN feedback. Stellar feedback is implemented using the model of Dalla Vecchia and Schaye (2008), where neighbouring gas particles have a probability of receiving a kinetic kick from the star particle. A new star particle is allowed to produce stellar feedback after 30 Myr, corresponding to the maximum lifetime of stars that eventually undergo a core-collapse supernova. Kicked gas particles are never hydrodynamically decoupled from the surrounding gas and are not allowed to undergo star formation for 15 Myr to avoid high velocity star ejection.

The BH growth and AGN feedback, which is included by default for BAHAMAS but was not for OWLS, is implemented following the prescription of Booth and Schaye (2009) (which is a modified version of the model originally developed by Springel et al. 2005). BH seeds of mass $m_{\text{seed}} = 9 \times 10^4 M_{\odot}$ are placed in the centres of potential of dark matter haloes with a minimum mass $m_{\text{halo,min}} = 4 \times 10^{10} M_{\odot}$. These BHs grow through the accretion of their surrounding gas and through mergers with other BHs. A BH stores up energy during mass accretion and undergoes a feedback event if it can heat n_{heat} of its neighbouring particles by a minimum temperature, T_{heat} . The conversion from accreted matter to feedback energy depends on the product of two factors: the efficiency of converting accreted matter into radiation (or alternatively the amount of matter that does not go towards growing the BH) and the efficiency at which this radiation couples to the surrounding gas.

The aspect in which BAHAMAS distinguishes itself from other cosmological hydrodynamical simulations, other than its large box size, is its calibration strategy. The main aim of the simulations is to accurately predict LSS statistics, including the matter power spectrum (see Section 1.4). The non-linear matter power spectrum resulting from collisionless DM is generally of the right form but it is the crucial inclusion and interactions of baryonic effects that produce the accurate power spectra required by observations. The way in which baryonic processes affect the matter power spectrum is by redistributing the baryonic content in dark matter haloes through stellar and AGN feedback. Therefore, the BAHAMAS calibration strategy aims to accurately capture the total baryon fraction of haloes. Since the majority of baryons are either in a hot gaseous state or trapped in stars, the aim is to reproduce the observed stellar and hot gas masses of haloes. More specifically, the calibration statistics which are calibrated are the galaxy stellar mass function and the hot gas mass fraction of groups and clusters (McCarthy et al., 2017). A further discussion of the calibration of the feedback is presented in Chapter 4.

BAHAMAS also includes an extension for massive neutrinos, described in Ali-Haïmoud and Bird (2013), that computes neutrino perturbations on the fly at every time step using a linear perturbation integrator sourced from the combined non-linear baryon and

CDM potential, adding the result to the total gravitational force. Because the neutrino power is calculated at every time step, the dynamical responses of the neutrinos to the baryons and CDM, and vice versa, are mutually and self-consistently included. I adopt the minimal neutrino mass, $\Sigma M_\nu = 0.06$ eV, in this work but the reader can refer to Mummery et al. (2017) and McCarthy et al. (2018) for the effects of more massive neutrinos. Additionally, the radiation energy density is included when computing the background expansion rate. This results in a few percent reduction in the amplitude of the present-day linear matter power spectrum relative to simulations that only include the matter and dark energy components in the background expansion rate. For the work presented here, I modified the background cosmology to include DDE as is detailed in Section 1.2. This involved modifying the calculation for the expansion history in the way shown in Equation 1.16. I explicitly confirmed that the simulations return the correct expansion rate at every time step and that the linear matter power spectra, calculated with `CAMB`, agree with the matter power spectra of the simulation on the largest scales.

I used a standard friends-of-friends (FoF) algorithm (Davis and Peebles, 1983) with linking length of 0.2 in units of mean inter-particle separation on the dark matter distribution to identify haloes. The `SUBFIND` algorithm (Springel et al., 2001; Dolag et al., 2009) was used to identify substructures within the FoF groups using a spherical overdensity method and to calculate properties such as $R_{200,\text{crit}}$, the radius of a sphere enclosing a mean density of 200 times the critical density, and $M_{200,\text{crit}}$, the mass enclosed within.

2.2 Cosmological parameter selection

A great deal of effort has been invested in devising methods that can constrain cosmological models from observed quantities. The difficulty of this comes with the fact that most cosmological models present a high dimensional parameter space and observational data comes from a variety of different observables that would ideally be combine to give a joint constraint on cosmological parameters. This is often achieved

using Markov-Chain Monte-Carlo (MCMC) methods, which have gained wide-spread use throughout cosmology and the larger astrophysics community. The MCMC algorithm is built on Bayes Theorem and has been widely covered in the literature. I will give a brief, conceptual outline here but the interested reader should refer to Sharma (2017) for a more formal and thorough discussion.

Equation 2.18 is Bayes Theorem where, in the context of cosmology, we have the posterior probability density function (PDF), $P(\theta|d)$, of a set of parameters, θ , given some data, d .

$$P(\theta|d) = \frac{P(d|\theta)P(\theta)}{P(d)} \quad (2.18)$$

We usually want to find θ for which the posterior PDF is at its maximum. The posterior PDF is calculated using the likelihood function, $P(d|\theta)$, the prior probability distribution, $P(\theta)$, and the marginal likelihood, $P(d)$. $P(d)$ is simply a normalisation constant that normalises the posterior PDF to unity and without it the posterior PDF would not be a probability. $P(d)$ is sometimes omitted for practical purposes as finding the maximum of the un-normalised posterior is still possible. $P(\theta)$ represents the prior knowledge on the parameter. A simple example of a prior would be the prior knowledge that a parameter, θ_1 , has to lie within some range, θ_{\min} and θ_{\max} . This is sometimes called a flat prior and would be expressed with $P(\theta_1) = 1$ in the range $\theta_{\min} < \theta_1 \leq \theta_{\max}$ and $P(\theta_1) = 0$ otherwise. The likelihood function is the probability of the data given the parameters.

While Bayes Theorem can be solved analytically for simple problems, more complex problems require numerical methods, such as MCMC, to approximate the posterior in Equation 2.18. MCMC places a ‘walker’ which takes steps through the parameter space and evaluates the posterior at each step. Each new step depends on the walkers current position (hence Markov-Chain) and the posterior at the new location. Usually, new proposed steps with a higher posterior probability are accepted, and those with a lower posterior probability are rejected. However, this leads the walker straight into

the nearest local maxima. Therefore, MCMC includes a random chance of accepting a new step with a lower posterior probability to stop the walker from getting stuck in local maxima and help explore the outskirts of the posterior distribution. Each step is referred to as a sample and the sequence of steps is referred to as a chain. The important property of the chain is that the density of samples, i.e. how often the walker has visited a particular area of the parameter space, is proportional to the posterior PDF. This allows the walker to map out the posterior distribution.

I used the MCMC method to explore the constraints on DDE from a variety of combinations of observational data. My aim was to find DDE cosmologies that showed a wide range of behaviours and were consistent with observation, and then run cosmological simulations of them. By understanding the allowed parameter space of DDE it would be possible to decide on a strategy with which to sample that parameter space. I was interested in generating cosmologies with a wide range of DDE parameters, in order to generate more extreme behaviours, that would allow me to study the effects of DDE on LSS. A large proportion of the work presented below has been presented in Pfeifer et al. (2020), and I have independently modified and ran the simulations as well as generated all of the plots presented.

I used `CosmoMC` (Lewis and Bridle, 2002), which is an MCMC engine, to generate chains for DDE cosmologies. The *Planck* collaboration has already published extensive parameter estimations for Λ CDM as well as a large set of extensions to Λ CDM (Planck Collaboration et al., 2018) using `CosmoMC`. Some of these chains have been made publicly available¹. However, only a limited number of chains considered the DDE cosmologies that I consider in this work. I decided to generate new chains in order to give me the freedom to choose cosmological parameter priors and the combination of observation data sets. I show the cosmological parameters and their priors in Table 2.1. Parameters with square brackets have uniform, flat priors and single valued parameters were set to that constant. I used the data from the *Planck* 2015 data release as this was the latest release at the time.

I first explore the $w_0 - w_a$ parameter space in Fig. 2.1. I used a combination of the

¹The public chains are available from the Planck wiki.

Parameter	Prior
$\Omega_b h^2$	[0.005, 0.1]
$\Omega_c h^2$	[0.001, 1.0]
$100\theta_{\text{MC}}$	[0.5, 10.0]
τ	[0.01, 0.8]
$\ln(10^{10} A_s)$	[2, 4]
n_s	[0.8, 1.2]
H_0 (km s ⁻¹ Mpc ⁻¹)	[60.0, 80.0]
w_0	[-3.0, 1.0]
w_a	[-3.0, 2.0]
$\sum m_\nu$ (eV)	0.06
N_ν	3.046
A_{lens}	[0, 2]

Table 2.1: The priors of the parameters used in the analysis with `CosmoMC`. Parameters with square brackets have uniform priors while single valued parameters are constants. From the top, the parameters are: baryon energy density, cold-dark-matter energy density, approximation to the observed angular size of the sound horizon at recombination, optical depth of reionisation, amplitude of scalar fluctuations, scalar spectral index, Hubble constant, two parameters defining the equation of state of dark energy (see Section 1.2), sum of neutrino masses, effective number of relativistic degrees of freedom, and the amplitude of the CMB lensing power spectrum.

Planck CMB temperature power spectrum (TT) and the polarisation power spectrum at low multipoles (lowTEB) (Planck Collaboration et al., 2016a); a combination of BAO data from the SDSS Main Galaxy Sample (Ross et al., 2015), the Baryon Oscillation Spectroscopic Survey (BOSS), BOSS CMASS and BOSS LOWZ (Anderson et al., 2014), and the six-degree-Field Galaxy survey (6dFGS) (Beutler et al., 2011); the supernova Ia constraints from the Joint Light-curve Analysis (JLA) data (Betoule et al., 2014); and the constraints on H_0 from measurements of the local Universe (Riess et al., 2011). I plot the 1σ and 2σ contours in the w_0 - w_a parameter space for different combinations of data sets. I over-plot individual samples as points which are coloured by their H_0 value. The cosmological constant, $w_0 = -1$, $w_a = 0$, is indicated by the crossing of the dashed lines. Each of the contours have different sizes but they generally follow the same shape. The *Planck* TT+lowTEB data (top left) gives a broad constraint with H_0 spanning a wide range of values, constrained by the prior on H_0 rather than the CMB data, that change in the direction perpendicular to the gradient of the contour. Adding BAO to the CMB data (top right) significantly reduces the allowed parameter space and limits the contour to lower values of H_0 . It is interesting to note that the cosmological constant sits outside of the boundary of the 1σ contour for both of the contours. Adding JLA SNIa data (bottom left), the parameter space is further reduced along the degeneracy to a narrow region, cutting out the lower H_0 values. However, adding the local H_0 constraints instead of the JLA SNIa data (bottom right), has a much smaller effect on the allowed parameter space with almost no difference. The general shape of the degeneracy can be explained by the fact that the main constraining power of the *Planck* data on dark energy comes from the distance to the surface of last scattering. Therefore, the CMB data allows any expansion history as long as its integral returns the measured distance to the surface of last scattering. This also explains why the inclusion of BAO or type Ia supernovae significantly increases the constraining power on the $w_0 - w_a$ parameter space, as they effectively probe the expansion history, $H(a)$.

It is important to note the possibility of remaining systematics in the CMB data. There exists an apparent enhanced smoothing of peaks and troughs in the temperature and

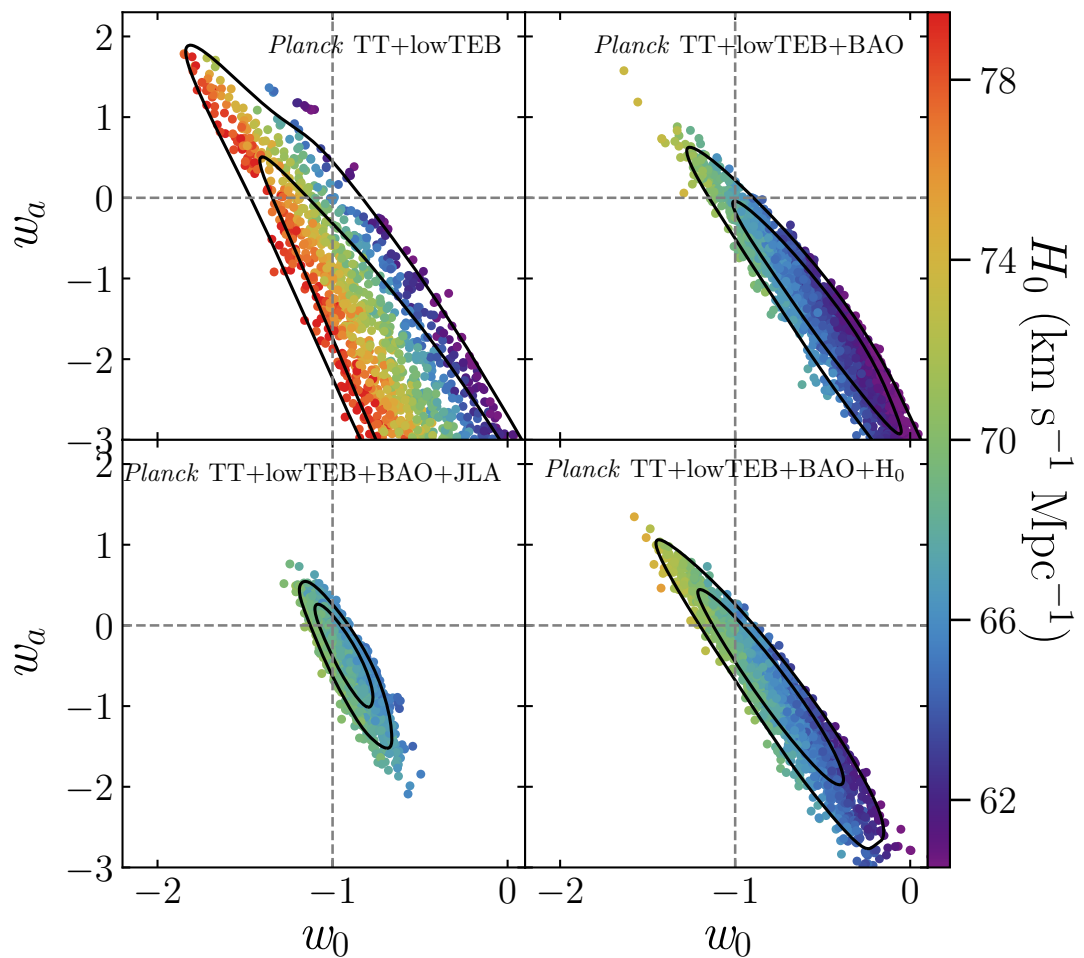


Figure 2.1: The constraints in the w_0 - w_a parameter space, in the form of 1σ and 2σ contours, from different combinations of data. *Planck* TT+lowTEB (top left) + BAO (top right) + JLA (bottom left)/+ local H_0 constraints (bottom right). Points are coloured depending on their H_0 value, the dashed lines cross at the cosmological constant and $A_{\text{lens}} = 1$.

polarization power spectrum. This has been shown by Addison et al. (2016) to result in inconsistencies between cosmological parameter derived from low and high multipole ranges. This smoothing, and the associated inconsistency, can be taken into account by letting the amplitude of the CMB lensing power spectrum, A_{lens} , vary in the MCMC analysis rather than setting it to unity, as done in the *Planck* analysis (see also Calabrese et al. 2008; Di Valentino et al. 2016; Renzi et al. 2018; Motloch and Hu 2018; McCarthy et al. 2018). Di Valentino et al. (2020a) have shown that the A_{lens} inconsistency has dramatic consequences on other cosmological parameters, namely the curvature of the Universe. If A_{lens} is set to unity, the CMB power spectrum prefer a closed Universe which is in strong tension with a variety of other observables. A flat Universe is recovered if A_{lens} is included as a free parameter. These results hint towards remaining systematics within the CMB data that we attempt to account for by including A_{lens} as a free parameter in our analysis. The publicly available chains for DDE cosmologies do not include A_{lens} as a free parameter.

I explore the effect of A_{lens} on the allowed parameter space in Fig. 2.2 for the $w_0 - w_a$ (top) and $\Omega_m - \sigma_8$ (bottom) parameter spaces for the *Planck* TT+lowTEB data with A_{lens} set to unity (left) and as a free parameter (right). I have included the LSS joint constraint $S_8 = \sigma_8 \sqrt{\Omega_m/0.3} = 0.77$ on the $\Omega_m - \sigma_8$ plot (dashed line) for reference (McCarthy et al., 2018). Including A_{lens} as a free parameter does not change the general shape but stretches the contour of the $w_0 - w_a$ parameter space towards lower (higher) values of w_0 (w_a). Again, it is interesting to note that the cosmological constant is in mild tension with *Planck* if A_{lens} is fixed at unity, the default value adopted by the *Planck* collaboration, but reconciled if it is included as a free parameter. For the $\Omega_m - \sigma_8$ parameter space, allowing A_{lens} to vary systematically shifts the entire contour to lower values of σ_8 and broadens the contour along the axis of σ_8 which results in a much better agreement with the LSS joint constraint, given by the S_8 parameter.

To choose the cosmological parameter for the cosmological models of DDE, I had to consider a few options. Firstly, the number of models I would investigate was mainly limited by the fact that cosmological simulations are expensive to run and thus only a limited number of them (<10) could be completed in adequate time at the chosen

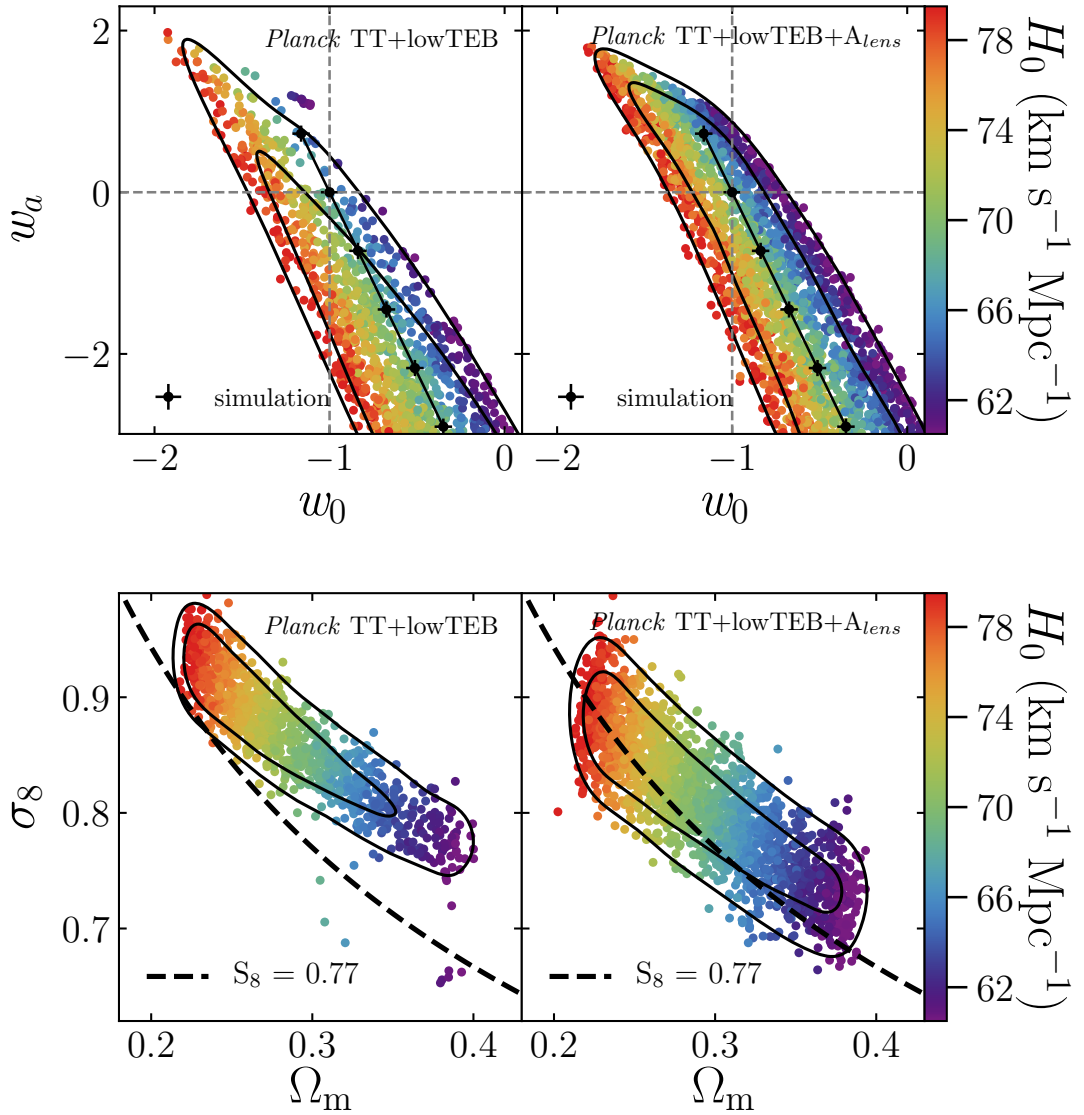


Figure 2.2: *Top*: The 1σ and 2σ constraints in the $w_0 - w_a$ parameter space using Planck TT+lowTEB data, where A_{lens} has been fixed at unity (left column) or left to vary (right column). The black points show the locations of the simulated cosmologies and the error bars on the points show the size of the region used to generate the rest of the cosmological parameters. The dashed lines cross at the cosmological constant. *Bottom*: The same as above except for $\Omega_m - \sigma_8$, where the dashed line shows $S_8 = 0.77$.

resolution. Rather than opting to probe a given cosmological parameter space with a sparsely populated grid, I decided to instead be more selective in my approach. Secondly, I had to decide on the parameter space that I wanted to sample. One option would be to pick a fiducial cosmological model and then simply vary the DDE parameters (w_0 and w_a) over a range of values while keeping the rest of the cosmological parameters fixed. This approach is rather *ad hoc* and would result in cosmologies that are neither physically-motivated nor consistent with observational constraints. I decided on using observational constraints to inform us on the allowed parameter space and identify regions of interest that I could sample. While my focus was to generate cosmologies with different DDE behaviours, i.e. generate cosmologies with large variation in w_0 and w_a , this approach allowed for rest of the cosmological parameters (e.g., H_0 , Ω_m , etc.) to be consistent with observational data by insisting that the cosmological model reproduces the chosen observational data set(s) to within some tolerance.

To generate the cosmologies for the simulations, I sampled the geometric degeneracy in the $w_0 - w_a$ parameter space shown in Fig. 2.2 and I chose the chain that includes A_{lens} as a free parameter. I opted to use the CMB data only and not add any other data set to further constrain the parameter space for several reasons: i) there are known tensions between ‘early’ (CMB+BAO) and ‘late’ (H_0) Universe measures² of the expansion history, making the combination of these constraints questionable; ii) the CMB-only (without BAO) constraints are fully compatible with any of the possible data set combinations; and iii) the CMB-only constraints allow for the largest variation in DDE models, resulting in a wider range of behaviours to study from a theoretical perspective.

I decided to run 6 simulations, one of which with a Λ CDM cosmology. I sampled the degeneracy in the $w_0 - w_a$ parameter space in Fig. 2.2 (top right) using 6 equally spaced points along a straight line, passing through the cosmological constant. All of the cosmologies are well within the 1σ contour for the parameter space that includes A_{lens} as a free parameter. I also show that most are within the 1σ , and all are within

²Type Ia supernovae constraints can agree with either, depending on how the distance scale to supernovae is established (i.e., via Cepheids or BAO) (Macaulay et al., 2019).

the 2σ contour, if I had chosen the same points in the parameter space for which A_{lens} is set to unity (see top left of Fig 2.2). Sampling the degeneracy naturally give us the values of w_0 and w_a . To generate the remaining cosmological parameters, I calculated the weighted average of each parameter from every sample of the MCMC chain that contained the values of $w_0 \pm 0.05$ and $w_a \pm 0.05$. This ensured that the entire cosmologies for all of the simulations are guaranteed to be compatible with the primary CMB angular power spectrum. The final cosmologies are given in Table 2.2 where I have set all cosmologies to be spatially flat, i.e. $\Omega_k = 0$.

Next, I introduce the terminology for the different DDE models which will be used throughout this thesis. My DDE terminology is based on quintessence models which can be classified into two categories: ‘thawing’ models start at $w \approx -1$ and have $w(a)$ increase with a (Scherrer and Sen, 2008; Chiba, 2009; Gupta et al., 2015), whereas ‘freezing’ models have $w(a)$ decrease with a and approach $w \approx -1$ at late times (Scherrer, 2006; Chiba, 2006; Sahlén et al., 2007). I adopt this terminology throughout, referring to models with $w_a < 0$ as thawing and $w_a > 0$ as freezing. I note that, although quintessence models cannot cross the $w = -1$ threshold, these models are able to do so. My terminology aims to aid the results and explanations presented here by borrowing terms from quintessence models with similar properties, even though they are strictly not the same. The evolution of $w(a)$ is shown in the top panel of Fig. 2.3. At low a (high z), the line above $w = -1$ is the freezing cosmology and the lines below are the 4 thawing cosmologies.

It is useful to first examine some physical quantities that can be calculated analytically, as these will help the interpretation of the simulation-based results later. Fig. 2.3 shows the evolution of $\Omega_m(a)$ (middle top) and $H(a)$ (middle bottom) as a function of scale factor (bottom axis) and redshift (top axis) for every cosmology, normalised by the Λ CDM cosmology. The evolution of $H(a)$ is calculated using Equation 1.16 while $\Omega_m(a)$ can be expressed as

$$\Omega_m(a) = \frac{\Omega_m a^{-3}}{H(a)}, \quad (2.19)$$

where $\Omega_{m,0}$ is the value of Ω_m at $z = 0$ for clarity. I also plot the linear growth

(1)	(2)	(3)	(4)	(5)	(6)	(7)	(8)	(9)	(10)	(11)
w_0	w_a	Ω_m	Ω_b	H_0 (km/s/Mpc)	n_s	A_s (10^{-9})	τ	σ_8	S_8	A_{lens}
-1.16	0.73	0.309	0.0501	67.25	0.975	2.10	0.058	0.773	0.783	1.298
-1.00	0.00	0.294	0.0476	68.98	0.974	2.11	0.061	0.802	0.795	1.233
-0.84	-0.73	0.288	0.0465	69.73	0.974	2.11	0.060	0.815	0.798	1.205
-0.67	-1.45	0.286	0.0462	69.97	0.973	2.10	0.059	0.819	0.801	1.195
-0.51	-2.18	0.284	0.0459	70.20	0.974	2.10	0.060	0.822	0.800	1.194
-0.35	-2.89	0.289	0.0465	69.71	0.973	2.10	0.059	0.824	0.806	1.174

Table 2.2: The cosmological parameters of the 6 chosen cosmologies derived from the *Planck* CMB data (TT+lowTEB) with marginalisation over the lensing amplitude, A_{lens} . From left to right, the parameters are: (1) and (2) the 2 free parameters describing DDE (see Equation 1.14), (3) the total matter density at present-day, (4) the baryon density at present-day, (5) Hubble's constant, (6) the spectral index of the initial power spectrum, (7) the amplitude of the power spectrum at recombination at a pivot scale of 0.05 Mpc^{-1} , (8) the optical depth to reionization, (9) the amplitude of the linear matter power spectrum on $8 \text{ Mpc } h^{-1}$ scales at present-day, (10) $S_8 = \sigma_8 \sqrt{\Omega_m/0.3}$, (11) the amplitude of the CMB lensing power spectrum.

factor, $D(a)$, for each cosmology normalised by the Λ CDM cosmology (bottom). The linear growth factor is defined as the ratio of matter overdensities at a given scale factor, $\delta(a)$, relative to some initial overdensity, $D(a) = \delta(a)/\delta(a_i)$. The closed form approximation (Peebles, 1980; Eisenstein, 1997) typically used to calculate $D(a)$ for a Λ CDM cosmology cannot be used for DDE cosmologies. Instead, equations such as those presented in Linder and Jenkins (2003a) should be solved.

The first thing to note from Fig. 2.3 is that the thawing dark energy models show systematically different behaviour to the freezing model. Any general trend in the former is the inverse in the latter, relative to the Λ CDM cosmology. The largest differences appear at $a > 0.5$ (or equally $z < 1$), as one might expect since dark energy dominates the energy density of the Universe at late times. One particularly interesting feature is that all of the cosmologies cross at the same $w(a)$ and a (top of Fig. 2.3). This is due to the method with which I originally chose the cosmological models. To show why this is, one can equate Equation 1.14 for two different cosmologies [e.g. $(w_{0,1}, w_{a,1})$ and $(w_{0,2}, w_{a,2})$] and solve for the expansion factor, a , at which $w(a)_1 = w(a)_2$:

$$a = 1 + \frac{w_{0,2} - w_{0,1}}{w_{a,2} - w_{a,1}} = 1 + \frac{dw_0}{dw_a}. \quad (2.20)$$

With equation 2.20 we can see that any DDE models that lie on the same line in the $w_0 - w_a$ parameter space (which is the case here, as I select values along the CMB geometric degeneracy in Fig 2.2) will all cross at the same value of a , with that value depending only on the slope of the line $w_0 - w_a$. This feature, along with the fact that the models are all constrained to yield the same distance to the last-scattering surface (and therefore have similar but different values for the rest of the cosmological parameters), is also likely responsible for the similar scale factors at which $\Omega_m(a)$ and $H(a)$ cross. I have separately checked that if I only vary the w_0 and w_a values, and keep the rest of the cosmological parameter fixed (in this case only Ω_m and Ω_{DE} matter), the different cosmologies cross at the same scale factor for $\Omega_m(a)$ and $H(a)$ also.

I plot the matter power spectra of the ICs for each cosmology in Fig. 2.4 to show that these cosmologies already have different matter distributions at high redshift. The

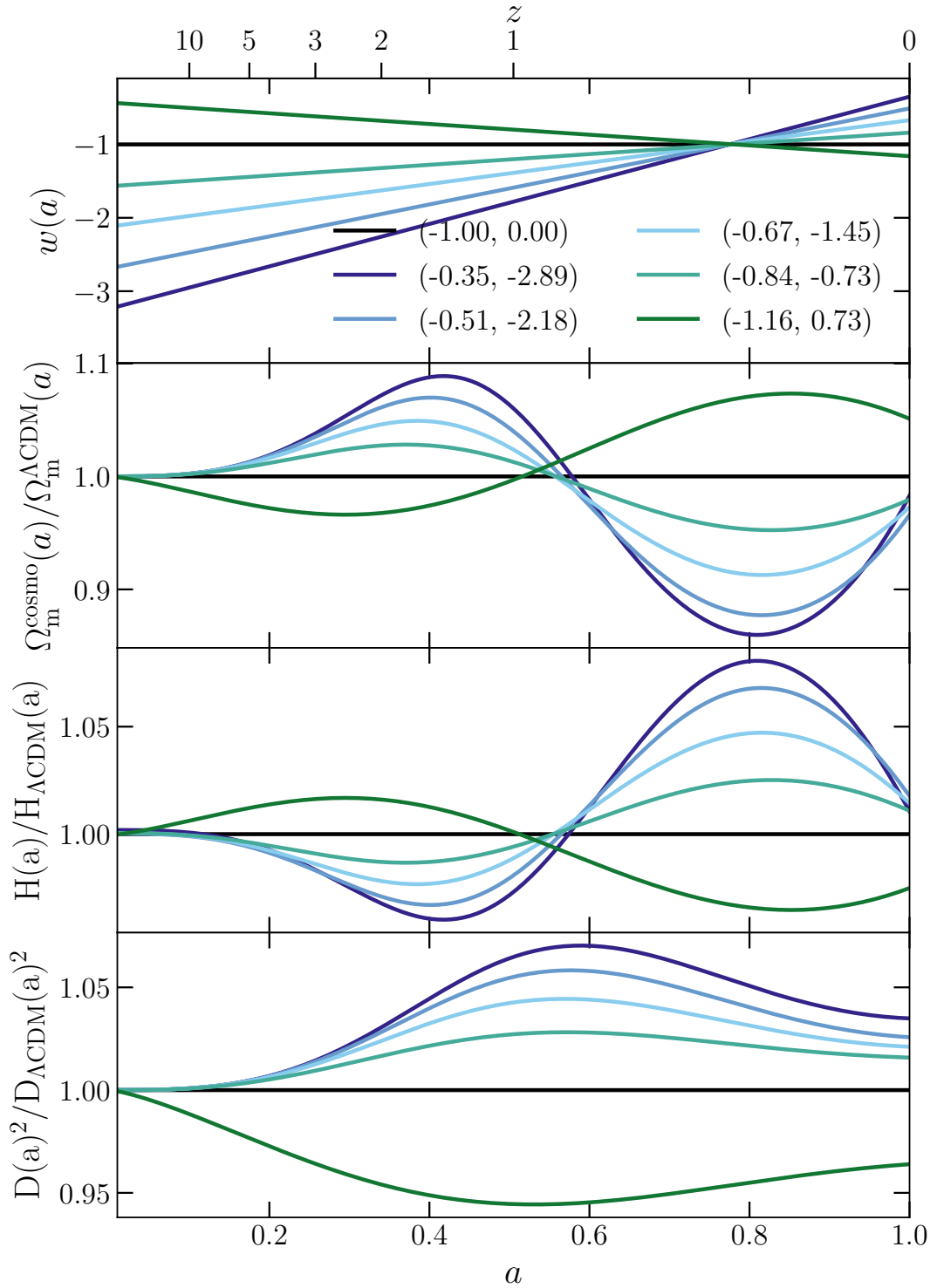


Figure 2.3: The evolution of $w(a)$ given by Equation 1.14 (top), Ω_m (middle-top), expansion history (middle-bottom) and linear growth factor (bottom) as a function of expansion factor and redshift for the cosmologies shown in Table 2.2. Each statistic, apart from $w(a)$, has been normalised by the Λ CDM cosmology. Colours indicate different cosmologies where bracketed values refer to the values of (w_0, w_a) .

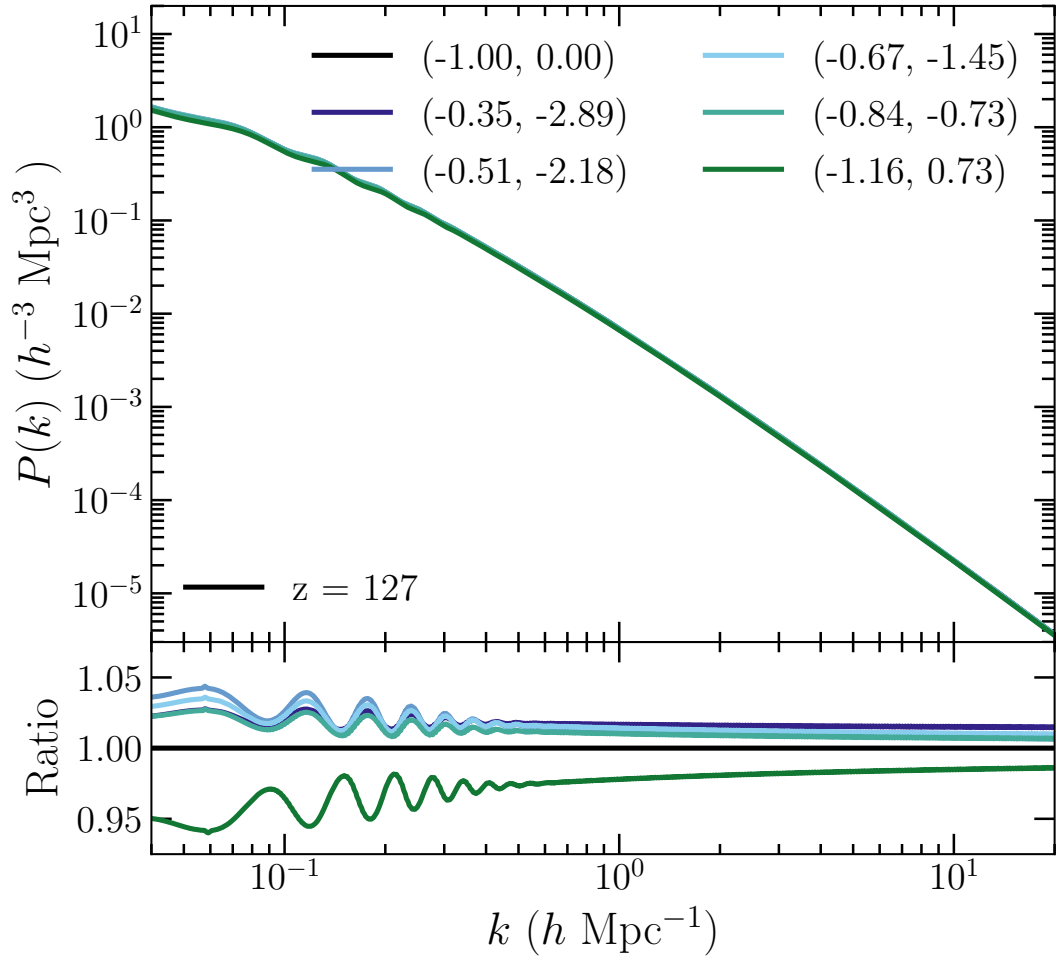


Figure 2.4: *Top:* The matter power spectrum of the ICs for each cosmology at $z = 127$ computed with CAMB. *Bottom:* The ratios of matter power spectra relative to Λ CDM. Colours indicate different cosmologies where bracketed values refer to the values of (w_0, w_a) .

power spectra were generated using `CAMB` at the simulation starting redshift of $z = 127$. The cosmologies already have a difference of $\approx 5\%$ in $P(k)$ at large scales (small k) and $\approx 1\%$ at small scales (large k) before starting the simulations. Due to slight offsets in the power spectra, the BAO signal at $k \sim 0.1$ becomes apparent in the ratios.

The work in this chapter has presented an overview of cosmological hydrodynamic simulations and covered the specific collisionless, hydrodynamic and subgrid physics treatment of the BAHAMAS simulation. I have also discussed the approach taken to generate cosmologies that aim to produce varied DDE behaviours and still be consistent with observational constraints. I have constrained the w_0 and w_a parameter space using observables that depend on metric measures only, and used these to generate 6 cosmologies that I simulate using the modified BAHAMAS simulation code. This represents a complete setup for the work done in this thesis. Following on from this, I present a range of LSS statistics from the collisionless simulations in Chapter 3 and investigate the interplay between cosmology and baryonic physics in Chapter 4.

Chapter 3

The effect of dynamical dark energy on large-scale structure

3.1 Introduction

Recent increases in the quantity and quality of observational data have revealed a number of tensions within the Λ CDM models that cannot be easily reconciled. One particular tension concerns the expansion rate of space at the present day, H_0 . Local measurements of a set of standard candles measure $H_0 = 74.03 \pm 1.42 \text{ km s}^{-1} \text{ Mpc}^{-1}$ (Riess et al., 2019) and a more recent study from the measured time delays of gravitationally-lensed quasars measured $H_0 = 73.3 \pm 1.8 \text{ km km s}^{-1} \text{ Mpc}^{-1}$ (Wong et al., 2020). These are in tension with a combined analysis of cosmic microwave background (CMB) data, baryon acoustic oscillations (BAO) and supernovae which have measured $H_0 = 67.4 \pm 0.5 \text{ km s}^{-1} \text{ Mpc}^{-1}$ (Planck Collaboration et al., 2018), culminating in a ‘early vs. late-Universe’ tension of 5.3σ (Wong et al., 2020). Another tension comes from large scale structure (LSS) joint constraints on Ω_m and σ_8 , the mean matter density of the Universe and the linearly-evolved amplitude of matter fluctuations at present day on $8h^{-1}\text{Mpc}$ scales, respectively. The *Planck* primary CMB data prefers higher values of Ω_m and/or σ_8 relative to a range of LSS data sets, typically at the $1-3\sigma$ level (e.g., Planck Collaboration et al. 2016b; Leauthaud et al. 2017; Hilde-

brandt et al. 2020; see McCarthy et al. 2018 for a recent discussion). These tensions have tended to increase in significance with new data and may hint at extra physics that is not encompassed within the standard model of cosmology.

One way of addressing these tensions is through extensions to the Λ CDM model, which typically add more complex physics and/or relax key assumptions of the model. The extension focused on in this work models DE as a dynamic scalar field (see Section 1.2) and uses the parameterisation given in Equation 1.14. This changes the expansion history of the Universe and subsequently affects the growth of structure. Therefore, the growth of LSS potentially serves as an excellent probe of dark energy that is complementary to geometric probes, such as BAO and supernovae (see Section 1.3 and Section 1.4). In addition, LSS is vital for distinguishing between DDE and modified gravity explanations for the accelerated expansion of the Universe (e.g., Li et al. 2012; Mota 2018).

In this chapter, I explore the impact of the DDE cosmologies on a number of common measures of LSS using cosmological simulations. I have carried out a new extension of the BAHAMAS simulations (see Section 2.1.5) that includes the effects of DDE. These new simulations enables me to study a range of LSS statistics including: the matter power spectrum ($P(k)$), the halo 2-point auto-correlation function, the halo mass function and halo number counts. I use the collisionless (dark matter-only) versions of the simulations (the impact of baryons is discussed in Section 4). I discuss how the DDE cosmologies affect these LSS statistics and draw comparisons (where possible) with other cosmologies constrained by the CMB which were explored in previous BAHAMAS papers; the effects of massive neutrinos (Mummery et al., 2017) (hereafter M17) and running of the spectral index (Stafford et al., 2020) (hereafter S20).

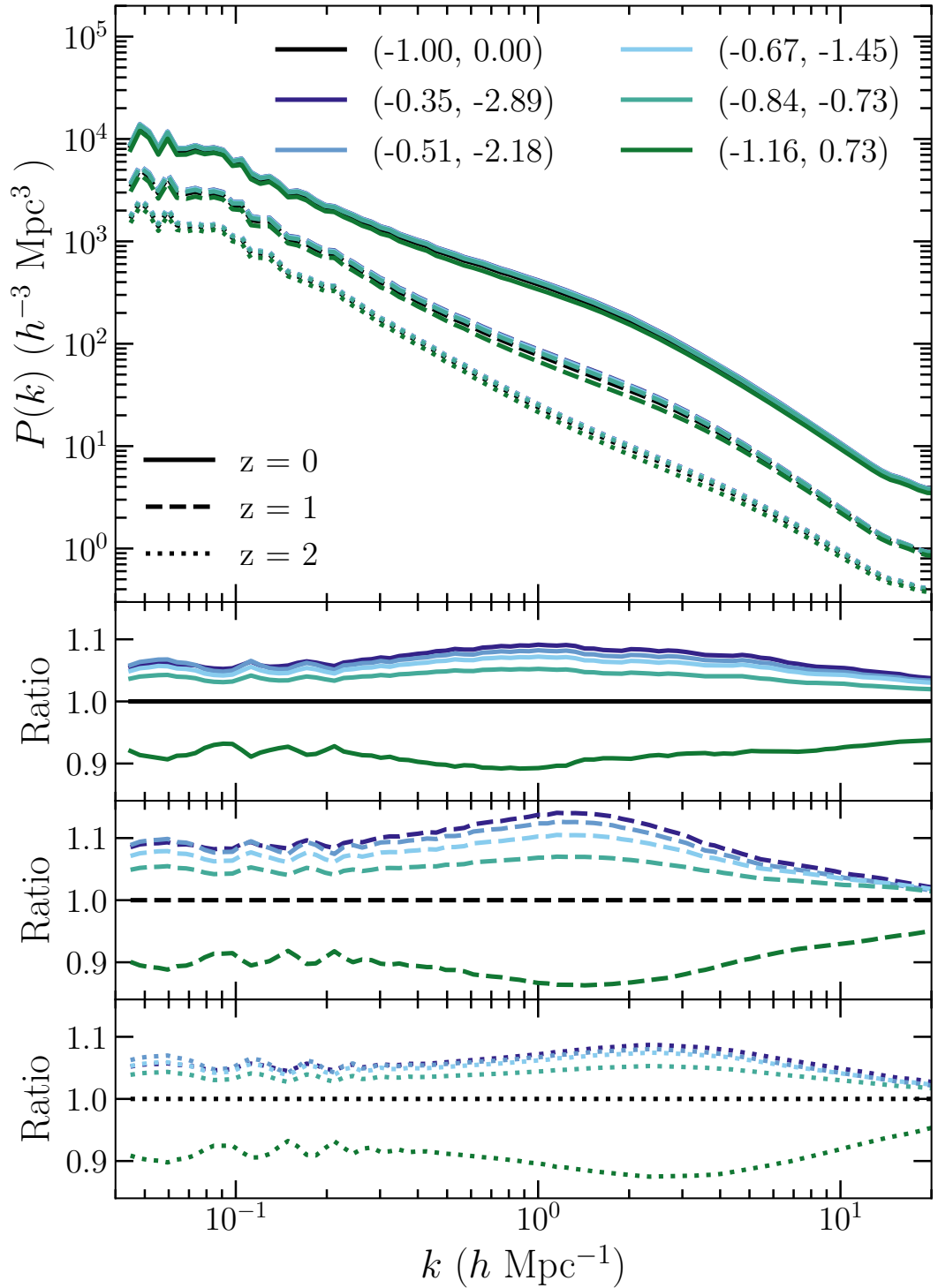


Figure 3.1: *Top*: The total matter power spectrum of the collisionless simulations for the different cosmologies and redshifts. *Bottom*: The ratios of matter power spectra relative to Λ CDM at each redshift. Colours indicate different cosmologies where bracketed values refer to the values of (w_0, w_a) while line styles show redshift.

3.2 Matter clustering

3.2.1 Matter power spectrum

I first investigate the effect of the DDE cosmologies on the matter clustering via the non-linear matter power spectrum of the total matter in the collisionless simulations. The power spectra are computed using the GenPK¹ code (Bird, 2017).

Fig. 3.1 shows the total matter power spectrum of the collisionless simulations for the different cosmologies at $z = 0, 1, 2$, where ratios have been taken with respect to the Λ CDM cosmology. Since I used the same phases to generate the ICs for each cosmology, I do not need to worry about cosmic variance issues and the ratio of $P(k)$ between two different simulations should be an accurate and robust prediction.

The freezing dark energy model shows a suppression in power of $\approx 10\%$, whereas the thawing dark energy models show an increase in power of $\approx 5-10\%$. This effect is slightly scale dependent with maximum impact at $k \approx 1 h \text{ Mpc}^{-1}$ and the largest change in $P(k)$ is seen at $z = 1$. The change in amplitude and the redshift evolution of $P(k)$ on linear scales (i.e., low k values) agrees with naive expectations based on the behaviour of $D(a)$ in Fig. 2.3. Note that the amplitude of $P(k) \propto D^2(a)$ in the linear regime. While the use of $D(a)$ is only strictly valid on linear scales, it is interesting to note that the change to $P(k)$ from DDE propagates through to non-linear scales. This can be explained through ‘mode mixing’, where k -modes no longer evolve independently from each other, but transfer power from large to small scales.

One can compare these effects to alternative extensions to the Λ CDM cosmology. M17 examined massive neutrino extensions and found that neutrinos suppress the matter power spectrum between $\approx 5\%$ and $\approx 30\%$ for the lowest, $\Sigma M_\nu = 0.06 \text{ eV}$, and largest sum of neutrino masses, $\Sigma M_\nu = 0.48 \text{ eV}$, respectively. Interestingly, the suppression in $P(k)$ from massive neutrinos has a similar shape to the DDE cosmologies in Fig. 3.1, which could act to mask a combination of massive neutrinos and DDE. Another possible extension to Λ CDM is the inclusion of a running of the scalar spectral

¹<https://github.com/sbird/GenPK>

index, n_s , which was investigated recently by S20. They found that negative (positive) running results in an amplification (suppression) of the matter power spectrum of ≈ 5 -10%. These effects had a scale dependence that caused a decrease in their magnitude towards smaller scales, especially at higher redshifts.

In addition, it is well known that baryonic effects on the matter power spectrum are of the order of ~ 10 -20% and cause a suppression in the power spectrum at $k \gtrsim 0.1 \text{ Mpc}^{-1}h$ (van Daalen et al., 2011; Mummery et al., 2017; Schneider et al., 2019; van Daalen et al., 2020; Debackere et al., 2020). The DDE cosmologies considered here produce effects of similar magnitude, although they extend throughout the linear and non-linear regime and should therefore be distinguishable from baryonic effects given a wide enough range of well-sampled k values. I explore this in Chapter 4.

3.2.2 2-point autocorrelation function

The clustering of dark matter haloes can be described by the 2-point auto-correlation function, $\xi(r)$, which is the excess probability of finding two haloes with a given separation, r , relative to a random distribution of haloes (Davis and Peebles, 1983). To compute this, one calculates the separation, r , between each halo and every other halo in the sample. The distribution of halo separations in bins of r can then be defined as $DD(r)$. The separation pair count of a random distribution, $RR(r)$, can be calculated analytically assuming the halos are distributed homogeneously with a density equal to the total number of haloes in the sample divided by the volume of the simulation. The 2-point auto-correlation function is then

$$\xi(r) = \frac{DD(r)}{RR(r)} - 1. \quad (3.1)$$

Fig. 3.2 shows the 2-point auto-correlation function for dark matter haloes in three mass bins of $M_{200,\text{crit}}$. The ratios are shown relative to the Λ CDM cosmology. In general, the freezing (thawing) dark energy cosmology produces haloes with decreased (increased) clustering relative to Λ CDM, generally mimicking the behaviour in $P(k)$.

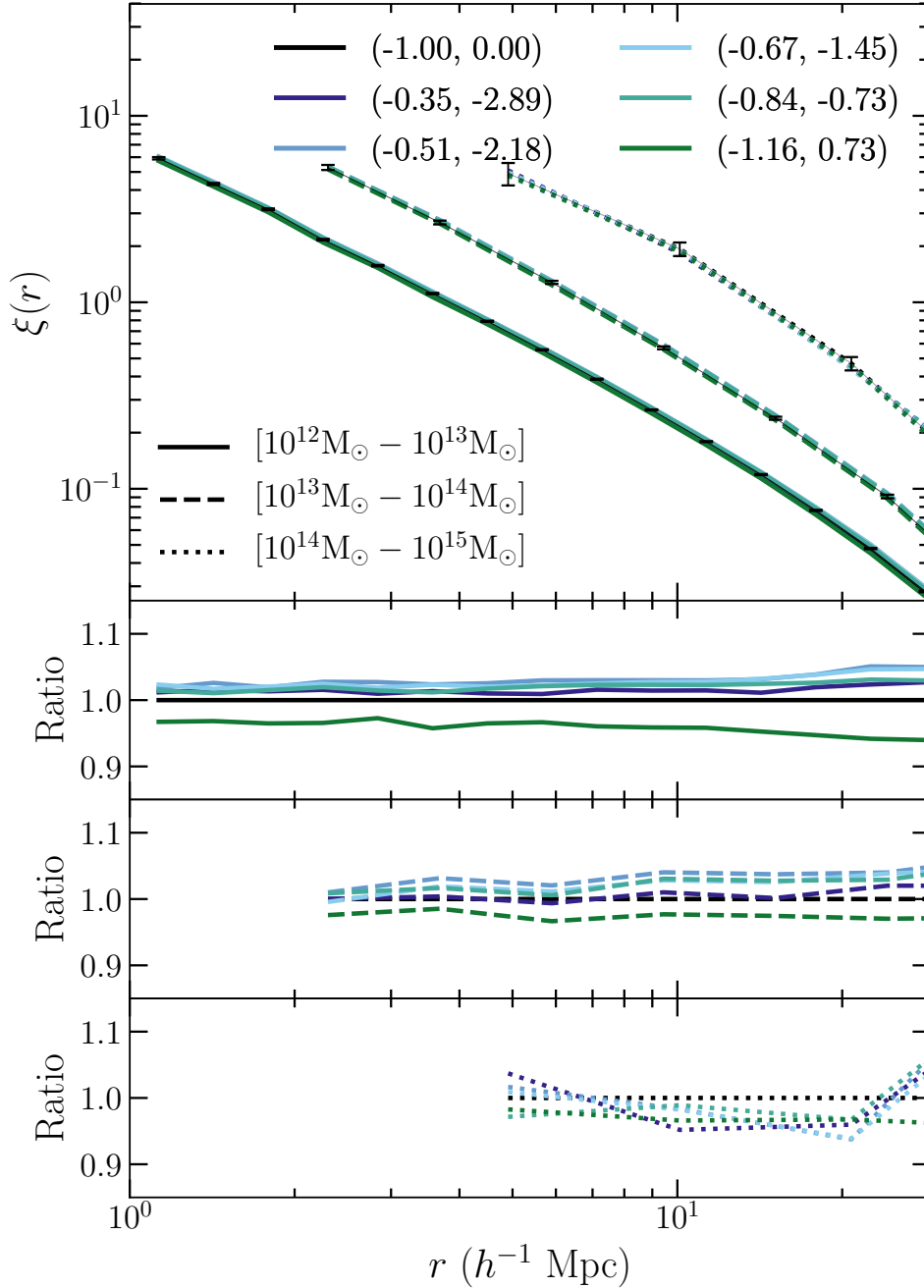


Figure 3.2: *Top*: The 2-point auto-correlation function of dark matter haloes for the different cosmologies and mass bins at $z = 0$. *Bottom*: The ratios of the 2-point correlation functions relative to the Λ CDM cosmology at different redshifts. Colours indicate different cosmologies where bracketed values refer to the values of (w_0, w_a) and line styles show separate mass bins given in $M_{200, \text{crit}}$. The cut-off at small radii is due to the overlapping of haloes which forces ξ to turn over. Error bars represent the Poisson uncertainties determined from the number of haloes in each radial bin for the Λ CDM cosmology.

The lowest mass bin shows a $\approx 10\%$ effect which decreases towards higher masses. Haloes start to overlap on small scales causing the 2-point auto-correlation function to turn over and decrease which is where I introduce a cut-off. As the size of haloes increases with increasing mass, this cut-off shifts to larger radii. I show the statistical errors on the 2-point auto-correlation function for the Λ CDM cosmology which were taken to be the Poisson uncertainties on the number of haloes in each radial bin. The errors for the other cosmologies are approximately equal to those of the Λ CDM cosmology. The uncertainties are slightly larger in bins at lower radii (as they sample smaller volumes) and for higher masses due to their lower abundance. Since I use the same phases to generate the ICs, I can compare the ratios between the different cosmologies without the complication of cosmic variance. That also means that measurements between simulations are strongly correlated. Therefore I only show the Poisson error on the absolute value and not in the lower ratio panels.

This change in the clustering of haloes is analogous to the change in the matter power spectrum, $P(k)$ seen in Fig. 3.1, which is unsurprising since the 2-point auto-correlation function is the Fourier transfer of $P(k)$ multiplied by the linear halo bias, b^2 .

The 2-point auto-correlation was also calculated for matched haloes. Matching haloes is done by identifying the 50 most bound dark matter particles comprising a halo in the Λ CDM simulation using their unique particle IDs and finding the halo in another simulation that contains the majority of dark matter particles with the same IDs. By inspecting a set of matched haloes I remove any additional effect due to the change in halo mass for different cosmologies, as seen in Section 3.3.1 below. The general trends of the 2-point auto-correlation function for matched haloes is the same as for unmatched haloes, although with increased effect due to the change in halo mass between different cosmologies. This is due to the fact that more massive haloes are more biased tracers of the underlying matter clustering and therefore show a higher clustering signal in the 2-point auto-correlation function.

M17 finds that massive neutrinos suppress the 2-point auto-correlation function of haloes with $M_{200,\text{crit}}=10^{12}M_{\odot}-10^{13}M_{\odot}$ by $\approx 5\%$ and $\approx 20\%$ for the lowest and largest sum of neutrino masses, respectively. S20 shows that their cosmologies with running

of the spectral index enhances the clustering signal by $\approx 5\%$ for negative running and vice versa for positive running for haloes within the same mass range. This is very similar to the effects of DDE which, unlike massive neutrinos, can not only suppress but also enhance the clustering signal relative to the Λ CDM cosmology.

3.3 Halo abundance

3.3.1 Halo mass function

The first statistic of halo abundance I examine is the halo mass function (HMF), Φ , defined as the number of haloes per comoving volume per logarithmic unit of mass $M_{200,\text{crit}}$,

$$\Phi \equiv \frac{dn}{d \log_{10}(M_{200,\text{crit}})}. \quad (3.2)$$

In Fig. 3.3 I show the HMF for the collisionless simulations of the different cosmologies at different redshifts, where the ratios are with respect to the Λ CDM cosmology. At $z = 0$, the freezing dark energy model has a higher (lower) number density of low-mass (high-mass) haloes, while for the thawing models this trend is reversed. These effects are most apparent at $z = 1$ where a change in the abundance of high-mass haloes of $\sim 20\%$ is seen and a crossover appears in the ratios at $M_{200,\text{crit}} \sim 10^{13} M_{\odot}$. The behaviour of the HMF is very different to that of $P(k)$, which shows no crossover and the opposite behaviour to the effect seen on low masses for the HMF. I show the statistical errors on the HMF for the Λ CDM cosmology which were taken as the Poisson uncertainties from the number of haloes in each mass bin. The errors for the other cosmologies are approximately equal to those of the Λ CDM cosmology. The uncertainties are significant at the highest masses due to the rarity of such haloes in the simulations.

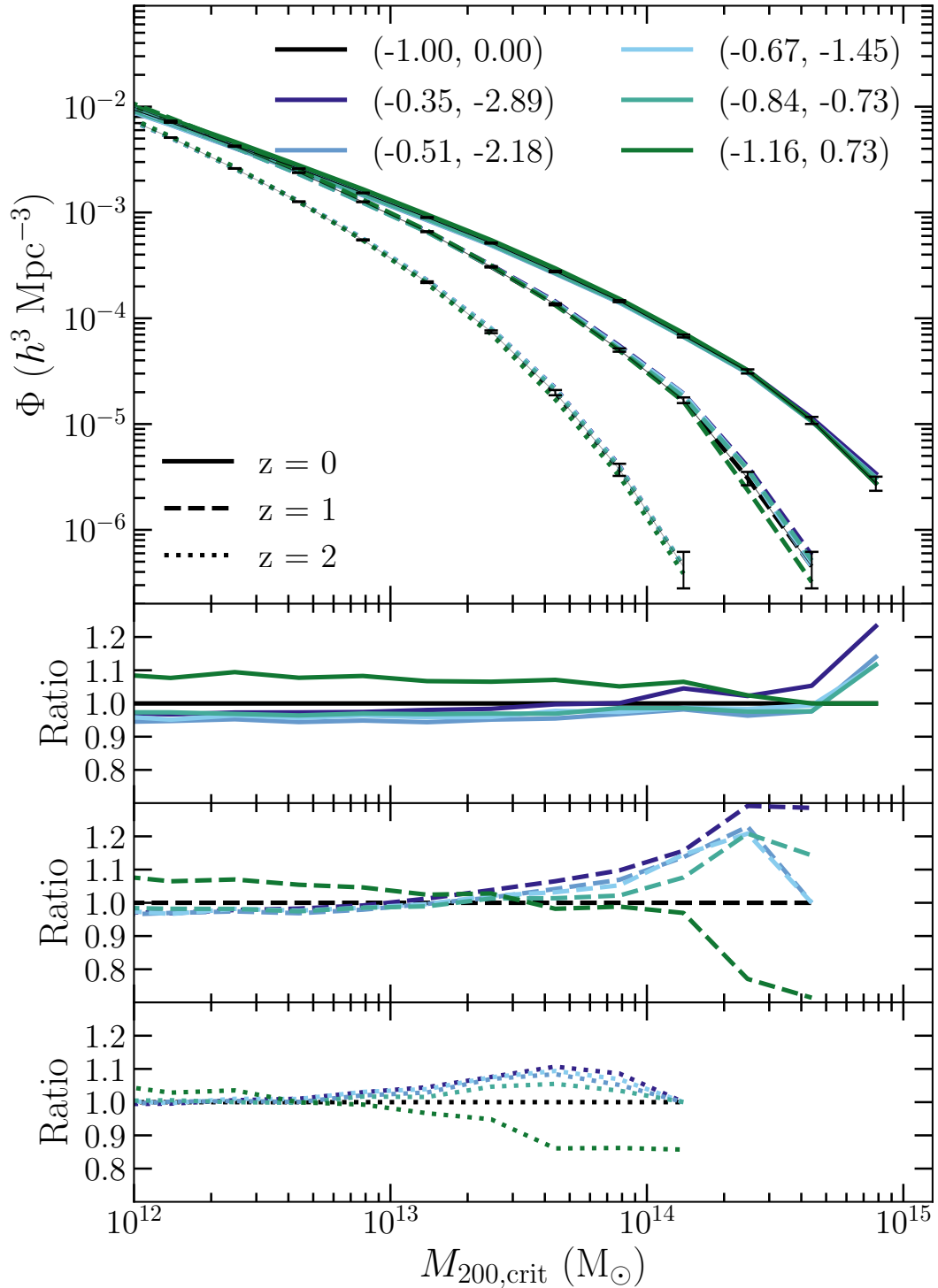


Figure 3.3: *Top:* The HMF of the collisionless (dark matter-only) simulations for the different cosmologies and redshifts. *Bottom:* The ratios of the HMFs with respect to the ΛCDM cosmology for each redshift. Colours indicate different cosmologies where bracketed values refer to the values of (w_0, w_a) and line styles indicate different redshifts. Error bars represent the Poisson uncertainties from the number of haloes in each mass bin for the ΛCDM cosmology.

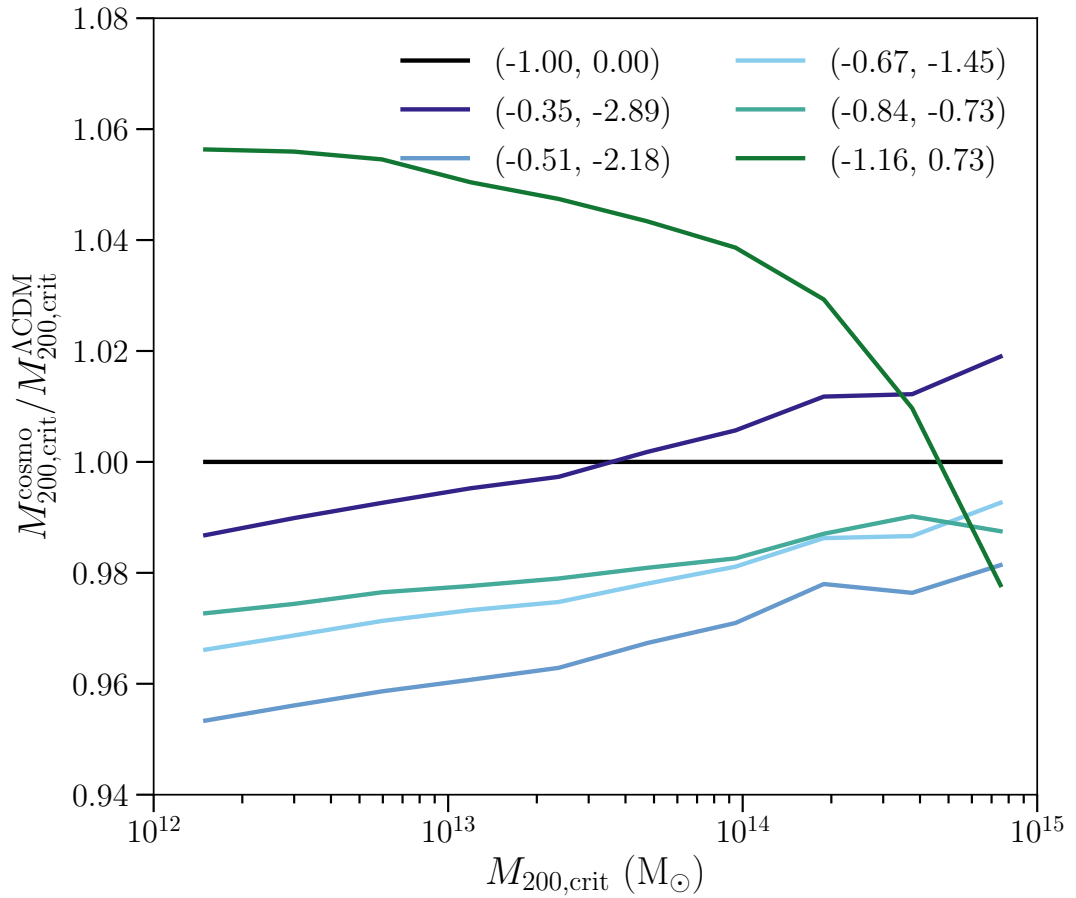


Figure 3.4: The median fractional change in halo mass relative to matched haloes from the Λ CDM cosmology at $z = 0$. All haloes have been matched to the Λ CDM cosmology. Colours indicate different cosmologies where bracketed values refer to the values of (w_0, w_a) .

Another way of looking at this effect is to plot the change in halo mass between matched haloes from different cosmologies rather than halo abundance. Fig. 3.4 shows the fractional change in halo mass relative to matched haloes from the Λ CDM cosmology at $z = 0$. This is plotted against the halo mass of the matched halo from the Λ CDM cosmology. Here I look at the change in halo mass at fixed abundance rather than changes in abundance at fixed halo mass. In this format, a vertical change in the fractional halo mass is comparable to a horizontal shift in the HMF. The trends in the HMF are also seen in the fractional change in halo mass with similar amplitude and mass scale. The freezing DDE cosmology forms more massive low-mass haloes but the growth of structure is suppressed and so the most massive haloes are not as massive as their Λ CDM equivalent. This trend is reversed for the thawing DDE cosmologies.

I can decompose the difference in the HMF between the different cosmologies into two effects. Firstly, the almost constant offset in the ratios of the HMF at the low-mass end (most apparent at $z = 0$) can be explained by the difference in Ω_m for the different cosmologies because dark matter haloes grow more massive in a cosmology with a higher Ω_m . Secondly, the crossover in the ratios at the high-mass end is due to the change in the growth of structure that is also seen in $P(k)$ in Fig. 3.1. The freezing cosmology shows a suppression in the growth of structure through the suppression in $P(k)$, meaning that high-mass haloes, which are still collapsing at that time, are less abundant with respect to the Λ CDM cosmology. This concept is explored further using the HMF fitting function of Tinker et al. (2008) in Appendix A.

M17 showed that massive neutrinos suppress the HMF with the largest effect at the high-mass end. Halo masses are suppressed by $\approx 10\%$ and $\approx 50\%$ for the lowest and largest sum of neutrino masses, respectively. Interestingly, S20 found that cosmologies which include running of the spectral index can impact the HMF in a very similar way to the DDE cosmologies, suppressing/amplifying the HMF at low/high masses for negative running cosmologies and vice versa for positive running cosmologies.

The effects of DDE on the HMF are very different to the effects of baryons on the HMF over the masses sampled here. M17 showed that baryonic feedback tends to suppress the HMF more strongly towards the high-mass end. However, at very high masses the

gravitational potential is strong enough to counteract the feedback, thus reducing its effect on the HMF. As well as this mass dependence, the amplitude of the baryonic impact is much stronger than that of the DDE cosmologies when they are constrained to reproduce the primary CMB (particularly the angular scale of the acoustic peaks).

3.3.2 Halo number counts

Next I examine the halo space density at a given redshift computed by integrating the HMF above a given mass. The halo space density simply represents the number density of haloes above a given mass. This is similar to what is more typically measured observationally since many surveys have too small a volume to robustly measure the HMF, especially at high masses.

Fig. 3.5 shows the number counts for haloes with $M_{200,\text{crit}} \geq 10^{12}M_{\odot}$, $10^{13}M_{\odot}$ and $10^{14}M_{\odot}$ out to $z = 3$ for the collisionless simulations for the different cosmologies. As expected from the HMF in Fig. 3.3, the number counts decrease for the freezing dark energy model and increase for the thawing dark energy models with increasing redshift relative to the Λ CDM cosmology. The crossing of the ratios in Fig. 3.3 can also be seen in the ratios of number counts where haloes with $M_{200,\text{crit}} \geq 10^{13}M_{\odot}$ cross over at $z = 1$. Because of the steepness of the HMF, the cluster count signal is dominated by the lowest-mass haloes, those near the lower mass limits in each mass bin. The bottom panels show that the difference is strongest for the highest-mass haloes and at higher redshifts. I plot error bars to show the Poisson uncertainties from the number of haloes in each redshift bin for the Λ CDM cosmology only for clarity, but note that the uncertainties for the other cosmologies are approximately of the same level. The uncertainties increase with increasing redshift and increasing mass since there are fewer haloes in those bins.

As discussed in Section 2.2 (see Fig. 2.2), a tension exists between the constraints in the $\sigma_8 - \Omega_m$ parameter space from CMB data and various LSS statistics, including number counts. LSS generally prefers lower values of S_8 , which results in fewer collapsed structures, compared to the value obtained from CMB data. As all of the

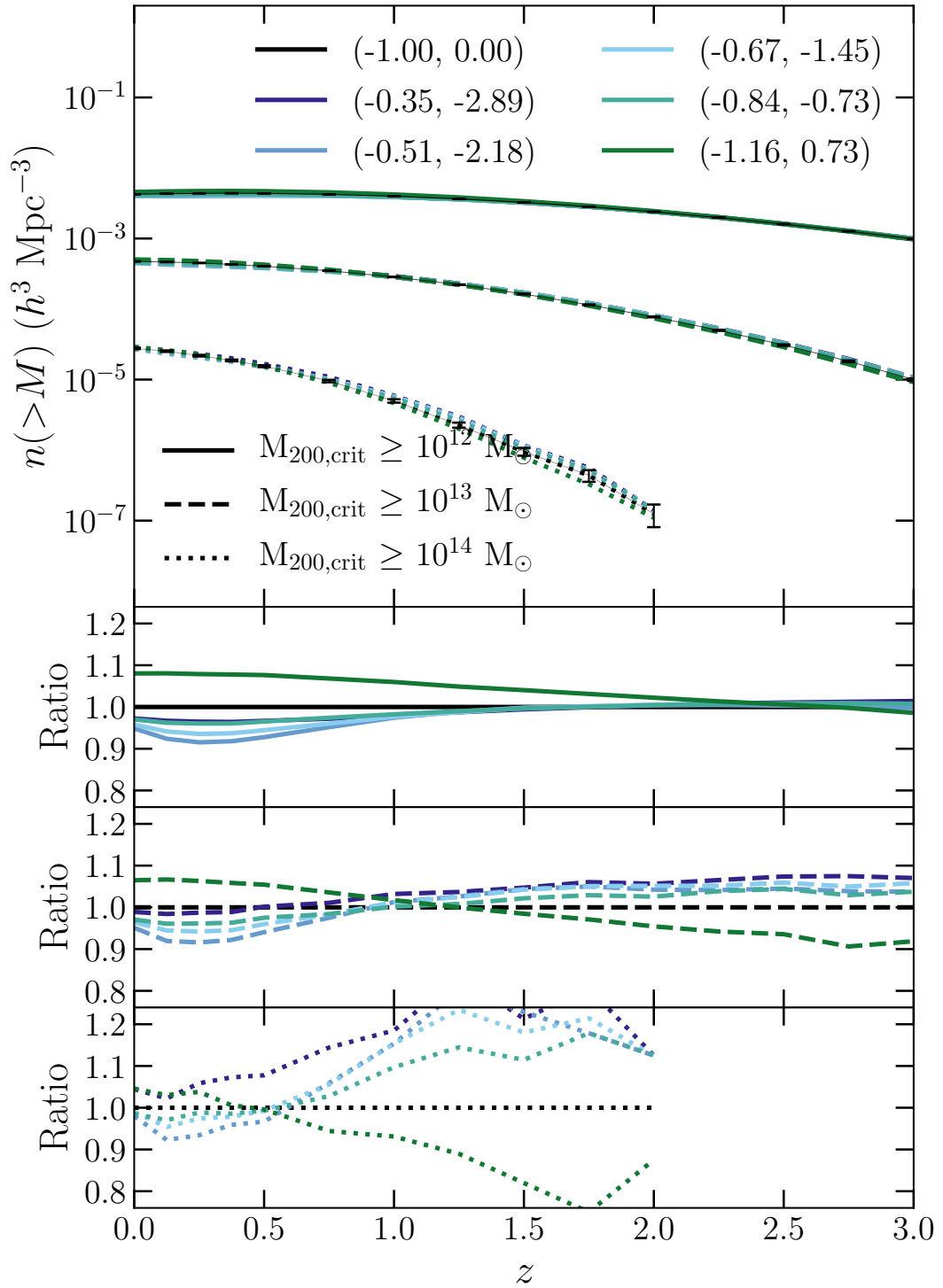


Figure 3.5: *Top*: The number density of dark matter haloes for different cosmologies and mass cuts. *Bottom*: The ratios of number density relative to the Λ CDM cosmology. Colours indicate different cosmologies where bracketed values refer to the values of (w_0, w_a) and the line styles show different lower mass limits of $10^{12}M_\odot$, $10^{13}M_\odot$ and $10^{14}M_\odot$. The error bars represent the Poisson uncertainties derived from the number of haloes in each redshift bin for the Λ CDM cosmology.

cosmologies are consistent with CMB data by construction, any cosmology that suppresses the growth of structure relative to the Λ CDM cosmology could help to alleviate this tension. Interestingly, I find that there is a non-monotonic behaviour in the variation in S_8 of the cosmologies and the impact on number counts relative to Λ CDM. For example, the freezing cosmology suppresses the abundance of the most massive clusters (Fig. 3.4 displays this most clearly) at a level that is comparable with that of the most extreme thawing models and yet the freezing model has a lower value of S_8 than the reference Λ CDM model while the most extreme thawing models have a larger value. The mapping between S_8 and cluster abundance is therefore more complex for (CMB-constrained) DDE models than for Λ CDM. Weak lensing, on the other hand, should provide a more direct constraint on S_8 than cluster abundances, as it measures the (projected) matter power spectrum. Thus, in principle, the combination of cluster abundances and cosmic shear should be helpful in constraining the parameters of DDE.

3.4 Collapse of structure

3.4.1 Mass accretion

I now examine the mass accretion history (MAH) of dark matter haloes. This is motivated by the fact that the DDE cosmologies affect the growth of structure (Pfeifer et al., 2020), suggesting that haloes experience different MAHs in these cosmologies in order to arrive at different masses today (see Fig. 3.4). To calculate the MAH of a halo from the simulations, I match haloes across simulation snapshots for the same cosmology as described in Section 3.2.2. I take the 50 most bound particles of a halo at the final snapshot and find them in the previous simulation snapshot (i.e. at an earlier time) using their unique particles IDs. The halo in the previous snapshot that contains the majority of those 50 particles is taken to be that halo's main progenitor. By applying this method to all snapshots, I can compute the MAH for all haloes. In Fig. 3.6 I show the mass for haloes as a function of a , normalised by their mass at $a = 1$ for each cosmology. Each panel shows the median MAH of haloes in bins of 0.5 dex in

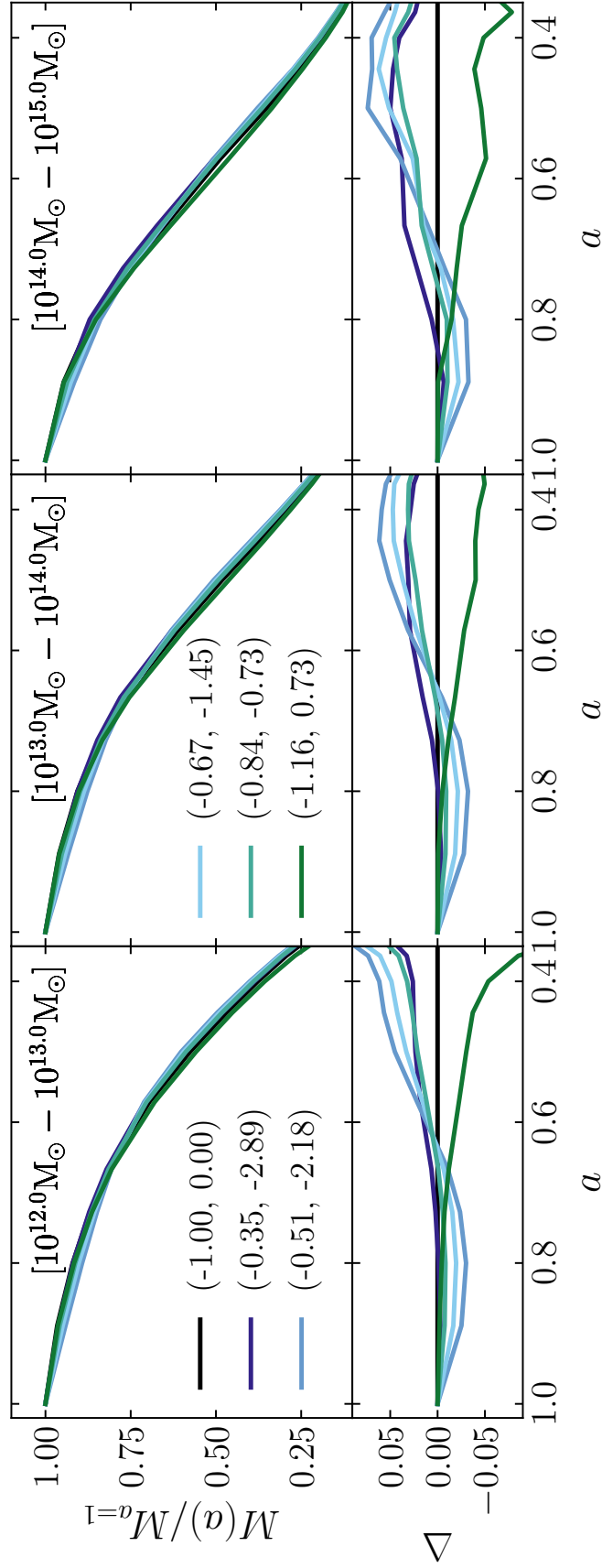


Figure 3.6: The mass of haloes from DDE cosmologies as a function of scale factor, normalised by the mass at present day. The solid lines in each panel show the median MAH of haloes in bins of $M_{200,\text{mean}}$ with width of 1 dex, where the mass in each bin refers to their mass at present day. The bottom panels show the fractional difference of the MAHs with respect to the Λ CDM cosmology. Colours indicate different cosmologies where bracketed values refer to the values of (w_0, w_a) .

$M_{200,\text{mean}}$, where the bins refer to the mass at present day, for the collisionless simulations. I also show the fractional difference of the MAHs with respect to the ΛCDM MAH at the bottom of each panel. The MAHs for lower-mass haloes have a steep rise in mass at low a (i.e., at early times) and a much flatter mass growth closer to today, while the high-mass haloes are still growing rapidly today. This is what is expected from hierarchical structure formation in which low-mass objects form most of their mass early in the Universe and high-mass objects are still forming today. There is also a clear change in the fractional difference between the different cosmologies, which can be split into two behaviours. The thawing models have lower (higher) mass at late (early) times, where the cross-over appears at $a \approx 0.6$. The freezing model shows a monotonic decrease with decrease in a . These behaviours appear to be independent of mass and suggest a global effect which affects haloes of all masses equally at any given time.

I also investigate the mass accretion rates (MAR) of dark matter haloes. I define the MAR as is done in Diemer and Kravtsov (2014),

$$\Gamma = \frac{\Delta \log(M)}{\Delta \log(a)} \quad (3.3)$$

which is effectively the gradient of the logarithmic quantities in Fig 3.6. I plot the MAR as a function of a for each cosmology in Fig. 3.7. The solid lines show the median MAR of dark matter haloes from the collisionless simulations in bins of $M_{200,\text{mean}}$, the same as Fig. 3.6. Accretion rates are high at early times and decrease towards present day, as expected from the argument of hierarchical structure formation given above. Equally, I also see that the absolute accretion rates are larger for higher-mass haloes. Similar to the MAH, I can split the trends in the fractional difference of the MAR into two different behaviours. The thawing models have a significantly lower MAR between $a \approx 0.5$ and $a \approx 0.8$ with a maximum suppression of $\approx 20\%$ and a significantly larger MAR at $a \gtrsim 0.8$ in excess of 20% with respect to ΛCDM . This behaviour is in part by construct because I select haloes of a similar mass. Therefore, if a halo experiences a suppression in mass accretion during its formation, it must also

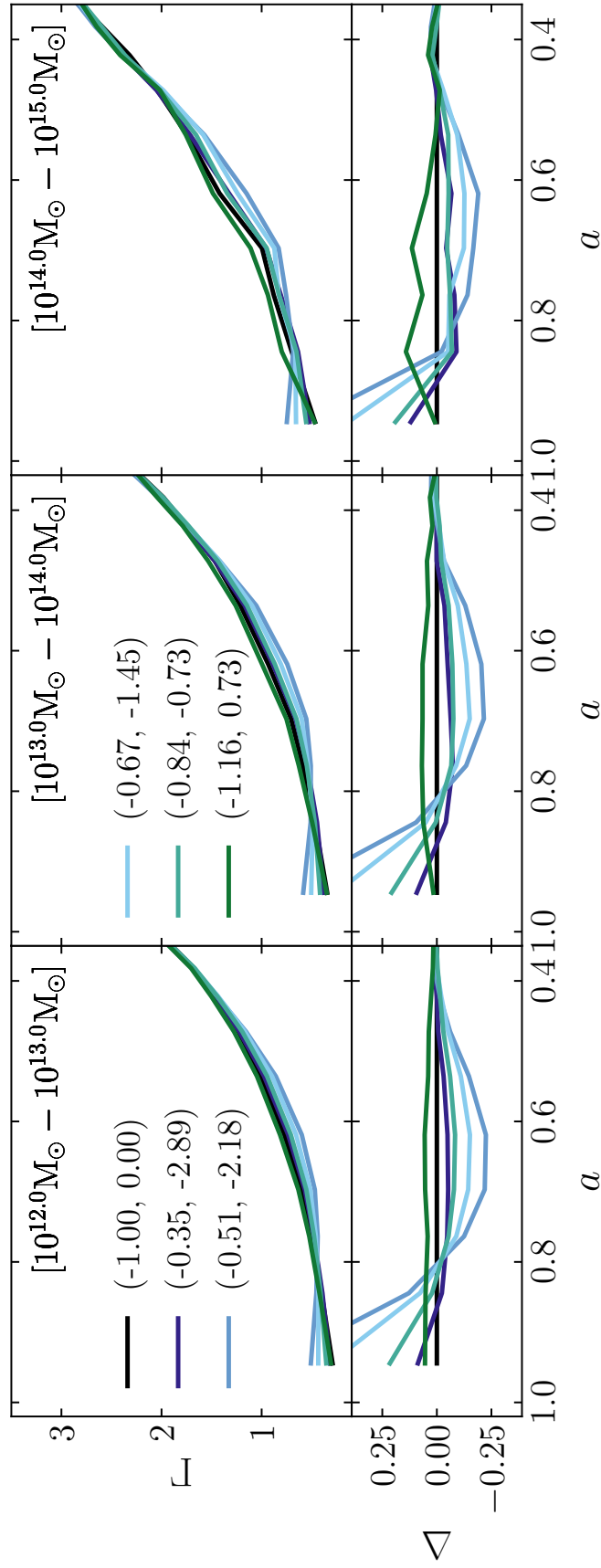


Figure 3.7: The mass accretion rates (defined in Equation 3.3) of haloes from DDE cosmologies as a function of scale factor. The solid lines in each panel show the median mass accretion rate of haloes in bins of $M_{200,\text{mean}}$ with width of 1 dex, where the mass in each bin refers to their mass at present day. The bottom panels show the fractional difference of the mass accretion rates with respect to the Λ CDM cosmology. Colours indicate different cosmologies where bracketed values refer to the values of (w_0, w_a) .

experience an increase in mass accretion to grow to the same mass as a fiducial halo. However, the freezing model does not fit into this explanation as it has an increased mass accretion relative to Λ CDM for the majority of the sampled a . This difference can be reconciled by considering the initial density perturbations from which these haloes grow. The above explanation is valid under the assumption that both haloes form from a region with the same initial over-density. However, regions of different initial over-density can collapse to form haloes of the same mass if their respective mass accretion histories are modified accordingly. Again, these behaviours are independent of mass.

3.5 Halo structure

Having investigated the overall abundance of haloes, I next examine the effect of DDE on the internal structure of haloes. The statistics I focus on are the radial velocity profiles, the spherically-averaged density profiles, the logarithmic slope of the density profiles and the halo concentration-mass relation.

3.5.1 Radial velocity profiles

In Fig. 3.8 I show the radial velocity profiles of dark matter haloes at different redshifts. I calculate the radial velocity profiles by stacking haloes within a given mass range and plot them as a function of radius from the halo centre of mass, where the particle radial distance is normalised by the $R_{200,\text{mean}}$ of their host halo. The radial velocity is the sum of the peculiar radial velocity, which is calculated from the velocity of the particles in the simulations, and a velocity induced due to the expansion of the Universe, $H(z)r$, which I add to the peculiar radial velocities. Since I plot the radial velocity profiles at different redshifts, I use the expansion rate at that redshift, calculated using Equation 1.8. I normalise the radial velocities by the mean $V_{200,\text{mean}}$ of the Λ CDM cosmology in each respective mass bin and redshift.

The mean radial velocities are approximately zero in the central regions of haloes since

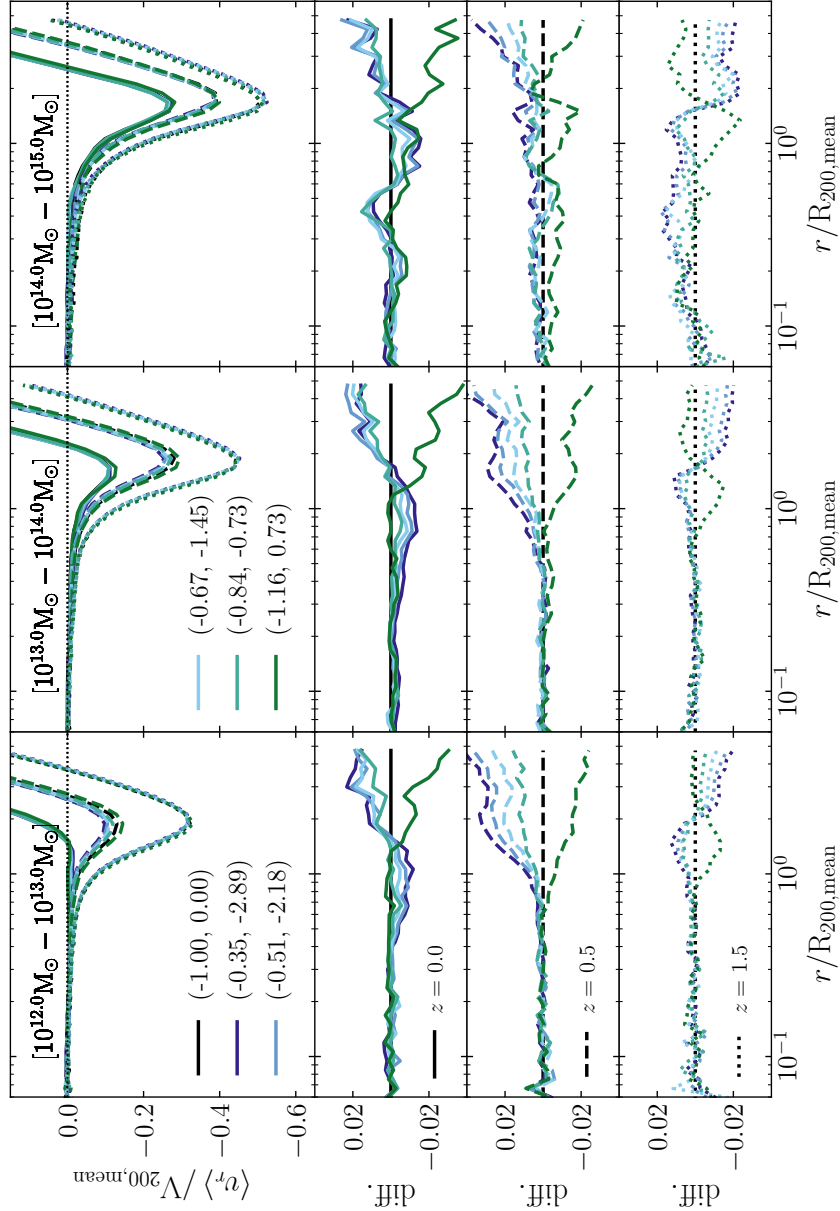


Figure 3.8: The stacked radial velocity profiles of dark matter haloes from DDE cosmologies in bins of $M_{200,\text{mean}}$ with width of 1 dex at $z = 0, 0.5, 1.5$, normalised by the mean $V_{200,\text{mean}}$ of the ΛCDM cosmology in each respective mass bin and redshift. Haloes have been matched with redshift and the quoted mass limits refer to the $M_{200,\text{mean}}$ at $z = 0$ for each cosmology. The bottom panels show the difference of the stacked radial velocity profiles with respect to the ΛCDM cosmology at different redshifts. Colours indicate different cosmologies where bracketed values refer to the values of (w_0, w_a) and linestyles represent different redshifts.

they are in equilibrium, neither collapsing nor expanding. At intermediate radii, $r \approx R_{200,\text{mean}}$, the velocities are negative corresponding to infalling matter. This infall is opposed by the Hubble flow which grows as a function of r . Thus, infalling matter is slowed until it reaches a point at which the peculiar velocity is matched by the velocity induced due to the Hubble flow. This point, at $v_r = 0$, is referred to the turnaround radius, R_{ta} , past which matter has a positive radial velocity and is moving away from the halo. More massive haloes have larger (more negative) infall velocities due to the fact that they are still actively accreting, even after normalising by $V_{200,\text{mean}}$ which accounts for the difference in the gravitational potential due the difference in mass.

I also show the radial velocity profiles at different redshifts indicated by different linestyles in Fig. 3.8. I use redshift matched haloes as described in Section 3.4.1 and therefore each mass bin follows the same population of haloes, where the masses refer to $M_{200,\text{mean}}$ at $z = 0$. This means that at any given redshift and mass bin I can draw a direct comparison between the radial velocity profiles and the MAH and MAR, shown in Fig. 3.6 and Fig. 3.7 respectively. I chose to investigate two particular redshifts other than $z = 0$; $z = 0.5$ ($a = 0.6$) is the redshift at which the MARs differ the most for the different cosmologies (other than $z = 0$), and $z = 1.5$ ($a = 0.4$) since at that redshift the MARs are very similar for the different cosmologies. At higher redshifts, the infall velocities become larger (more negative) in normalised units which can be attributed to the higher accretion rates at those redshifts (see Diemer and Kravtsov (2014)), and R_{ta} moves to larger radii.

The bottom panels of Fig 3.8 show the difference in the radial velocities relative to the Λ CDM cosmology for each redshift and mass bin. Here the internal velocity profile is not affected by cosmology. However, the outer region of the radial velocity profiles show systematic differences between the freezing and thawing DDE cosmologies. At $z = 0$, the thawing models have a larger (more negative) infall velocity at $r \approx R_{200,\text{mean}}$ and a lower (less negative) infall velocity beyond $r \approx 2R_{200,\text{mean}}$. The freezing model appears unaffected at $r \approx R_{200,\text{mean}}$ but has a larger (more negative) infall velocity $r \approx 2R_{200,\text{mean}}$. At $z = 0.5$, the thawing models now show a lower (less negative) infall velocity while the freezing model shows an equally higher (more negative) infall

velocity. Finally, at $z = 1.5$, the velocity profiles appear almost unaffected by cosmology. All of these trends show no dependence on mass. These behaviours match the trends seen in the mass accretion history in Fig. 3.7. Models with a larger MAR at a given redshift also show a larger (more negative) infall velocity at that redshift. The largest differences in the radial velocity appear at $z = 0.5$ and $r \approx 2R_{200,\text{mean}}$, and correspond to differences in velocity of $v \approx 1 \text{ km s}^{-1}$, $v \approx 8 \text{ km s}^{-1}$ and $v \approx 15 \text{ km s}^{-1}$ from lowest to highest mass bin.

I attempt to explain the features in the difference in radial velocity with redshift through the competition of two separate effects. At very large radii, matter is captured by the Hubble flow and the slope of the radial velocity profile is determined by $H(z)$. At $z = 0$, this is determined by the value of H_0 which is given in Table 2.2 for each cosmology. It can be seen that infalling matter at very large radii for cosmologies with larger values of H_0 experience lower (less negative) infall velocities. The second effect is due to the accretion rates. As seen in Fig. 3.7, the thawing DDE models have significantly larger accretion rates at $z = 0$ relative to the Λ CDM cosmology which would suggest larger (more negative) infall velocities which is indeed what is seen at $r \approx R_{200,\text{mean}}$. In fact, these two regimes seem to be separated by the minimum in the radial velocity profile. If I apply this to $z = 0.5$, first for thawing models, I expect a lower (less negative) infall velocity at $R_{200,\text{mean}}$ due to the lower MAR (see Fig. 3.7) and a lower infall velocity beyond R_{ta} due to the larger expansion rate at $z = 0.5$ (see Fig 2.3), and the opposite for the freezing model. This is indeed what the radial velocity profiles show.

3.5.2 Total mass density profile

I calculate the median radial total mass density profiles in 15 logarithmically spaced radial bins in the range $0.01 < r/R_{200,\text{crit}} \leq 1$ and for haloes in mass bins of 0.5 dex width in the range $M_{200,\text{crit}} = 10^{13}\text{-}10^{15}M_{\odot}$. The densities are scaled by r^2 to reduce the dynamic range.

Since the masses of haloes are affected by the DDE cosmologies, different populations

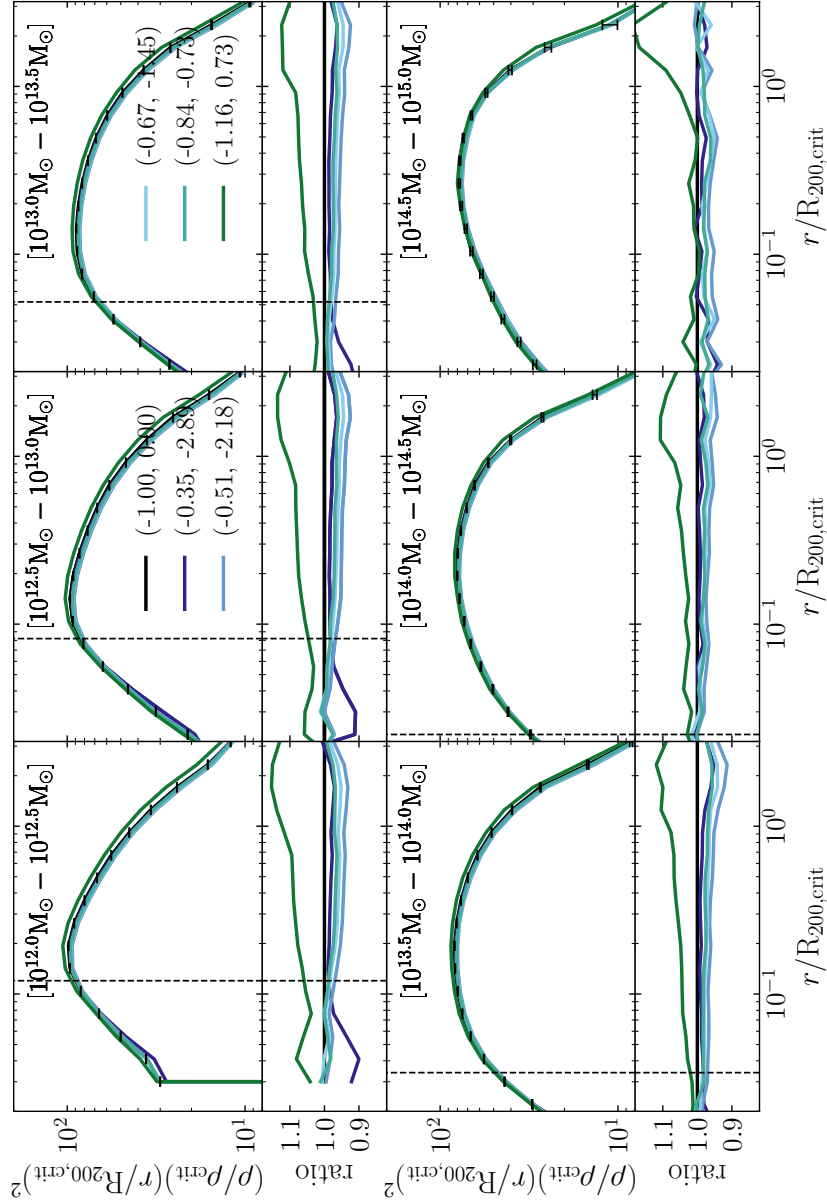


Figure 3.9: Median radial total mass density profiles of matched haloes for the different DDE cosmologies for collisionless simulations. Haloes have been matched to the Λ CDM cosmology. The panels show different mass bins with width 0.5 dex in $M_{200,\text{crit}}$ for the Λ CDM cosmology. Colours indicate different cosmologies where bracketed values refer to the values of (w_0, w_a) . The dashed vertical lines show the median convergence radius for haloes in that mass bin within which the density profiles should not be trusted. The error bars show the standard error on the median for the Λ CDM cosmology.

of haloes are selected in each mass bin for different cosmologies. This makes any comparison of the direct effect of different DDE cosmologies on the structure of haloes convoluted. In order to compare like-for-like haloes, I match haloes across simulations to the Λ CDM cosmology (see Section 3.3.1). Therefore, the mass bins correspond to $M_{200,\text{crit}}$ from the matched haloes in the dark matter-only Λ CDM simulations. Equally, the $R_{200,\text{crit}}$ values used to normalise the radial density profiles are those of the haloes that have been matched to, i.e. the $R_{200,\text{crit}}$ values from the dark matter-only reference Λ CDM simulations.

Fig. 3.9 shows the median radial total mass density profiles for the collisionless simulations for the different DDE cosmologies for different mass bins and the ratios relative to Λ CDM for each mass bin. The vertical dashed lines show the median convergence radius for haloes in that mass bin for the Λ CDM cosmology. The convergence radius was calculated using the method described in Power et al. (2003) (Equation 20) but with a convergence criterion of 0.177 as advocated by Ludlow et al. (2019). The effect of the freezing DDE cosmology is to increase the density of dark matter haloes whereas the thawing DDE cosmologies have the opposite effect, decreasing the density. The DDE cosmologies change the density by at most $\sim 10\%$ and the difference decreases in amplitude with increase in halo mass. There is also a radial dependence that shows an increase in density with increasing radius. I show the standard error on the median as error bars for the Λ CDM cosmology only, but note that the errors on the other cosmologies are approximately the same as for the Λ CDM case.

These general trends in the density profiles are consistent with the previously found results for the change in the mass of matched haloes. For example, haloes that show a higher density relative to their matched Λ CDM counterpart in Fig. 3.9 also show a relative increase in their $M_{200,\text{crit}}$ in Fig. 3.4. This is similar to what was found by M17 and S20. M17 shows that cosmologies with massive neutrinos lower the masses of dark matter haloes relative to their matched Λ CDM haloes and these cosmologies also show an almost radially independent suppression of the density profiles. In S20, cosmologies with running of the spectral index suppress (increase) mass growth for low-mass (high-mass) haloes and this was also reflected in their respective halo densities.

3.5.3 Slope of the density profiles

I explore the logarithmic slope of the density profiles, defined as $\gamma \equiv d\log\rho/d\log r$. Diemer and Kravtsov (2014) show that the primary mechanism behind changes in γ is the MAR. Since the DDE cosmologies affect the MAR of haloes of a given mass, I also expect to see changes to γ . I calculate the density profiles from all haloes within a mass bin for a given cosmology over 150 logarithmically spaced radial bins from 0.01 to $5 R_{200,\text{mean}}$. The radial distance of every particle is normalised by the $R_{200,\text{mean}}$ of its host halo and the final density profile is given by the median density in each radial bin for all haloes within a given mass bin, redshift and cosmology. The haloes have been redshift matched, as described in Section 3.7, which means that I follow the same population of haloes through redshift within a given mass bin in Fig 3.10, where the masses refer to $M_{200,\text{mean}}$ at $z = 0$. I follow the method in Diemer and Kravtsov (2014) and calculate the logarithmic slope of the median density profiles after applying a second-order Savitzky-Golay (Savitzky and Golay, 1964) smoothing algorithm to the logarithmic median density profiles which is designed to smooth out noise without introducing artifacts or artificially changing the values of the slope. By smoothing over 15 bins, the method fails for the 7 bins on the radial extremes of the slope. I do not attempt to correct for this as I am not concerned about the inner-most and outer-most slope, and instead simply cut those bins from the distribution.

I can define the splashback radius, R_{sb} , as the radius at which the density profiles are the steepest, or alternatively, at which γ is lowest. R_{sb} lies outside of $R_{200,\text{mean}}$ for all masses and redshift, and shows almost no redshift dependence. Generally, higher mass haloes have lower values of γ , however, the trend in the steepness of the density profiles at R_{sb} with redshift is different in each mass bin. At low masses, γ becomes more negative with increasing redshift, while the opposite is true for high-mass haloes. The lower panels in Fig 3.10 show the fractional difference of γ relative to the Λ CDM cosmology at each redshift. At $z = 0$, there appears to be no effect due to cosmology in any of the mass bins. The fractional differences at $z = 0.5$ and $z = 1.5$ show the same trend which appears to be due to a small radial shift in R_{sb} . The thawing models have smaller R_{sb} compared to the Λ CDM cosmology while that of the freezing model

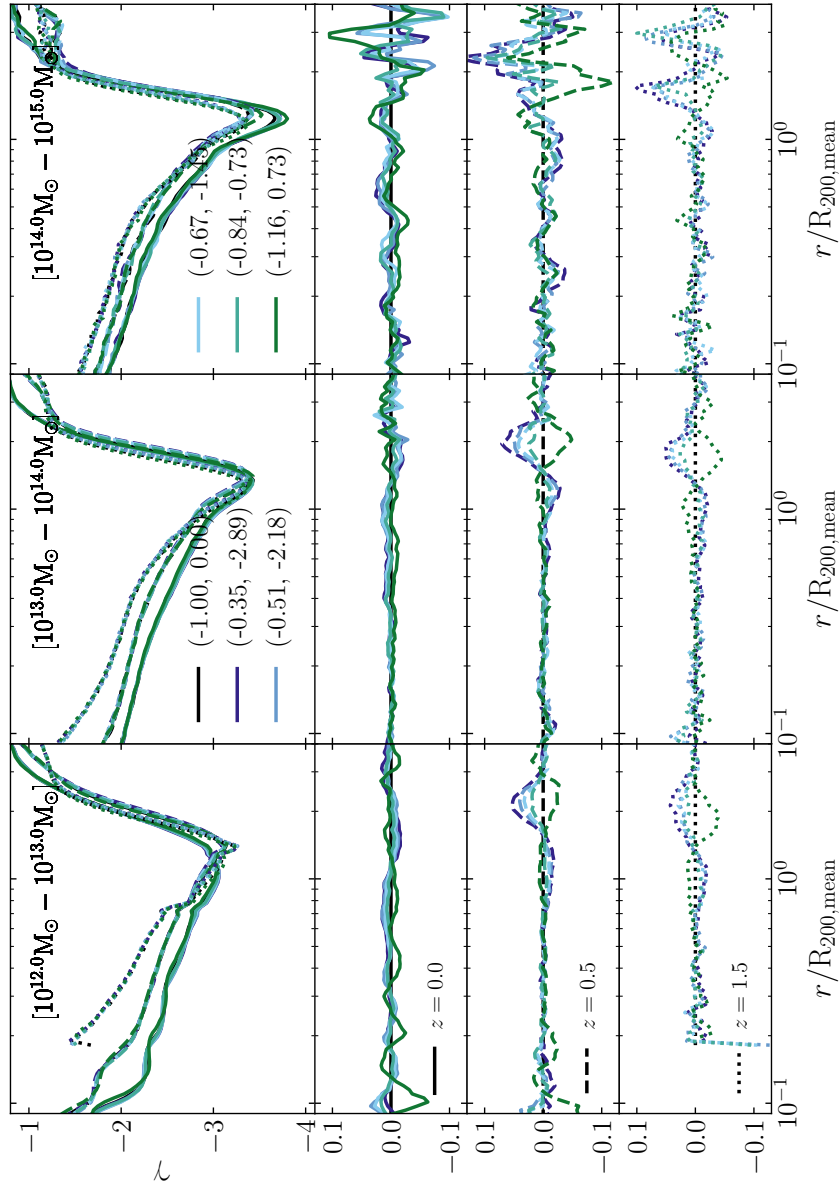


Figure 3.10: The logarithmic slope of the median density profiles of dark matter haloes from DDE cosmologies in bins of $M_{200,\text{mean}}$ with width of 1 dex at $z = 0, 0.5, 1.5$. Haloes have been matched with redshift and the quoted mass limits refer to the $M_{200,\text{mean}}$ at $z = 0$ for each cosmology. The bottom panels show the fractional difference of the profiles with respect to the Λ CDM cosmology at different redshifts. Colours indicate different cosmologies where bracketed values refer to the values of (w_0, w_a) and linestyles represent different redshifts.

is slightly larger. None of the trends in the fractional difference at any redshift shows a dependence on mass. In fact, the largest mass bin is too noisy to be able to see any trend.

The fact that the logarithmic slope of the density profiles do not appear to be susceptible to the changes in cosmology suggests that the internal structure of haloes and R_{sb} scales well with R_{mean} . Why this is the case is left for future work.

3.5.4 Concentration–mass relation

The internal structures of haloes are themselves tracers of the formation history of haloes. Since the formation history depends on the evolution of the background density, the internal structure is also sensitive to the cosmology. CDM models predict that low-mass haloes collapse earlier while high-mass haloes, such as clusters, are still collapsing today. As gravitational collapse can only occur when the local density exceeds the background density, lower-mass haloes are expected to have a more concentrated density profile, which has been shown to be true in a number of high resolution simulations (e.g. Bullock et al. 2001; Eke et al. 2001).

Simulation results have shown that dark matter density profiles can be approximately described by the NFW profile (Navarro et al., 1997)

$$\rho(r) = \frac{\rho_s}{\frac{r}{r_s} \left[1 + \frac{r}{r_s} \right]^2}, \quad (3.4)$$

which only has a scale density, ρ_s , and a scale radius, r_s , as free parameters. With this, one can define the concentration as $c_{200,\text{crit}} \equiv R_{200,\text{crit}}/r_s$.

To calculate the scale radius for the halo sample, I first remove all unrelaxed haloes as unrelaxed haloes are not in virial equilibrium and have been shown to be poorly described by the NFW profile (e.g. Macciò et al. 2007; Romano-Díaz et al. 2007). This is done by ensuring that all haloes have their centre of mass offset by no more than $0.07 R_{200,\text{crit}}$ from the centre of potential (Neto et al., 2007), which has been

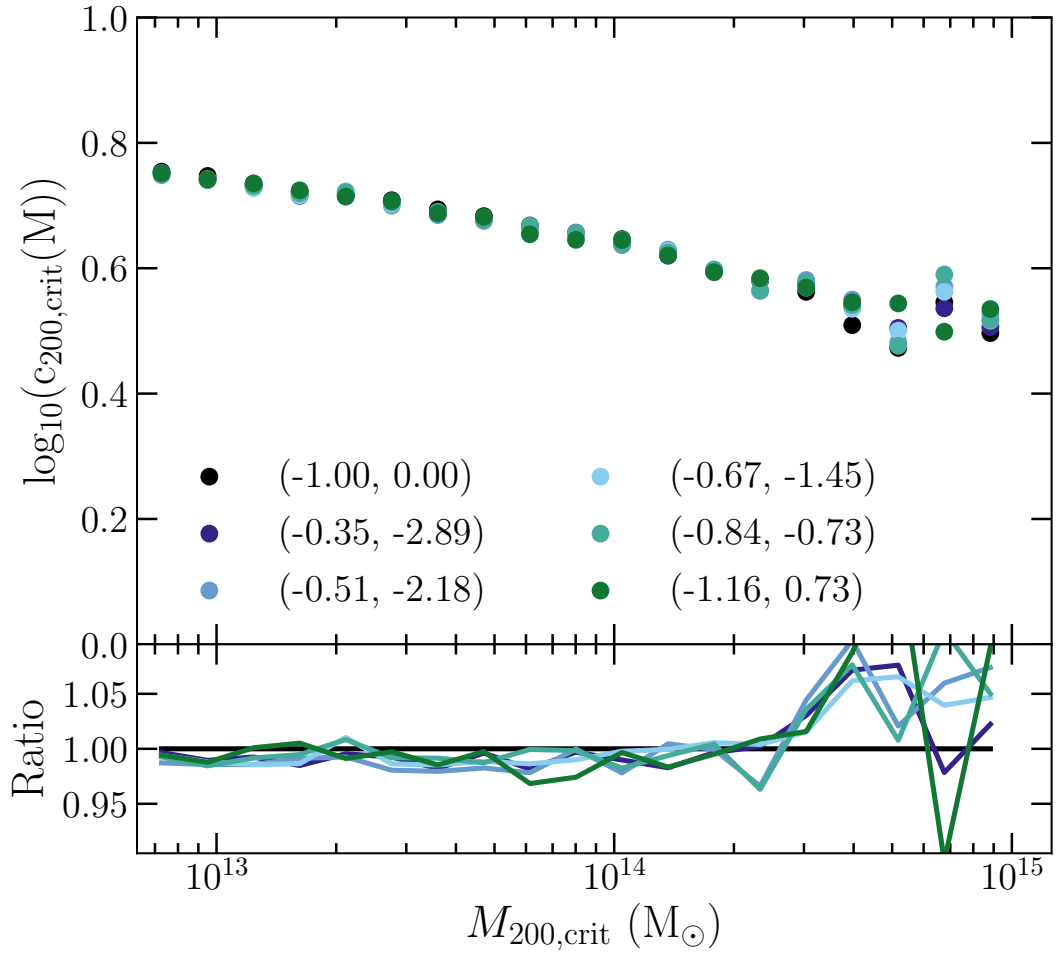


Figure 3.11: *Top:* The concentration of dark matter haloes for the different cosmologies. Points represent the median concentration in 20 equally spaced bins between $10^{13} \leq M_{200,\text{crit}} < 10^{15.5}$ in bins of $M_{200,\text{crit}}$. *Bottom:* The ratios of concentration of the median points with respect to the Λ CDM cosmology. Colours indicate different cosmologies where bracketed values refer to the values of (w_0, w_a) .

shown to remove the vast majority of unrelaxed haloes (Duffy et al., 2008). I select haloes with more than 800 particles and stack them until they have a total of 5000 particles. Lastly, I fit an NFW profile over the radial range $0.1 \leq r/R_{200,\text{crit}} \leq 1.0$ and remove any halo for which $r_s < \text{convergence radius}$ (described in Section 3.5.2) to ensure the halo density profiles are converged. I fit to the quantity ρr^2 to give equal weighting to each radial bin (Neto et al., 2007).

In Fig. 3.11 I show the logarithm of the concentration for unmatched dark matter haloes for each cosmology (top). As I have not matched haloes, I use the $M_{200,\text{crit}}$ and $R_{200,\text{crit}}$ from each simulation. The points represent the median value in each mass bin for 20 equally spaced bins between $10^{13} \leq M_{200,\text{crit}} < 10^{15.5}$. The ratios were taken with respect to the ΛCDM cosmology of the binned median values (bottom). There is no strong trend in the ratios of the concentrations for the different cosmologies. Small differences appear at the high-mass end which is also where the scatter in the concentrations becomes significant.

M17 showed that massive neutrinos systematically lower the concentration of dark matter haloes at the $\approx 5\text{-}10\%$ level between the lowest and highest neutrino mass, while S20 showed that cosmologies with running of the spectral index increase the concentration towards higher masses for all considered cosmologies. M17 also showed that the effect of baryonic feedback is of the order of $\approx 20\%$ which dominates any effect on the concentrations due to cosmology.

3.6 Summary

I constructed a new suite of cosmological hydrodynamical simulations using a modified version of the *BAHAMAS* code to investigate the effects of spatially flat DDE cosmologies on LSS. Six cosmologies were chosen based on the constrained $w_0 - w_a$ geometric degeneracy from the *Planck* TT+lowTEB data set. I included A_{lens} as a free parameter in the analysis to account for the enhanced smoothing of the CMB temperature power spectrum. DDE changes the expansion history of the Universe (see Fig. 2.3)

and therefore affects the growth of structure. However, I chose the other cosmological parameters so that the *integrated* expansion history (i.e., the distance to the surface of last scattering) is the same and consistent with the *Planck* primary CMB data. While this approach generates more ‘realistic’ cosmologies, it makes disentangling the effects of DDE from those caused by changes in the other cosmological parameters more challenging. Therefore, I refer to the DDE cosmologies as a whole, rather than the DDE itself, and all effects are with respect to the Λ CDM cosmology.

While the analysis is restricted to a single extension to Λ CDM, as I want to see the effects of DDE, I do compare the results to the possible cosmological extensions of a running of the spectral index as well as changes to the summed neutrino mass. It would be interesting to let DDE, running, and massive neutrinos vary simultaneously (e.g., see Di Valentino et al. 2016, 2020b) to examine the degeneracies between their effects, but I leave this for future studies. To examine the impact of the DDE cosmologies on the LSS, I have examined a variety of statistics, namely: the matter power spectrum, the 2-point auto-correlation function of dark matter haloes, the halo mass function, and halo number counts. I also examined the mass accretion history and MAR of dark matter haloes. Finally, I have looked at the radial velocity profiles, radial density profiles and their logarithmic slope, and the concentration–mass relation to investigate the impact of DDE on internal properties of haloes.

The main findings can be summarised as follows:

- The clustering of matter is strongly affected in the DDE cosmologies. Both the matter power spectrum (Fig. 3.1) and the 2-point auto-correlation function of haloes (Fig. 3.2) can show up to a $\sim 10\%$ change at $z = 0$, where the thawing (freezing) DDE cosmologies enhance (suppress) the clustering with respect to the reference Λ CDM cosmology. The effect on $P(k)$ shows only a weak scale dependence, while the amplitude change agrees well with the expectations based on changes in the linear growth factor for the different cosmologies. The redshift dependence of these effects is relatively mild.
- The effect on the abundance of low-mass haloes in the different DDE cosmolo-

gies is of the same order of magnitude as the clustering and has a strong mass dependence (Fig. 3.3). The largest effects are seen at the high-mass end and at higher redshifts, $z = 1$ and $z = 2$. The abundances of the lowest-mass haloes in the simulations at any given redshift are modified by $\approx 5\text{-}10\%$ while the highest-mass haloes can have their abundances modified by up to $\approx 20\%$. The thawing (freezing) DDE cosmologies decrease (increase) the abundance of low-mass haloes with respect to ΛCDM , whereas for high-mass haloes ($M_{200,\text{crit}} \gtrsim 10^{14} M_{\odot}$) this trend is reversed. The effect at the low-mass end can be attributed to the differences in Ω_m between the cosmologies, while the changes at the high-mass end are due to the change in growth of structure (i.e., $P(k)$).

- The change in the abundances and, more importantly, the fractional mass between different cosmologies can be clearly seen in the mass accretion history of haloes. These differences are amplified in the MARs where higher accretion rates occur for the thawing cosmologies at $z = 0$ and lower accretion rates around $z = 0.5$, relative to ΛCDM . The freezing cosmology behaves rather docile in comparison, showing a mild enhancement in the accretion rates until $z \approx 1.5$. The MAH and MAR show systematic differences between thawing and freezing cosmologies relative to ΛCDM , although with no mass dependence.
- In terms of the internal structure of haloes, the DDE cosmologies generally have less of an impact. The radial velocity profiles display systematically different trends for the thawing and freezing cosmologies but the magnitude of these are very small, of the order of 10 km s^{-1} . The density profiles show shifts in amplitude consistent with the change in halo mass mentioned above (Fig. 3.9), while the shapes of the density profiles are only weakly affected. The logarithmic slope of the density profiles show almost no changes between cosmologies, most likely because the changes in the MAR is simply too small.
- The effects on the chosen statistics have been compared to the effect of massive neutrinos with a varying sum of neutrino masses previously investigated in BAHAMAS (Mummery et al., 2017). It is clear that massive neutrinos can behave similarly to the cosmologies including DDE presented here. However,

massive neutrinos can only suppress the clustering of matter and haloes and the abundances of haloes, whereas the freezing and thawing cosmologies can either suppress or enhance these, respectively. Their scale and redshift dependence on $P(k)$, as well as their mass and redshift dependence on the abundance of haloes, are very similar which makes the effect of massive neutrinos and thawing cosmologies difficult to distinguish (see also Upadhye 2019).

- I have also compared these statistics to the effect of a running of the scalar spectral index found by Stafford et al. (2020). The comparison to running of the spectral index shows striking similarities in both the shape and magnitude of observed trends for all the considered statistics. The scale and redshift dependencies in $P(k)$ are very similar for the scales I sample although there appears to be some deviations in behaviour at the smallest scales, largest k . The effect on the abundance of dark matter haloes is even more similar, with both cosmological extensions showing remarkably similar trends across mass and redshift.

I can put the work in the context of the LSS tension that exists between ‘early-Universe’ CMB data and ‘late-Universe’ LSS data sets, where the latter prefer lower values of S_8 than the former, which is effectively equivalent to saying that the observed low-redshift Universe is smoother than it ought to be assuming the Λ CDM model with CMB constraints on its parameters. It is clear from Table 2.2 that the cosmologies do not significantly lower the S_8 parameter relative to Λ CDM and most DDE models I consider actually increase its value (the thawing models). This simple comparison, though, relies on the assumption that changes to the value of S_8 directly translate into changes in the formation of structure. However, I have shown that for (CMB-constrained) DDE models, the mapping between massive cluster abundances in particular and S_8 is more complex (non-monotonic) than for Λ CDM, with the freezing model (with lower S_8) yielding a similar suppression in cluster abundances to some of the extreme thawing models (with higher S_8). Cosmic shear (weak lensing), on the other hand, might be expected to more directly constrain S_8 , given that it measures the projected matter power spectrum. In principle, therefore, the combination of different LSS tests should be helpful in constraining the nature of DDE. As for the current claimed tension between

the CMB and measures of LSS, the variations I see in the DDE cosmologies, while certainly not insignificant, do not appear to be large enough on their own to reconcile the tension (e.g., the abundance of clusters is suppressed by $\approx 5\%$ for some of the models, whereas a suppression of $\approx 50\%$ or larger is claimed to be required, depending on how the mass scale of clusters is calibrated).

In this chapter I have presented a wide variety of statistics and shown the effect that the DE cosmologies have on them, which are summarised above. In Chapter 4 I investigate the interplay between the DE cosmologies and baryon physics with the aim of quantifying how dependent these are on each other.

Chapter 4

Impact of baryons and its effect on cosmology

In this chapter, I investigate the effects of including baryons on some of the statistics I have shown so far and show to what degree these can be separated from the effects of changing the cosmology. I use the term “separability” to refer to the degree by which cosmological and baryonic effects are independent of each other, or in other words, how sensitive one is to the other. The work presented here uses large cosmological hydrodynamical simulations to study the combined effects of DDE and baryons on LSS for the first time.

Many studies have used collisionless simulations to study the effects of DE that differ from the cosmological constant on the dark matter distributions. The first studies explored cosmologies with $w \neq -1$ but still constant with time (Ma et al., 1999; Bode et al., 2001; Łokas et al., 2004) and soon after, a variable equation of state parameter was introduced (Klypin et al., 2003; Linder and Jenkins, 2003b). For the interested reader, Baldi (2012) reviews different theoretical DE models along with relevant studies that utilise cosmological simulations. More recently, DE has been studied using collisionless simulations in the context of the halo mass function (Francis et al., 2009; Bhattacharya et al., 2011; Courtin et al., 2011; Biswas et al., 2019), non-linear power spectrum (Francis et al., 2009; Casarini et al., 2009; Alimi et al., 2010; Heitmann et al.,

2010), and has been employed in both semi-analytic (Takahashi et al., 2012; Mead et al., 2015; Cataneo et al., 2019) and emulation (Kwan et al., 2013; Heitmann et al., 2014; Knabenhans et al., 2019; Harnois-Deraps et al., 2019) frameworks. Hydrodynamical simulations have also been used, although to much less extent, specifically to investigate the impact of DE on galaxy evolution (Penzo et al., 2014) and cosmic reionization (Maio et al., 2006).

It has been shown that the inclusion of baryonic physics in cosmological simulations can have a significant effect on the overall matter distribution. This has been shown with respect to the matter power spectrum (e.g. van Daalen et al. 2011; Schneider et al. 2019; van Daalen et al. 2020), the halo mass function (e.g. Sawala et al. 2013; Cusworth et al. 2014; Velliscig et al. 2014), clustering (van Daalen et al., 2014), density profiles (e.g. Duffy et al. 2010; Schaller et al. 2015) and the binding energy of haloes (Davies et al., 2019), which are all significantly impacted by baryons and their respective feedback mechanisms. Of course, changes in cosmology also have a large effect on some of these statistics. This raises the question of whether the effects of cosmology and baryons influence each other or, instead, can be treated independently, as often implicitly assumed in halo model-based approaches (e.g., Mead et al. 2016).

Such considerations are also important when constructing hydrodynamical simulations, since it is often desirable that they reproduce a particular set of observables. If those observables are sensitive to cosmological variations, then this would suggest that the simulations would need to be re-calibrated for each choice of cosmology. The BAHAMAS suite of simulations are a first attempt at calibrating the feedback processes to study their impact on LSS for large-volume cosmological hydrodynamical simulations. It is therefore vital for the calibration statistics to be mostly unaffected by a change in cosmology, or to re-calibrate after every change. The calibration statistics for BAHAMAS are the observed stellar and hot gas mass of haloes, which were specifically chosen because they are expected to be relatively insensitive to changes in cosmology (as confirmed in McCarthy et al. 2018, S20, and later here) and because these quantities are directly related to impact of baryons on the matter power spectrum (van Daalen et al., 2020; Debackere et al., 2020). In the present study, I have used the

same feedback parameters as adopted in McCarthy et al. (2017) and I have verified that the cosmologies considered in this work all reproduce the calibration statistics as well as found in that study.

I have also confirmed that the relative impact of feedback (at fixed cosmology) on various metrics, such as the matter power spectrum and the halo mass function, are the same (to within a couple of percent) as reported previously in M17 and S20 (see also Fig. 4.3 below). Therefore, rather than re-examine the effects of baryons, I limit the exploration here to the question of whether the impact of baryons is separable from the change in cosmology. To do so, I follow the approach taken in M17 and S20. Specifically, if the effects are separable, then multiplying the impact of baryons in the reference Λ CDM run (relative to the collisionless version of this simulation) by the impact of changing the nature of DE relative to Λ CDM for the collisionless case, should reproduce the combined impact of baryons and a change in cosmology of a DDE run with hydrodynamics compared to the collisionless Λ CDM run.

To express the above mathematically, I test the *ansatz* that

$$\psi_{\text{H}}^{\text{cosmo}} = \psi_{\text{DMO}}^{\Lambda\text{CDM}} \left(\frac{\psi_{\text{DMO}}^{\text{cosmo}}}{\psi_{\text{DMO}}^{\Lambda\text{CDM}}} \right) \left(\frac{\psi_{\text{H}}^{\Lambda\text{CDM}}}{\psi_{\text{DMO}}^{\Lambda\text{CDM}}} \right). \quad (4.1)$$

where ψ is the chosen statistic (such as the matter power spectrum or the HMF), the subscripts denote whether it is from the collisionless or hydrodynamical cases, and the superscripts denote the cosmology where ‘cosmo’ refers to either a DDE or Λ CDM cosmology. The first and second bracketed terms are therefore the effect of cosmology and baryons with respect to a collisionless (dark matter-only) Λ CDM cosmology simulation, respectively.

To test the separability, I have run all of the simulations including hydrodynamics, using the calibrated feedback model from the original BAHAMAS runs (McCarthy et al., 2017). I test the degree of separability by applying equation 4.1 to three statistics: the matter power spectrum, the HMF and the density profiles. I do not show the absolute effect of including hydrodynamics on these statistics as this has already been covered

thoroughly in M18 for the subgrid calibration strategy used in the BAHAMAS suite of simulations. Since I use the same calibration as in M18 and, as I show below, the baryonic effects and those of the DDE cosmologies are independent of each other, the baryonic effects shown in M18 are identical to those in the work presented here.

4.1 Matter clustering

4.1.1 Matter power spectrum

I first examine the total matter power spectrum, which was described in Section 3.2. Fig. 4.1 shows the total matter power spectrum from the hydrodynamical simulations (lines) and from the collisionless simulations with baryonic effects applied following the prescription in equation 4.1 (crosses). To see how well these agree, I show the ratio for each cosmology and at three different redshifts, $z = 0, 1,$ and 2 . As can be seen, the effects of cosmology and baryons (feedback) are separable to very high precision (typically $< 0.1\%$ for $k < 10 h \text{ Mpc}^{-1}$) for the majority of the k -scales and across all redshifts shown.

4.2 Halo abundance

4.2.1 Halo mass function

Next I examine the separability of baryonic and cosmological effects on the HMF, which was described in Section 3.3.1. Fig. 4.2 shows the HMF for the hydrodynamical simulation (lines) and the collisionless simulations including baryonic effects following the prescription in equation 4.1 (crosses). As with the matter power spectrum, I show the ratio of these for each cosmology and for $z = 0, 1, 2$. They typically agree to better than a few percent accuracy for the majority of the mass range sampled at each redshift. The scatter increases somewhat at the high-mass end at each redshift due to

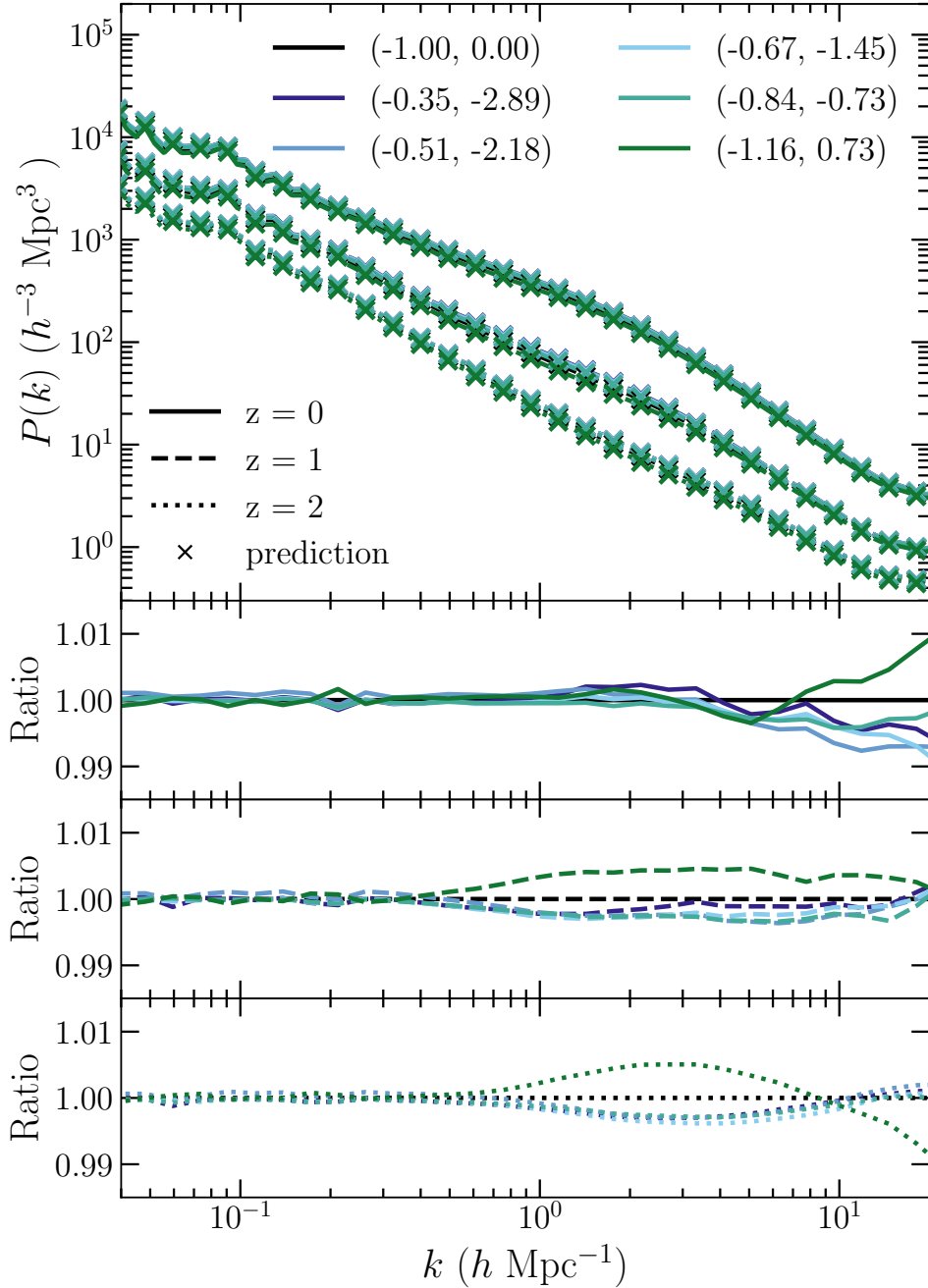


Figure 4.1: *Top*: the total matter power spectra for the different cosmologies from hydrodynamical simulations (lines) and the collisionless simulations with added baryonic effects (crosses) as described in equation 4.1. Line styles indicate different redshifts. *Bottom*: The ratios at different redshifts of the matter power spectrum from hydrodynamical simulations and the collisionless simulation with added baryonic effects for the same cosmology. Colours indicate different cosmologies where bracketed values refer to the values of (w_0, w_a) and linestyles indicate redshifts.

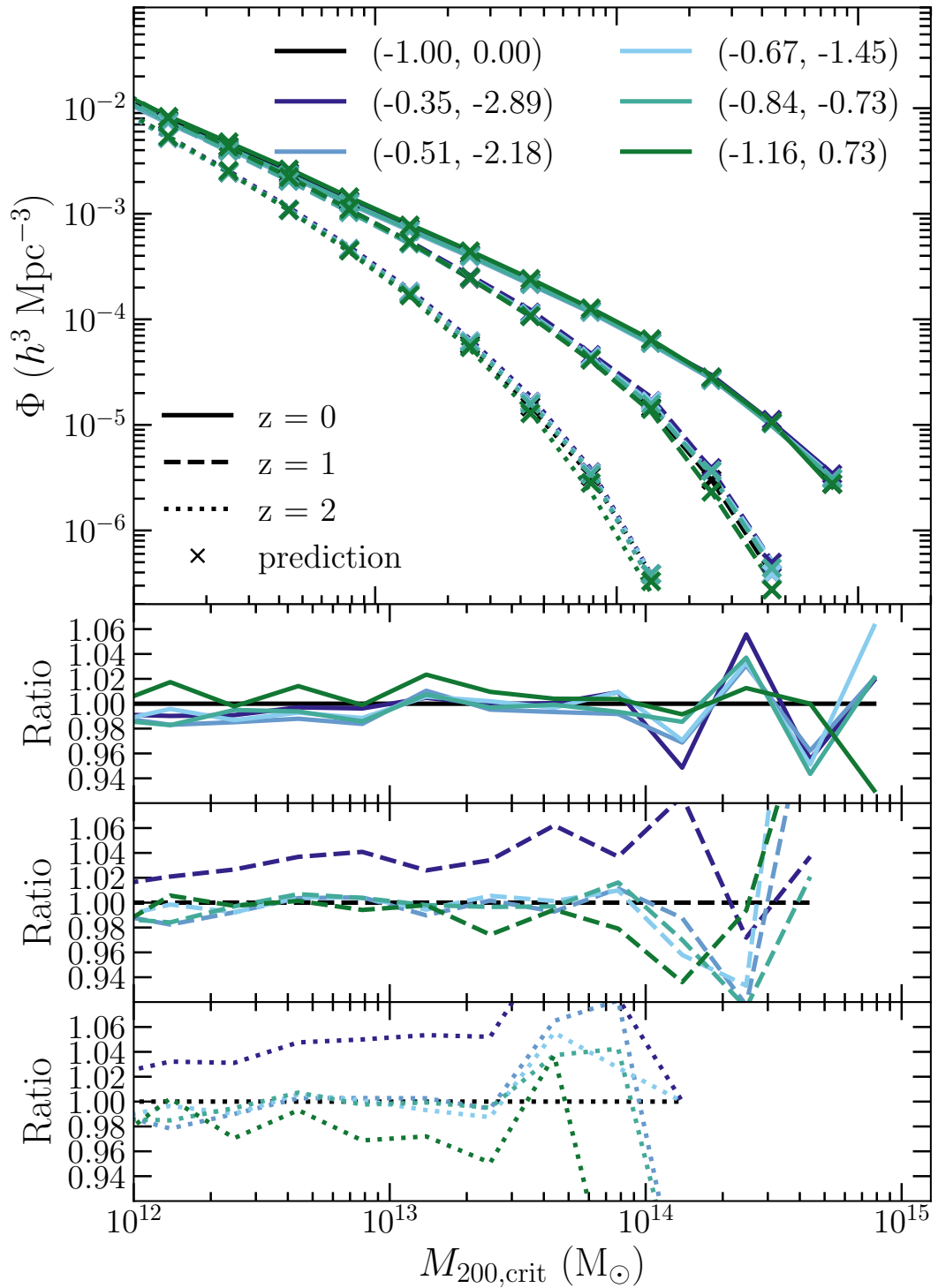


Figure 4.2: *Top*: the HMF for the hydrodynamical simulations (lines) and the collisionless simulations with added baryonic effects (crosses) as described in Equation 4.1. Line styles indicate different redshifts. *Bottom*: The ratios at different redshifts of the HMF from hydrodynamical simulations and the collisionless simulation with added baryonic effects for the same cosmology. Colours indicate different cosmologies where bracketed values refer to the values of (w_0, w_a) and linestyles indicate redshifts.

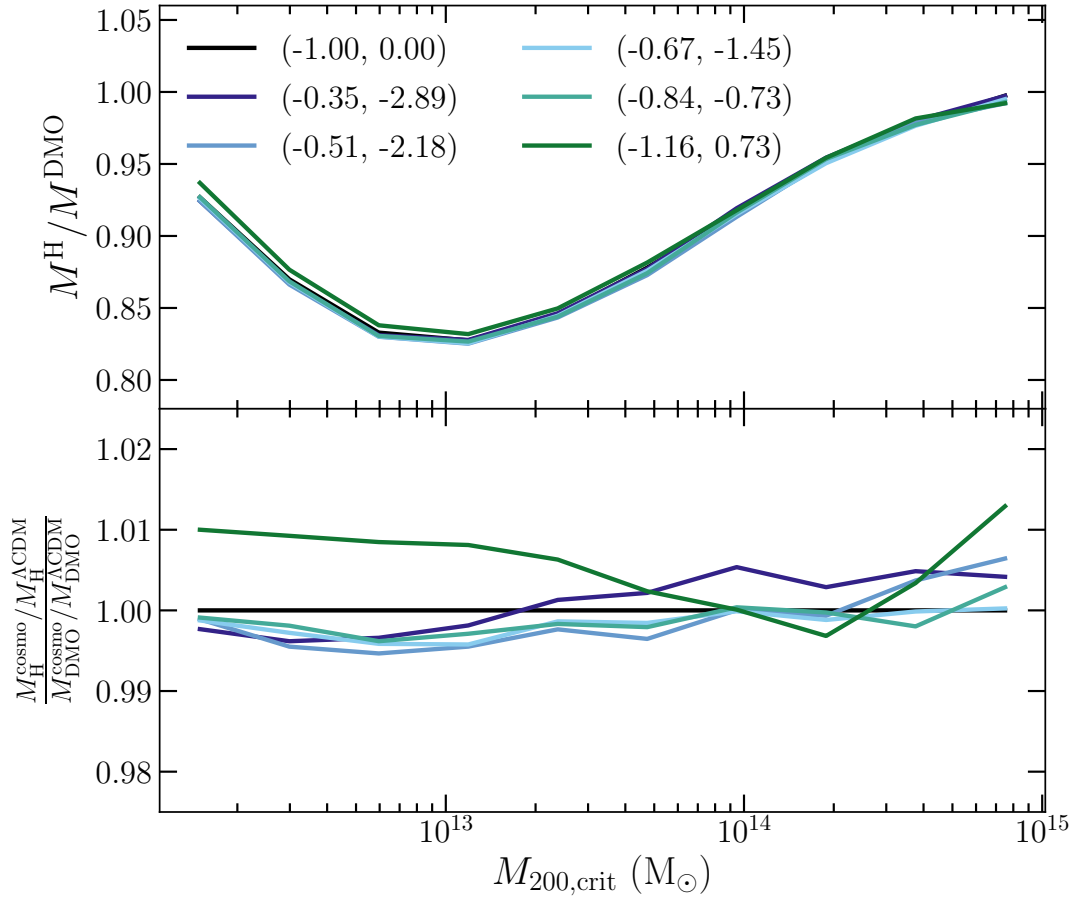


Figure 4.3: *Top:* The fractional change in halo mass, $M_{200,\text{crit}}$, of haloes from the hydrodynamical simulations relative to their matched dark matter counterparts at $z = 0$. *Bottom:* The ratio of the fractional mass change from hydrodynamical simulations and the collisionless simulations with added baryonic effects (see Equation 4.1). Colours indicate different cosmologies where bracketed values refer to the values of (w_0, w_a) .

the relative rarity of such systems.

I also investigate the separability of cosmological and baryonic effects on the masses of haloes, as I have shown that the halo mass is affected by DDE (Fig. 3.4) and previous studies have shown the impact of baryonic physics on halo mass (Sawala et al., 2013; Cui et al., 2014; Velliscig et al., 2014; Schaller et al., 2015). The top panel of Fig. 4.3 shows the ratio of $M_{200,\text{crit}}$ from the hydrodynamical simulations with those of the collisionless simulations in bins of $M_{200,\text{crit}}$ of the halo from the collisionless simulation, for each cosmology. It shows that baryonic effects suppress the masses of haloes by up to $\approx 15\%$ at $10^{13} M_\odot$ but this suppression is less effective at lower and higher masses, consistent with M17 and S20. This peak in suppression is due to

the mass dependence of the feedback efficiency of active galactic nuclei (AGN). The suppression is reduced in magnitude at higher masses owing to the increased binding energies of those haloes. In the bottom panel of Fig. 4.3 I plot the effect of the DDE cosmologies on the halo mass for the hydrodynamical simulations normalised by the effect of DDE in the collisionless simulations (for each cosmology). The impact of baryons on the halo is independent of the nature of DDE at the level of $< 1\%$ over the entire mass range. Likewise, the effect of DDE cosmologies on halo mass is independent of baryonic physics.

4.3 Halo structure

4.3.1 Density profiles

Finally, I examine the separability of cosmological and baryonic effects on the total matter density profiles, described in Section 3.5.2. Fig. 4.4 shows the total matter density profiles in bins of $M_{200,\text{crit}}$ of haloes from the hydrodynamical simulation (lines) and of the collisionless simulations where the baryonic effects (crosses) are applied in post-processing according to Equation 4.1. Unlike in Fig. 3.9, these haloes have not been matched to the collisionless simulations.

The effects of feedback and changes in cosmology are separable to $< 1\%$ for haloes within the mass range $M_{200,\text{crit}}=10^{12.5} - 10^{14} M_{\odot}$. The errors in the separability are slightly larger for lower-mass haloes, likely because they are sampled by fewer particles, and at the highest masses, plausibly as a result of relatively poor statistics.

4.4 Summary

The effects of changing cosmology were compared to the effects of baryons, investigating their dependence on each other. In general, baryons tend to suppress the statistics considered here, at levels of up to 10-20%. Baryons also have a strong scale depen-

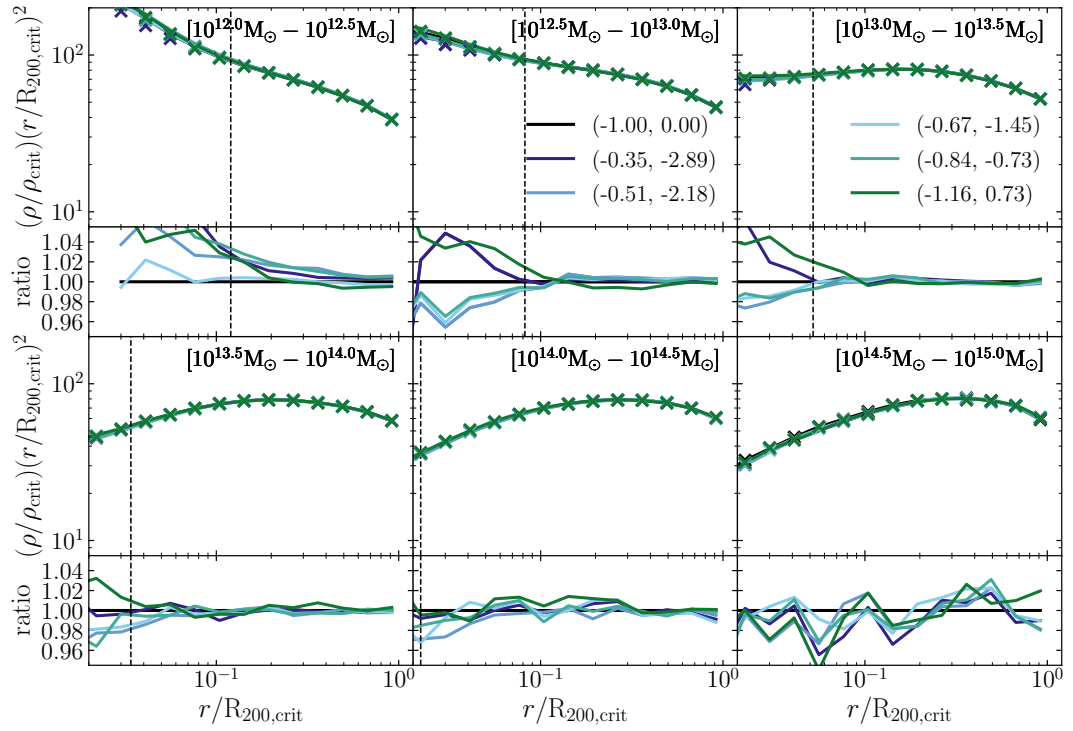


Figure 4.4: Median radial total mass density profiles for the different DDE cosmologies from the hydrodynamical simulations (lines) and the collisionless simulations with added baryonic effects (crosses) as described by Equation 4.1. The ratio is of the hydrodynamical density profiles and the collisionless density profiles with added baryonic effects. Each panel shows different mass bins with width 0.5 dex in $M_{200,\text{crit}}$. Colours indicate different cosmologies where bracketed values refer to the values of (w_0, w_a) . The dashed vertical lines show the median convergence radius (see Section 3.5.2) for haloes in that mass bin below which the density profiles should not be trusted.

dence for $P(k)$ and a more complicated mass dependence for the HMF compared to that of DDE cosmologies. I investigated the separability of cosmological and baryonic effects on our LSS statistics, by assuming that each effect can be treated as a simple multiplicative factor described by Equation 4.1. In general, I find that effects due to the different DDE cosmologies and baryonic physics can be separated to high accuracy in this way, with errors of at most a few percent. More specifically, errors in the separability in $P(k)$ are $< 0.1\%$ (see Fig. 4.1), the lowest in any of our statistics, while in the HMF and density profiles the errors are typically $\approx 1-2\%$ (see Fig. 4.2).

This result opens a new avenue for models that can predict collisionless, DM statistics for a variety of cosmologies. These models can use these results to justify correcting their statistics for the effect of baryons using a post-processing step. Of course, the impact of baryons is not precisely known, in that different simulations predict different effects. At the present, most of this variation is likely due to lack of calibration on quantities important for LSS (such as hot gas fractions). As already mentioned, BAHAMAS is the first simulation programme to explicitly calibrate the feedback with LSS cosmology in mind. It remains to be seen whether or not important differences are still present after all simulations are calibrated in the same way.

An important point to be made is that even though I show how baryons and cosmology are separable, this does not mean that they are not degenerate. Both can result in similar effects on a given statistic, especially when considering the limited dynamic range sampled, e.g. a window in k for the matter power spectrum. Fitting a quantity for baryons and cosmology simultaneously can not be done without addressing this.

Chapter 5

Summary and future work

5.1 Summary

In this final chapter I provide a brief summary of the thesis and a discuss of possible future work. I started off, in Chapter 1, by introducing the standard model of cosmology, Λ CDM, along with a brief description of the history of our Universe in the Λ CDM framework. I then gave a theoretical background to the Λ CDM model, listed some of the key assumptions and covered the main free parameters that observational cosmology is trying to constrain. Following this, I focused on the theoretical description for the observed accelerated expansion at the present day, fulfilled by the cosmological constant in Λ CDM, and motivated the attempt to pursue more complex forms of DE, which are one of the main components of this thesis, in order to relieve some of the theoretically unsatisfactory properties of the cosmological constant. Importantly, the nomenclature of the DDE models used in this work are introduced. Chapter 1 concluded with a review of observational methods to constrain DE; firstly, I covered geometric probes that constrain the expansion history of the Universe directly and secondly, I motivated the use of LSS probes as a complementary approach to geometric probes to constrain DE through measuring the growth of structure.

Chapter 2 introduces and motivates the use of cosmological hydrodynamical simula-

tions as tools for computing accurate theoretical predictions of LSS statistics. I started by reviewing the numerical methods employed by simulations: the use of gravity solvers for collisionless systems, the inclusion of hydrodynamics to model collisional systems and the crucial implementation of subgrid physics to approximately describe important astrophysical processes. I used these to present a more thorough description of BAHAMAS, the suite of simulations that are used in this thesis. The final part of Chapter 2 presents a detailed discussion of my approach to generate DDE cosmologies of interest that are consistent with observations. I covered cosmological parameter constraints from a combination of observational data and consider possible remaining systematics in the CMB data, in the form of A_{lens} . The chapter concluded by stating the final 6 cosmologies and briefly examining their theoretical behaviours. The discussion of the following results is framed in such a way that I make statements of trends relative to the cosmology as a whole, rather than attributing effects to the specific DDE part of each cosmological model.

Chapter 3 investigated a range of statistics from the collisionless simulations. The analysis throughout this work aims at quantifying the effect of the DDE cosmologies on the chosen statistics relative to the Λ CDM cosmology. A consistent behaviour of the DDE cosmologies is that any trend in the freezing model is generally the opposite in the thawing models. I show that the clustering of matter, in the form of the matter power spectrum and the 2-point auto-correlation function of haloes, is affected up to $\approx 10\%$, where the thawing models enhance and the freezing model suppressed the clustering. The abundance of haloes is also strongly affected and the effect has a clear mass dependence. For the thawing cosmologies, lower-mass haloes show a suppression in abundance of $\sim 5\%$ whereas the higher-mass haloes show a drastic enhancement of $\approx 10\text{-}20\%$. This trend is reversed for the freezing cosmology. Alongside the abundance, I also show that the mass of matched haloes between cosmologies at $z = 0$ is impacted by the DDE cosmologies. This led to the investigation of these mass differences in the form of the mass accretion history and the mass accretion rates as a function of scale factor. Mass accretion rates of haloes, relative to Λ CDM, were impacted up to $\approx 25\%$ independent of halo mass. Thawing cosmologies showed the

highest impact, suppressing mass accretion between $a = 0.4 - 0.8$ and enhancing mass accretion at $a > 0.8$. This raised the question of whether these global impacts to the population of haloes impacted their internal structure as well. I examined the radial velocity profiles of haloes which displayed differences although the absolute sizes of those velocity changes were small. The DDE cosmologies impacted the radial density profiles of matched haloes more, showing a maximum enhancement in amplitude of $\approx 10\%$ for the freezing cosmology. This change is consistent with the change in halo mass between the different cosmologies. The logarithmic slope of the density profiles, containing the feature of the splashback radius, and the concentration-mass relations showed very little changes with cosmology.

In the previous chapter, Chapter 4, I examined the impact of baryons on a set of statistics from Chapter 3. The aim was to quantify the degree in which cosmological and baryonic effects were correlated, which was given the term ‘separability’. In other words, I wanted to investigate if the cosmology affected the baryonic physics, and vice versa, and if one could simply model both effects separately given the simple *ansatz* in Equation 4.1. I showed, for the first time, that by modeling the contribution of baryons and cosmology as simple multiplicative factors, the correct statistics are obtained to high accuracy, with errors of the order of a few percent. The baryonic suppression on the matter power spectrum has been well documented and I showed that the cosmological effect due to DDE can be well separated with errors of $<0.1\%$. I also showed that the baryonic and cosmological effects on the abundance of haloes and on the density profiles can be separated with errors of $\approx 1 - 2\%$. This leads to the conclusion that baryonic and cosmological affect from DDE are independent.

In conclusion, the impact of DDE in CMB-constrained cosmologies results in significant effects on a variety of LSS metrics which should be testable with upcoming LSS surveys. For example, LSST¹ and Euclid² are anticipated to measure the matter power spectrum at the percent level (Huterer, 2002; Huterer and Takada, 2005; Hearin et al., 2012), while the differences in the DDE models I consider can reach up to ten

¹<https://www.lsst.org/>

²<https://www.euclid-ec.org/>

times this level. Additionally, the effect of DDE appears to be independent of baryonic physics which makes the modeling and appropriate inclusion of these contributing factors simpler for future theoretical predictions. Of course, this relies on reducing the existing uncertainties in the different approaches of modeling baryonic physics in a range of cosmological simulations. van Daalen et al. (2020) show that existing simulations can affect the matter power spectrum between 10-30% simply through different implementations of subgrid models and their calibration. However, they also show that these differences correlate well with the mean baryon fraction in massive haloes, arguing that this property may allow one to correct dark matter only power spectra down to percent level accuracy. The prospects for using future LSS observations together with detailed predictions from cosmological simulations to place interesting constraints on DDE are therefore bright.

5.2 Future work

The results of this thesis have the potential to be expanded upon and be used as stepping stones for accurate theoretical predictions for the next generation of surveys. I have shown that the differences in LSS statistics between the different DDE cosmologies should be detectable by future surveys. However, as mentioned in my outline of the cosmological parameter selection, one of the main limitations of this work is that I could only run a select few simulations. This limited the theoretical inference of this work to a case study on the effects of DDE. I would like to generate theoretical predictions for more than 6 cosmologies, ideally for any cosmology within a given parameter range. For example, the MCMC analysis can give theoretical predictions for any given point within a multidimensional cosmological parameter space and compare these to observations to gain a handle on the underlying allowed parameter constraints. However, it is simply not feasible to run a simulation for every single sample in the MCMC chain, which consist of hundreds of thousands of samples and are not guaranteed to be the same for every MCMC run due to the random sampling. This has forced the field to adopt less accurate analytic or semi-analytic approaches when generating theoretic-

cal predictions for cosmological parameter inference due to their lower computational cost over cosmological simulations.

A viable solution to this has been proposed through interpolation methods called emulators. The basic strategy of emulators is to evenly sample a given cosmological parameter space with simulations, the simplest being a lattice. The statistic of choice is measured for each of these simulations, e.g. the matter power spectrum. The final part of an emulator is to interpolate the statistic as a function of cosmological parameters, so that any combination of parameters within the cosmological parameter space has an associated solution for that statistic. The power of emulators comes from the relatively small number of simulations needed to gain accurate interpolation results, relative to the unfeasible brute-force method suggested above, and the speed with which these statistics can be returned once the emulator is built, which is comparable to the semi-analytic methods typically employed.

This method has been successfully applied over recent years to construct emulators of the non-linear matter power spectrum (Heitmann et al., 2014; Lawrence et al., 2017; Euclid Collaboration et al., 2019), the galaxy power spectrum (Kwan et al., 2015), the galaxy clustering (Zhai et al., 2019), the halo mass function (McClintock et al., 2019; Bocquet et al., 2020) and the concentration-mass relation (Kwan et al., 2013). However, one aspect that none of the existing emulators include is the effect of baryons. The emulators for the non-linear matter power spectrum require a very high accuracy of $\approx 1\%$ to be able to fully exploit the next generation of surveys. Euclid Collaboration et al. (2019) discuss how the baryonic effect impacts the medium to small scales significantly and that accounting for this is important, yet different studies achieve different levels of suppression of the matter power spectrum due to different forms of feedback. van Daalen et al. (2020) shows that the baryonic suppression of the matter power spectrum from different simulations with different feedback prescriptions correlates very well with the baryon fraction (see Fig. 16). This could be incorporated into an emulator which would make it possible to marginalise over different feedback strengths. Another advantage of including hydrodynamics would be the ability to build emulators on directly observable quantities, e.g. the thermal SZ-lensing cross-correlation spec-

trum. It would also eliminate any residual errors from the simple solution of correcting DM emulation results for baryonic affect using the separability shown in Chapter 4.

Another avenue, which can be combined with the emulators outlined above, is the inclusion of other extensions to Λ CDM, specifically the running of the spectrum index (Stafford et al., 2020) and massive neutrinos (Mummery et al., 2017). It would be very interesting to explore the possible degeneracies in the LSS statistics between these extensions which can produce similar effects, as I have mentioned in this work. In fact, doing this without the use of emulators would make it extremely difficult since these extension would result in a total of 4 free parameters which would take a considerable number of simulations to explore competently.

Appendix A

Appendix

In this section we show how we can use the HMF fitting function from Tinker et al. (2008) to gain some insight into the trends we observe in the HMF for our different cosmologies in Fig. 3.3.

The fitting function provided in Tinker et al. (2008) is an attempt to describe the abundance of dark matter haloes as a function of the matter power spectrum. It is given by

$$\frac{dn}{dM} = f(\sigma) \frac{\bar{\rho}_m}{M} \frac{d \ln \sigma^{-1}}{dM} \quad (\text{A.1})$$

where $\bar{\rho}_m$ is the mean matter density which depends on Ω_m , and $f(\sigma)$ is given as

$$f(\sigma) = A \left[\left(\frac{\sigma}{b} \right)^{-a} + 1 \right] e^{-c/\sigma^2} \quad (\text{A.2})$$

where A , a , b , and c are constants calibrated to simulations, and σ is the rms density fluctuation in a sphere of radius R ,

$$\sigma^2(R) = \frac{1}{2\pi^2} \int_0^\infty k^2 P(k) |W(kR)|^2 dk, \quad (\text{A.3})$$

where $W(kR)$ is the Fourier transform of the real-space top-hat window function and $P(k)$ is the linear matter power spectrum.

Through Equation A.1, we can decompose the abundance of haloes into three separate terms; $f(\sigma)$ which depends on a set of constants and a cosmology-dependent $P(k)$, $\frac{\bar{\rho}_m}{M}$ which is cosmology dependent through its Ω_m dependence, and $\frac{d\ln\sigma^{-1}}{dM}$ which is also dependent on cosmology through $P(k)$. To investigate the impact that each of these terms has on the final HMF, we show them as a function of halo mass in Fig. A.1 for our cosmologies at $z = 0$, normalised by their respective Λ CDM cosmology solution. The $f(\sigma)$ term changes the abundance of high-mass haloes that are still forming at $z = 0$ but leaves the low-mass end unaffected. The $\frac{\bar{\rho}_m}{M}$ term, which is effectively just a change in Ω_m , creates a constant offset equal to the fractional difference between the values of Ω_m for the cosmologies compared to the value of the Λ CDM cosmology. The $\frac{d\ln\sigma^{-1}}{dM}$ term also shows an almost constant, but negligible, offset. Fig. A.1 can then be used to explain the trends we see in the HMF for the different cosmologies in Fig. 3.3. Firstly, the low-mass trend is dominated by changes in Ω_m between the cosmologies and, secondly, the effect at the high-mass end is a combination of this offset and changes in $P(k)$ that cause a suppression or enhancement of the HMF at the high-mass end.

For completeness we also compare the HMF from the simulations to the results from the fitting function of Tinker et al. (2008) in Fig. A.2. The ratios have been taken with the Λ CDM cosmology for the collisionless simulations (crosses) and the HMF fitting function (lines), respectively. We see that the fitting function reproduces the relative difference between the cosmologies well and over the entire mass range probed by the simulations, although there is some scatter at the high-mass end for the simulation results which make the direct comparison more challenging.

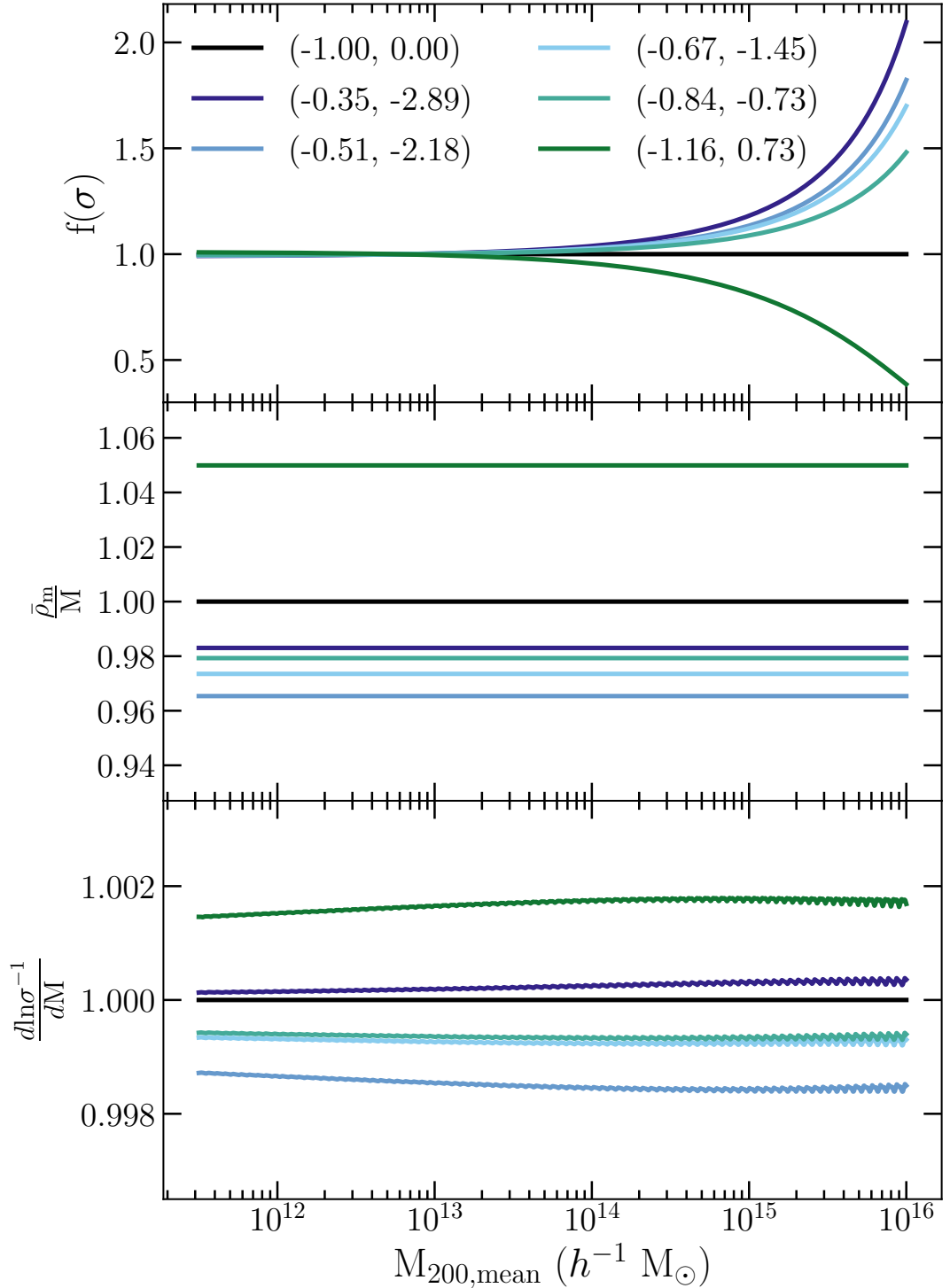


Figure A.1: The HMF fitting function from Tinker et al. (2008) given in Equation A.1 split into three separate terms and plotted against halo mass. Each line represents one of our cosmologies normalised by the Λ CDM cosmology at $z = 0$. Colours indicate different cosmologies (see Table 2.2) where bracketed values refer to the values of (w_0, w_a) .

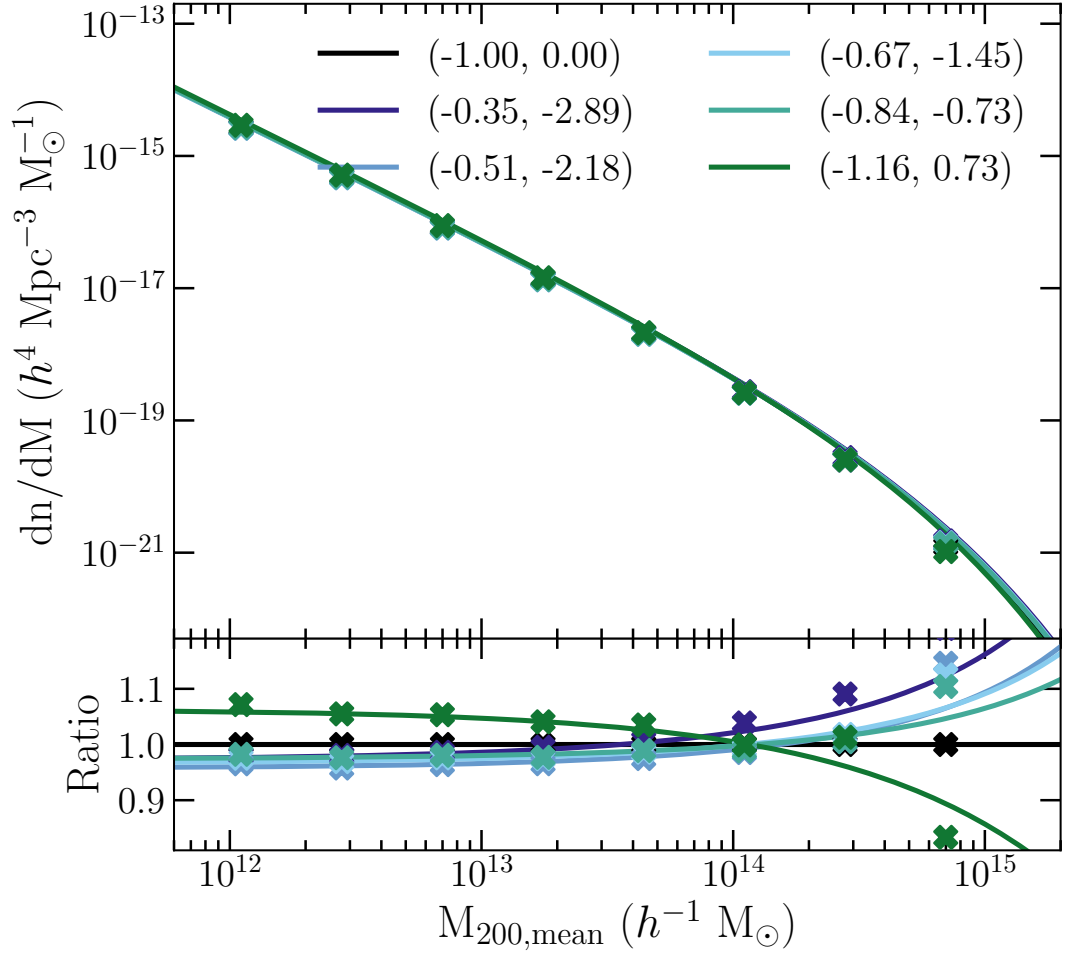


Figure A.2: *Top:* The HMF fitting function described in Equation A.1 (lines) and the HMF from the collisionless simulations (crosses) for each of the cosmologies at $z = 0$. *Bottom:* The ratios of the fitting function and the simulation HMF relative to their respective Λ CDM cosmology solution. Colours indicate different cosmologies (see Table 2.2) where bracketed values refer to the values of (w_0, w_a) .

Bibliography

- A. Friedmann. Über die Krümmung des Raumes. *Zeitschrift für Physik*, 10:377–386, January 1922. doi: 10.1007/BF01332580.
- P. de Bernardis, P. A. R. Ade, J. J. Bock, J. R. Bond, J. Borrill, A. Boscaleri, K. Coble, B. P. Crill, G. De Gasperis, P. C. Farese, P. G. Ferreira, K. Ganga, M. Giacometti, E. Hivon, V. V. Hristov, A. Iacoangeli, A. H. Jaffe, A. E. Lange, L. Martinis, S. Masi, P. V. Mason, P. D. Mauskopf, A. Melchiorri, L. Miglio, T. Montroy, C. B. Netterfield, E. Pascale, F. Piacentini, D. Pogosyan, S. Prunet, S. Rao, G. Romeo, J. E. Ruhl, F. Scaramuzzi, D. Sforna, and N. Vittorio. A flat Universe from high-resolution maps of the cosmic microwave background radiation. *Nature*, 404:955–959, April 2000.
- A. H. Jaffe, P. A. Ade, A. Balbi, J. J. Bock, J. R. Bond, J. Borrill, A. Boscaleri, K. Coble, B. P. Crill, P. de Bernardis, P. Farese, P. G. Ferreira, K. Ganga, M. Giacometti, S. Hanany, E. Hivon, V. V. Hristov, A. Iacoangeli, A. E. Lange, A. T. Lee, L. Martinis, S. Masi, P. D. Mauskopf, A. Melchiorri, T. Montroy, C. B. Netterfield, S. Oh, E. Pascale, F. Piacentini, D. Pogosyan, S. Prunet, B. Rabbii, S. Rao, P. L. Richards, G. Romeo, J. E. Ruhl, F. Scaramuzzi, D. Sforna, G. F. Smoot, R. Stompor, C. D. Winant, and J. H. Wu. Cosmology from MAXIMA-1, BOOMERANG, and COBE DMR Cosmic Microwave Background Observations. *Physical Review Letters*, 86:3475–3479, April 2001. doi: 10.1103/PhysRevLett.86.3475.
- José Alberto Rubiño-Martin, Rafael Rebolo, Pedro Carreira, Kieran Cleary, Rod D. Davies, Richard J. Davis, Clive Dickinson, Keith Grainge, Carlos M. Gutiérrez, Michael P. Hobson, Michael E. Jones, Rüdiger Kneissl, Anthony Lasenby, Klaus Maisinger, Carolina Ödman, Guy G. Pooley, Pedro J. Sosa Molina, Ben Rusholme,

- Richard D. E. Saunders, Richard Savage, Paul F. Scott, Anže Slosar, Angela C. Taylor, David Titterton, Elizabeth Waldram, Robert A. Watson, and Althea Wilkinson. First results from the Very Small Array - IV. Cosmological parameter estimation. *MNRAS*, 341(4):1084–1092, June 2003. doi: 10.1046/j.1365-8711.2003.06494.x.
- J. W. Fowler, V. Acquaviva, P. A. R. Ade, P. Aguirre, M. Amiri, J. W. Appel, L. F. Barrientos, E. S. Battistelli, J. R. Bond, B. Brown, B. Burger, J. Chervenak, S. Das, M. J. Devlin, S. R. Dicker, W. B. Doriese, J. Dunkley, R. Dünner, T. Essinger-Hileman, R. P. Fisher, A. Hajian, M. Halpern, M. Hasselfield, C. Hernández-Monteagudo, G. C. Hilton, M. Hilton, A. D. Hincks, R. Hlozek, K. M. Huffenberger, D. H. Hughes, J. P. Hughes, L. Infante, K. D. Irwin, R. Jimenez, J. B. Juin, M. Kaul, J. Klein, A. Kosowsky, J. M. Lau, M. Limon, Y. T. Lin, R. H. Lupton, T. A. Marriage, D. Marsden, K. Martocci, P. Mausekopf, F. Menanteau, K. Moodley, H. Moseley, C. B. Netterfield, M. D. Niemack, M. R. Nolta, L. A. Page, L. Parker, B. Partridge, H. Quintana, B. Reid, N. Sehgal, J. Sievers, D. N. Spergel, S. T. Staggs, D. S. Swetz, E. R. Switzer, R. Thornton, H. Trac, C. Tucker, L. Verde, R. Warne, G. Wilson, E. Wollack, and Y. Zhao. The Atacama Cosmology Telescope: A Measurement of the 600 < ell < 8000 Cosmic Microwave Background Power Spectrum at 148 GHz. *ApJ*, 722(2):1148–1161, October 2010. doi: 10.1088/0004-637X/722/2/1148.
- G. Hinshaw, D. Larson, E. Komatsu, D. N. Spergel, C. L. Bennett, J. Dunkley, M. R. Nolta, M. Halpern, R. S. Hill, N. Odegard, L. Page, K. M. Smith, J. L. Weiland, B. Gold, N. Jarosik, A. Kogut, M. Limon, S. S. Meyer, G. S. Tucker, E. Wollack, and E. L. Wright. Nine-year Wilkinson Microwave Anisotropy Probe (WMAP) Observations: Cosmological Parameter Results. *ApJS*, 208(2):19, October 2013. doi: 10.1088/0067-0049/208/2/19.
- Planck Collaboration, N. Aghanim, Y. Akrami, M. Ashdown, J. Aumont, C. Baccigalupi, M. Ballardini, A. J. Banday, R. B. Barreiro, N. Bartolo, S. Basak, R. Battye, K. Benabed, J. P. Bernard, M. Bersanelli, P. Bielewicz, J. J. Bock, J. R. Bond, J. Borrill, F. R. Bouchet, F. Boulanger, M. Bucher, C. Burigana, R. C. Butler, E. Calabrese, J. F. Cardoso, J. Carron, A. Challinor, H. C. Chiang, J. Chluba, L. P. L.

Colombo, C. Combet, D. Contreras, B. P. Crill, F. Cuttaia, P. de Bernardis, G. de Zotti, J. Delabrouille, J. M. Delouis, E. Di Valentino, J. M. Diego, O. Doré, M. Douspis, A. Ducout, X. Dupac, S. Dusini, G. Efstathiou, F. Elsner, T. A. Enßlin, H. K. Eriksen, Y. Fantaye, M. Farhang, J. Fergusson, R. Fernandez-Cobos, F. Finelli, F. Forastieri, M. Frailis, A. A. Fraisse, E. Franceschi, A. Frolov, S. Galeotta, S. Galli, K. Ganga, R. T. Génova-Santos, M. Gerbino, T. Ghosh, J. González-Nuevo, K. M. Górski, S. Gratton, A. Gruppuso, J. E. Gudmundsson, J. Hamann, W. Handley, F. K. Hansen, D. Herranz, S. R. Hildebrandt, E. Hivon, Z. Huang, A. H. Jaffe, W. C. Jones, A. Karakci, E. Keihänen, R. Keskitalo, K. Kiiveri, J. Kim, T. S. Kisner, L. Knox, N. Krachmalnicoff, M. Kunz, H. Kurki-Suonio, G. Lagache, J. M. Lamarre, A. Lasenby, M. Lattanzi, C. R. Lawrence, M. Le Jeune, P. Lemos, J. Lesgourgues, F. Levrier, A. Lewis, M. Liguori, P. B. Lilje, M. Lilley, V. Lindholm, M. López-Caniego, P. M. Lubin, Y. Z. Ma, J. F. Macías-Pérez, G. Maggio, D. Maino, N. Mandolesi, A. Mangilli, A. Marcos-Caballero, M. Maris, P. G. Martin, M. Martinelli, E. Martínez-González, S. Matarrese, N. Mauri, J. D. McEwen, P. R. Meinhold, A. Melchiorri, A. Mennella, M. Migliaccio, M. Millea, S. Mitra, M. A. Miville-Deschênes, D. Molinari, L. Montier, G. Morgante, A. Moss, P. Natoli, H. U. Nørgaard-Nielsen, L. Pagano, D. Paoletti, B. Partridge, G. Patanchon, H. V. Peiris, F. Perrotta, V. Pettorino, F. Piacentini, L. Polastri, G. Polenta, J. L. Puget, J. P. Rachen, M. Reinecke, M. Remazeilles, A. Renzi, G. Rocha, C. Rosset, G. Roudier, J. A. Rubiño-Martín, B. Ruiz-Granados, L. Salvati, M. Sandri, M. Savelainen, D. Scott, E. P. S. Shellard, C. Sirignano, G. Sirri, L. D. Spencer, R. Sunyaev, A. S. Suur-Uski, J. A. Tauber, D. Tavagnacco, M. Tenti, L. Toffolatti, M. Tomasi, T. Trombetti, L. Valenziano, J. Valiviita, B. Van Tent, L. Vibert, P. Vielva, F. Villa, N. Vittorio, B. D. Wandelt, I. K. Wehus, M. White, S. D. M. White, A. Zacchei, and A. Zonca. Planck 2018 results. VI. Cosmological parameters. *arXiv e-prints*, art. arXiv:1807.06209, Jul 2018.

K.-H. Chae. New Modeling of the Lensing Galaxy and Cluster of Q0957+561: Implications for the Global Value of the Hubble Constant. *ApJ*, 524:582–590, October 1999. doi: 10.1086/307842.

- S. Alam, M. Ata, S. Bailey, F. Beutler, D. Bizyaev, J. A. Blazek, A. S. Bolton, J. R. Brownstein, A. Burden, C.-H. Chuang, J. Comparat, A. J. Cuesta, K. S. Dawson, D. J. Eisenstein, S. Escoffier, H. Gil-Marín, J. N. Grieb, N. Hand, S. Ho, K. Kinemuchi, D. Kirkby, F. Kitaura, E. Malanushenko, V. Malanushenko, C. Maraston, C. K. McBride, R. C. Nichol, M. D. Olmstead, D. Oravetz, N. Padmanabhan, N. Palanque-Delabrouille, K. Pan, M. Pellejero-Ibanez, W. J. Percival, P. Petitjean, F. Prada, A. M. Price-Whelan, B. A. Reid, S. A. Rodríguez-Torres, N. A. Roe, A. J. Ross, N. P. Ross, G. Rossi, J. A. Rubiño-Martín, A. G. Sánchez, S. Saito, S. Salazar-Albornoz, L. Samushia, S. Satpathy, C. G. Scóccola, D. J. Schlegel, D. P. Schneider, H.-J. Seo, A. Simmons, A. Slosar, M. A. Strauss, M. E. C. Swanson, D. Thomas, J. L. Tinker, R. Tojeiro, M. Vargas Magaña, J. A. Vazquez, L. Verde, D. A. Wake, Y. Wang, D. H. Weinberg, M. White, W. M. Wood-Vasey, C. Yèche, I. Zehavi, Z. Zhai, and G.-B. Zhao. The clustering of galaxies in the completed SDSS-III Baryon Oscillation Spectroscopic Survey: cosmological analysis of the DR12 galaxy sample. *ArXiv e-prints*, July 2016.
- D. M. Scolnic, D. O. Jones, A. Rest, Y. C. Pan, R. Chornock, R. J. Foley, M. E. Huber, R. Kessler, G. Narayan, A. G. Riess, S. Rodney, E. Berger, D. J. Brout, P. J. Challis, M. Drout, D. Finkbeiner, R. Lunnan, R. P. Kirshner, N. E. Sanders, E. Schlafly, S. Smartt, C. W. Stubbs, J. Tonry, W. M. Wood-Vasey, M. Foley, J. Hand, E. Johnson, W. S. Burgett, K. C. Chambers, P. W. Draper, K. W. Hodapp, N. Kaiser, R. P. Kudritzki, E. A. Magnier, N. Metcalfe, F. Bresolin, E. Gall, R. Kotak, M. McCrum, and K. W. Smith. The Complete Light-curve Sample of Spectroscopically Confirmed SNe Ia from Pan-STARRS1 and Cosmological Constraints from the Combined Pantheon Sample. *ApJ*, 859(2):101, June 2018. doi: 10.3847/1538-4357/aab9bb.
- Yacine Ali-Haïmoud and Simeon Bird. An efficient implementation of massive neutrinos in non-linear structure formation simulations. *MNRAS*, 428(4):3375–3389, Feb 2013. doi: 10.1093/mnras/sts286.
- Julien Lesgourgues and Sergio Pastor. Massive neutrinos and cosmology. *Phys. Rep.*, 429(6):307–379, July 2006. doi: 10.1016/j.physrep.2006.04.001.

- D. J. Fixsen. The Temperature of the Cosmic Microwave Background. *ApJ*, 707(2): 916–920, December 2009. doi: 10.1088/0004-637X/707/2/916.
- E. R. Harrison. Fluctuations at the Threshold of Classical Cosmology. *Phys. Rev. D*, 1 (10):2726–2730, May 1970. doi: 10.1103/PhysRevD.1.2726.
- Yaa B. Zeldovich. A hypothesis, unifying the structure and the entropy of the Universe. *MNRAS*, 160:1P, January 1972. doi: 10.1093/mnras/160.1.1P.
- P. J. E. Peebles and J. T. Yu. Primeval Adiabatic Perturbation in an Expanding Universe. *ApJ*, 162:815, December 1970. doi: 10.1086/150713.
- Albert Einstein. Kosmologische Betrachtungen zur allgemeinen Relativitätstheorie. *Sitzungsberichte der Königlich Preußischen Akademie der Wissenschaften (Berlin)*, pages 142–152, January 1917.
- G. Lemaître. Un Univers homogène de masse constante et de rayon croissant rendant compte de la vitesse radiale des nébuleuses extra-galactiques. *Annales de la Société Scientifique de Bruxelles*, 47:49–59, January 1927.
- Adam G. Riess, Alexei V. Filippenko, Peter Challis, Alejandro Clocchiatti, Alan Diercks, Peter M. Garnavich, Ron L. Gilliland, Craig J. Hogan, Saurabh Jha, Robert P. Kirshner, B. Leibundgut, M. M. Phillips, David Reiss, Brian P. Schmidt, Robert A. Schommer, R. Chris Smith, J. Spyromilio, Christopher Stubbs, Nicholas B. Suntzeff, and John Tonry. Observational Evidence from Supernovae for an Accelerating Universe and a Cosmological Constant. *AJ*, 116(3):1009–1038, Sep 1998. doi: 10.1086/300499.
- S. Perlmutter, G. Aldering, G. Goldhaber, R. A. Knop, P. Nugent, P. G. Castro, S. Deustua, S. Fabbro, A. Goobar, D. E. Groom, I. M. Hook, A. G. Kim, M. Y. Kim, J. C. Lee, N. J. Nunes, R. Pain, C. R. Pennypacker, R. Quimby, C. Lidman, R. S. Ellis, M. Irwin, R. G. McMahon, P. Ruiz-Lapuente, N. Walton, B. Schaefer, B. J. Boyle, A. V. Filippenko, T. Matheson, A. S. Fruchter, N. Panagia, H. J. M. Newberg, W. J. Couch, and The Supernova Cosmology Project. Measurements of

- Ω and Λ from 42 High-Redshift Supernovae. *ApJ*, 517(2):565–586, June 1999. doi: 10.1086/307221.
- Ronald J. Adler, Brendan Casey, and Ovid C. Jacob. Vacuum catastrophe: An elementary exposition of the cosmological constant problem. *American Journal of Physics*, 63(7):620–626, July 1995. doi: 10.1119/1.17850.
- M. P. Hobson, G. Efstathiou, A. N. Lasenby, and Lawrence H. Ford. General Relativity: An Introduction for Physicists. *Physics Today*, 60(3):62, January 2007. doi: 10.1063/1.2718760.
- Justin Khoury and Amanda Weltman. Chameleon cosmology. *Phys. Rev. D*, 69(4):044026, February 2004. doi: 10.1103/PhysRevD.69.044026.
- Kurt Hinterbichler and Justin Khoury. Screening Long-Range Forces through Local Symmetry Restoration. *Phys. Rev. Lett.*, 104(23):231301, June 2010. doi: 10.1103/PhysRevLett.104.231301.
- C. Wetterich. Cosmology and the fate of dilatation symmetry. *Nuclear Physics B*, 302(4):668–696, Jun 1988. doi: 10.1016/0550-3213(88)90193-9.
- P. J. E. Peebles and Bharat Ratra. Cosmology with a Time-Variable Cosmological “Constant”. *ApJl*, 325:L17, February 1988. doi: 10.1086/185100.
- Bharat Ratra and P. J. E. Peebles. Cosmological consequences of a rolling homogeneous scalar field. *Phys. Rev. D*, 37(12):3406–3427, Jun 1988. doi: 10.1103/PhysRevD.37.3406.
- Joshua A. Frieman, Christopher T. Hill, Albert Stebbins, and Ioav Waga. Cosmology with Ultralight Pseudo Nambu-Goldstone Bosons. *Phys. Rev. Lett.*, 75(11):2077–2080, September 1995. doi: 10.1103/PhysRevLett.75.2077.
- R. R. Caldwell, R. Dave, and P. J. Steinhardt. Quintessential Cosmology Novel Models of Cosmological Structure Formation. *Ap&SS*, 261:303–310, January 1998. doi: 10.1023/A:1002028230277.

- Ivaylo Zlatev, Limin Wang, and Paul J. Steinhardt. Quintessence, Cosmic Coincidence, and the Cosmological Constant. *Phys. Rev. Lett.*, 82(5):896–899, February 1999. doi: 10.1103/PhysRevLett.82.896.
- R. R. Caldwell and Eric V. Linder. Limits of Quintessence. *Phys. Rev. Lett.*, 95(14):141301, September 2005. doi: 10.1103/PhysRevLett.95.141301.
- C. Wetterich. An asymptotically vanishing time-dependent cosmological “constant”. *A&A*, 301:321, September 1995.
- Pedro G. Ferreira and Michael Joyce. Structure Formation with a Self-Tuning Scalar Field. *Phys. Rev. Lett.*, 79(24):4740–4743, December 1997. doi: 10.1103/PhysRevLett.79.4740.
- Edmund J. Copeland, Andrew R. Liddle, and David Wands. Exponential potentials and cosmological scaling solutions. *Phys. Rev. D*, 57(8):4686–4690, April 1998. doi: 10.1103/PhysRevD.57.4686.
- Steven Weinberg. The cosmological constant problem. *Reviews of Modern Physics*, 61:1–23, January 1989. doi: 10.1103/RevModPhys.61.1.
- Sean M. Carroll. Quintessence and the Rest of the World: Suppressing Long-Range Interactions. *Phys. Rev. Lett.*, 81(15):3067–3070, October 1998. doi: 10.1103/PhysRevLett.81.3067.
- Takeshi Chiba, Takahiro Okabe, and Masahide Yamaguchi. Kinetically driven quintessence. *Phys. Rev. D*, 62(2):023511, July 2000. doi: 10.1103/PhysRevD.62.023511.
- C. Armendariz-Picon, V. Mukhanov, and Paul J. Steinhardt. Essentials of k-essence. *Phys. Rev. D*, 63(10):103510, May 2001. doi: 10.1103/PhysRevD.63.103510.
- Camille Bonvin, Chiara Caprini, and Ruth Durrer. No-Go Theorem for k-Essence Dark Energy. *Phys. Rev. Lett.*, 97(8):081303, August 2006. doi: 10.1103/PhysRevLett.97.081303.

- Eugeny Babichev, Viatcheslav Mukhanov, and Alexander Vikman. k-Essence, superluminal propagation, causality and emergent geometry. *Journal of High Energy Physics*, 2008(2):101, February 2008. doi: 10.1088/1126-6708/2008/02/101.
- Asantha R. Cooray and Dragan Huterer. Gravitational Lensing as a Probe of Quintessence. *ApJ*, 513(2):L95–L98, March 1999. doi: 10.1086/311927.
- Brian F. Gerke and G. Efstathiou. Probing quintessence: reconstruction and parameter estimation from supernovae. *MNRAS*, 335(1):33–43, September 2002. doi: 10.1046/j.1365-8711.2002.05612.x.
- Michel Chevallier and David Polarski. Accelerating Universes with Scaling Dark Matter. *International Journal of Modern Physics D*, 10:213–223, January 2001. doi: 10.1142/S0218271801000822.
- Eric V. Linder. Exploring the Expansion History of the Universe. *Phys. Rev. Lett.*, 90:091301, March 2003. doi: 10.1103/PhysRevLett.90.091301.
- Varun Sahni and Alexei Starobinsky. Reconstructing Dark Energy. *International Journal of Modern Physics D*, 15(12):2105–2132, January 2006. doi: 10.1142/S0218271806009704.
- C. T. Kowal. Absolute magnitudes of supernovae. *AJ*, 73:1021–1024, December 1968. doi: 10.1086/110763.
- S. A. Colgate. Supernovae as a standard candle for cosmology. *ApJ*, 232:404–408, September 1979. doi: 10.1086/157300.
- M. M. Phillips. The Absolute Magnitudes of Type IA Supernovae. *ApJ*, 413:L105, August 1993. doi: 10.1086/186970.
- Adam G. Riess, William H. Press, and Robert P. Kirshner. A Precise Distance Indicator: Type IA Supernova Multicolor Light-Curve Shapes. *ApJ*, 473:88, December 1996. doi: 10.1086/178129.
- Robert Tripp. A two-parameter luminosity correction for Type IA supernovae. *A&A*, 331:815–820, March 1998.

- A. Conley, J. Guy, M. Sullivan, N. Regnault, P. Astier, C. Balland, S. Basa, R. G. Carlberg, D. Fouchez, D. Hardin, I. M. Hook, D. A. Howell, R. Pain, N. Palanque-Delabrouille, K. M. Perrett, C. J. Pritchett, J. Rich, V. Ruhlmann-Kleider, D. Balam, S. Baumont, R. S. Ellis, S. Fabbro, H. K. Fakhouri, N. Fourmanoit, S. González-Gaitán, M. L. Graham, M. J. Hudson, E. Hsiao, T. Kronborg, C. Lidman, A. M. Mourao, J. D. Neill, S. Perlmutter, P. Ripoche, N. Suzuki, and E. S. Walker. Supernova Constraints and Systematic Uncertainties from the First Three Years of the Supernova Legacy Survey. *ApJS*, 192(1):1, January 2011. doi: 10.1088/0067-0049/192/1/1.
- D. Rubin, G. Aldering, K. Barbary, K. Boone, G. Chappell, M. Currie, S. Deustua, P. Fagrellius, A. Fruchter, B. Hayden, C. Lidman, J. Nordin, S. Perlmutter, C. Saunders, C. Sofiatti, and The Supernova Cosmology Project. UNITY: Confronting Supernova Cosmology's Statistical and Systematic Uncertainties in a Unified Bayesian Framework. *ApJ*, 813(2):137, November 2015. doi: 10.1088/0004-637X/813/2/137.
- M. C. March, R. Trotta, P. Berkes, G. D. Starkman, and P. M. Vaudrevange. Improved constraints on cosmological parameters from Type Ia supernova data. *MNRAS*, 418(4):2308–2329, December 2011. doi: 10.1111/j.1365-2966.2011.19584.x.
- Adam G. Riess, Stefano Casertano, Wenlong Yuan, Lucas M. Macri, and Dan Scolnic. Large Magellanic Cloud Cepheid Standards Provide a 1% Foundation for the Determination of the Hubble Constant and Stronger Evidence for Physics beyond Λ CDM. *ApJ*, 876(1):85, May 2019. doi: 10.3847/1538-4357/ab1422.
- R. A. Sunyaev and Ya. B. Zeldovich. Small-Scale Fluctuations of Relic Radiation. *Ap&SS*, 7(1):3–19, April 1970. doi: 10.1007/BF00653471.
- Daniel J. Eisenstein, Idit Zehavi, David W. Hogg, Roman Scoccimarro, Michael R. Blanton, Robert C. Nichol, Ryan Scranton, Hee-Jong Seo, Max Tegmark, Zheng Zheng, Scott F. Anderson, Jim Annis, Neta Bahcall, Jon Brinkmann, Scott Burles, Francisco J. Castander, Andrew Connolly, Istvan Csabai, Mamoru Doi, Masataka Fukugita, Joshua A. Frieman, Karl Glazebrook, James E. Gunn, John S. Hendry, Gregory Hennessy, Zeljko Ivezić, Stephen Kent, Gillian R. Knapp, Huan Lin,

- Yeong-Shang Loh, Robert H. Lupton, Bruce Margon, Timothy A. McKay, Avery Meiksin, Jeffery A. Munn, Adrian Pope, Michael W. Richmond, David Schlegel, Donald P. Schneider, Kazuhiro Shimasaku, Christopher Stoughton, Michael A. Strauss, Mark SubbaRao, Alexander S. Szalay, István Szapudi, Douglas L. Tucker, Brian Yanny, and Donald G. York. Detection of the Baryon Acoustic Peak in the Large-Scale Correlation Function of SDSS Luminous Red Galaxies. *ApJ*, 633(2): 560–574, November 2005. doi: 10.1086/466512.
- Shaun Cole, Will J. Percival, John A. Peacock, Peder Norberg, Carlton M. Baugh, Carlos S. Frenk, Ivan Baldry, Joss Bland-Hawthorn, Terry Bridges, Russell Cannon, Matthew Colless, Chris Collins, Warrick Couch, Nicholas J. G. Cross, Gavin Dalton, Vincent R. Eke, Roberto De Propris, Simon P. Driver, George Efstathiou, Richard S. Ellis, Karl Glazebrook, Carole Jackson, Adrian Jenkins, Ofer Lahav, Ian Lewis, Stuart Lumsden, Steve Maddox, Darren Madgwick, Bruce A. Peterson, Will Sutherland, and Keith Taylor. The 2dF Galaxy Redshift Survey: power-spectrum analysis of the final data set and cosmological implications. *MNRAS*, 362(2):505–534, September 2005. doi: 10.1111/j.1365-2966.2005.09318.x.
- Nikhil Padmanabhan, David J. Schlegel, Uroš Seljak, Alexey Makarov, Neta A. Bahcall, Michael R. Blanton, Jonathan Brinkmann, Daniel J. Eisenstein, Douglas P. Finkbeiner, James E. Gunn, David W. Hogg, Željko Ivezić, Gillian R. Knapp, Jon Loveday, Robert H. Lupton, Robert C. Nichol, Donald P. Schneider, Michael A. Strauss, Max Tegmark, and Donald G. York. The clustering of luminous red galaxies in the Sloan Digital Sky Survey imaging data. *MNRAS*, 378(3):852–872, July 2007. doi: 10.1111/j.1365-2966.2007.11593.x.
- Will J. Percival, Shaun Cole, Daniel J. Eisenstein, Robert C. Nichol, John A. Peacock, Adrian C. Pope, and Alexander S. Szalay. Measuring the Baryon Acoustic Oscillation scale using the Sloan Digital Sky Survey and 2dF Galaxy Redshift Survey. *MNRAS*, 381(3):1053–1066, November 2007. doi: 10.1111/j.1365-2966.2007.12268.x.
- Florian Beutler, Chris Blake, Matthew Colless, D. Heath Jones, Lister Staveley-Smith, Lachlan Campbell, Quentin Parker, Will Saunders, and Fred Watson. The 6dF

- Galaxy Survey: baryon acoustic oscillations and the local Hubble constant. *MNRAS*, 416(4):3017–3032, October 2011. doi: 10.1111/j.1365-2966.2011.19250.x.
- Ashley J. Ross, Lado Samushia, Cullan Howlett, Will J. Percival, Angela Burden, and Marc Manera. The clustering of the SDSS DR7 main Galaxy sample - I. A 4 per cent distance measure at $z = 0.15$. *MNRAS*, 449(1):835–847, May 2015. doi: 10.1093/mnras/stv154.
- Timothée Delubac, Julian E. Bautista, Nicolás G. Busca, James Rich, David Kirkby, Stephen Bailey, Andreu Font-Ribera, Anže Slosar, Khee-Gan Lee, Matthew M. Pieri, Jean-Christophe Hamilton, Éric Aubourg, Michael Blomqvist, Jo Bovy, Jon Brinkmann, William Carithers, Kyle S. Dawson, Daniel J. Eisenstein, Satya Gontcho A. Gontcho, Jean-Paul Kneib, Jean-Marc Le Goff, Daniel Margala, Jordi Miralda-Escudé, Adam D. Myers, Robert C. Nichol, Pasquier Noterdaeme, Ross O’Connell, Matthew D. Olmstead, Nathalie Palanque-Delabrouille, Isabelle Pâris, Patrick Petitjean, Nicholas P. Ross, Graziano Rossi, David J. Schlegel, Donald P. Schneider, David H. Weinberg, Christophe Yèche, and Donald G. York. Baryon acoustic oscillations in the $\text{Ly}\alpha$ forest of BOSS DR11 quasars. *A&A*, 574:A59, February 2015. doi: 10.1051/0004-6361/201423969.
- Shadab Alam, Metin Ata, Stephen Bailey, Florian Beutler, Dmitry Bizyaev, Jonathan A. Blazek, Adam S. Bolton, Joel R. Brownstein, Angela Burden, Chia-Hsun Chuang, Johan Comparat, Antonio J. Cuesta, Kyle S. Dawson, Daniel J. Eisenstein, Stephanie Escoffier, Héctor Gil-Marín, Jan Niklas Grieb, Nick Hand, Shirley Ho, Karen Kinemuchi, David Kirkby, Francisco Kitaura, Elena Malanushenko, Viktor Malanushenko, Claudia Maraston, Cameron K. McBride, Robert C. Nichol, Matthew D. Olmstead, Daniel Oravetz, Nikhil Padmanabhan, Nathalie Palanque-Delabrouille, Kaike Pan, Marcos Pellejero-Ibanez, Will J. Percival, Patrick Petitjean, Francisco Prada, Adrian M. Price-Whelan, Beth A. Reid, Sergio A. Rodríguez-Torres, Natalie A. Roe, Ashley J. Ross, Nicholas P. Ross, Graziano Rossi, Jose Alberto Rubiño-Martín, Shun Saito, Salvador Salazar-Albornoz, Lado Samushia, Ariel G. Sánchez, Siddharth Satpathy, David J. Schlegel, Donald P. Schneider, Claudia G. Scóccola, Hee-Jong Seo, Erin S. Sheldon, Audrey Simmons, Anže Slosar,

- Michael A. Strauss, Molly E. C. Swanson, Daniel Thomas, Jeremy L. Tinker, Rita Tojeiro, Mariana Vargas Magaña, Jose Alberto Vazquez, Licia Verde, David A. Wake, Yuting Wang, David H. Weinberg, Martin White, W. Michael Wood-Vasey, Christophe Yèche, Idit Zehavi, Zhongxu Zhai, and Gong-Bo Zhao. The clustering of galaxies in the completed SDSS-III Baryon Oscillation Spectroscopic Survey: cosmological analysis of the DR12 galaxy sample. *MNRAS*, 470(3):2617–2652, September 2017. doi: 10.1093/mnras/stx721.
- Victoria de Sainte Agathe, Christophe Balland, Héliion du Mas des Bourboux, Nicolás G. Busca, Michael Blomqvist, Julien Guy, James Rich, Andreu Font-Ribera, Matthew M. Pieri, Julian E. Bautista, Kyle Dawson, Jean-Marc Le Goff, Axel de la Macorra, Nathalie Palanque-Delabrouille, Will J. Percival, Ignasi Pérez-Ràfols, Donald P. Schneider, Anže Slosar, and Christophe Yèche. Baryon acoustic oscillations at $z = 2.34$ from the correlations of $\text{Ly}\alpha$ absorption in eBOSS DR14. *A&A*, 629:A85, September 2019. doi: 10.1051/0004-6361/201935638.
- R. K. Sachs and A. M. Wolfe. Perturbations of a Cosmological Model and Angular Variations of the Microwave Background. *ApJ*, 147:73, January 1967. doi: 10.1086/148982.
- Pablo Fosalba, Enrique Gaztañaga, and Francisco J. Castander. Detection of the Integrated Sachs-Wolfe and Sunyaev-Zeldovich Effects from the Cosmic Microwave Background-Galaxy Correlation. *ApJL*, 597(2):L89–L92, November 2003. doi: 10.1086/379848.
- Tommaso Giannantonio, Ryan Scranton, Robert G. Crittenden, Robert C. Nichol, Stephen P. Boughn, Adam D. Myers, and Gordon T. Richards. Combined analysis of the integrated Sachs-Wolfe effect and cosmological implications. *Phys. Rev. D*, 77(12):123520, June 2008. doi: 10.1103/PhysRevD.77.123520.
- P. J. E. Peebles. *The large-scale structure of the universe*. Princeton Univ. Press, Princeton, NJ, 1980.
- Ryuichi Takahashi, Masanori Sato, Takahiro Nishimichi, Atsushi Taruya, and

- Masamune Oguri. Revising the Halofit Model for the Nonlinear Matter Power Spectrum. *ApJ*, 761(2):152, December 2012. doi: 10.1088/0004-637X/761/2/152.
- Nick Kaiser. Weak Gravitational Lensing of Distant Galaxies. *ApJ*, 388:272, April 1992. doi: 10.1086/171151.
- Wayne Hu and Bhuvnesh Jain. Joint galaxy-lensing observables and the dark energy. *Phys. Rev. D*, 70(4):043009, August 2004. doi: 10.1103/PhysRevD.70.043009.
- N. Kaiser. On the spatial correlations of Abell clusters. *ApJL*, 284:L9–L12, September 1984. doi: 10.1086/184341.
- J. M. Bardeen, J. R. Bond, N. Kaiser, and A. S. Szalay. The Statistics of Peaks of Gaussian Random Fields. *ApJ*, 304:15, May 1986. doi: 10.1086/164143.
- Shaun Cole and Nick Kaiser. Biased clustering in the cold dark matter cosmogony. *MNRAS*, 237:1127–1146, April 1989. doi: 10.1093/mnras/237.4.1127.
- H. J. Mo and S. D. M. White. An analytic model for the spatial clustering of dark matter haloes. *MNRAS*, 282(2):347–361, September 1996. doi: 10.1093/mnras/282.2.347.
- Jeremy L. Tinker, Brant E. Robertson, Andrey V. Kravtsov, Anatoly Klypin, Michael S. Warren, Gustavo Yepes, and Stefan Gottlöber. The Large-scale Bias of Dark Matter Halos: Numerical Calibration and Model Tests. *ApJ*, 724(2):878–886, December 2010. doi: 10.1088/0004-637X/724/2/878.
- Nick Kaiser. Clustering in real space and in redshift space. *MNRAS*, 227:1–21, July 1987. doi: 10.1093/mnras/227.1.1.
- A. J. S. Hamilton. *Linear Redshift Distortions: a Review*, volume 231 of *Astrophysics and Space Science Library*, page 185. 1998. doi: 10.1007/978-94-011-4960-0_17.
- Steve Hatton and Shaun Cole. Estimating β from redshift-space distortions in the 2dF galaxy survey. *MNRAS*, 310(4):1137–1146, December 1999. doi: 10.1046/j.1365-8711.1999.03034.x.

- Jeremy L. Tinker. Redshift-space distortions with the halo occupation distribution - II. Analytic model. *MNRAS*, 374(2):477–492, January 2007. doi: 10.1111/j.1365-2966.2006.11157.x.
- Thomas McClintock, Eduardo Rozo, Matthew R. Becker, Joseph DeRose, Yao-Yuan Mao, Sean McLaughlin, Jeremy L. Tinker, Risa H. Wechsler, and Zhongxu Zhai. The Aemulus Project. II. Emulating the Halo Mass Function. *ApJ*, 872(1):53, February 2019. doi: 10.3847/1538-4357/aaf568.
- Sebastian Bocquet, Katrin Heitmann, Salman Habib, Earl Lawrence, Thomas Uram, Nicholas Frontiere, Adrian Pope, and Hal Finkel. The Mira-Titan Universe. III. Emulation of the Halo Mass Function. *arXiv e-prints*, art. arXiv:2003.12116, March 2020.
- William H. Press and Paul Schechter. Formation of Galaxies and Clusters of Galaxies by Self-Similar Gravitational Condensation. *ApJ*, 187:425–438, February 1974. doi: 10.1086/152650.
- J. R. Bond, S. Cole, G. Efstathiou, and N. Kaiser. Excursion Set Mass Functions for Hierarchical Gaussian Fluctuations. *ApJ*, 379:440, October 1991. doi: 10.1086/170520.
- Andrew R. Zentner. The Excursion Set Theory of Halo Mass Functions, Halo Clustering, and Halo Growth. *International Journal of Modern Physics D*, 16(5):763–815, January 2007. doi: 10.1142/S0218271807010511.
- A. Jenkins, C. S. Frenk, S. D. M. White, J. M. Colberg, S. Cole, A. E. Evrard, H. M. P. Couchman, and N. Yoshida. The mass function of dark matter haloes. *MNRAS*, 321(2):372–384, February 2001. doi: 10.1046/j.1365-8711.2001.04029.x.
- Michael S. Warren, Kevork Abazajian, Daniel E. Holz, and Luís Teodoro. Precision Determination of the Mass Function of Dark Matter Halos. *ApJ*, 646(2):881–885, August 2006. doi: 10.1086/504962.
- Jeremy Tinker, Andrey V. Kravtsov, Anatoly Klypin, Kevork Abazajian, Michael Warren, Gustavo Yepes, Stefan Gottlöber, and Daniel E. Holz. Toward a Halo Mass

- Function for Precision Cosmology: The Limits of Universality. *ApJ*, 688(2):709–728, Dec 2008. doi: 10.1086/591439.
- Suman Bhattacharya, Katrin Heitmann, Martin White, Zarija Lukić, Christian Wagner, and Salman Habib. Mass Function Predictions Beyond Λ CDM. *ApJ*, 732(2):122, May 2011. doi: 10.1088/0004-637X/732/2/122.
- Ian G. McCarthy, Gilbert P. Holder, Arif Babul, and Michael L. Balogh. The Sunyaev-Zeldovich Effect Signature of Excess Entropy in Distant, Massive Clusters. *ApJ*, 591(2):526–539, July 2003a. doi: 10.1086/375487.
- Ian G. McCarthy, Arif Babul, Gilbert P. Holder, and Michael L. Balogh. Cluster Sunyaev-Zeldovich Effect Scaling Relations. *ApJ*, 591(2):515–525, July 2003b. doi: 10.1086/375486.
- Gregory B. Poole, Arif Babul, Ian G. McCarthy, Mark A. Fardal, C. J. Bildfell, Thomas Quinn, and Andisheh Mahdavi. The impact of mergers on relaxed X-ray clusters - II. Effects on global X-ray and Sunyaev-Zel'dovich properties and their scaling relations. *MNRAS*, 380(2):437–454, September 2007. doi: 10.1111/j.1365-2966.2007.12107.x.
- Henk Hoekstra, Andisheh Mahdavi, Arif Babul, and Chris Bildfell. The Canadian Cluster Comparison Project: weak lensing masses and SZ scaling relations. *MNRAS*, 427(2):1298–1311, December 2012. doi: 10.1111/j.1365-2966.2012.22072.x.
- Andisheh Mahdavi, Henk Hoekstra, Arif Babul, Chris Bildfell, Tesla Jeltema, and J. Patrick Henry. Joint Analysis of Cluster Observations. II. Chandra/XMM-Newton X-Ray and Weak Lensing Scaling Relations for a Sample of 50 Rich Clusters of Galaxies. *ApJ*, 767(2):116, April 2013. doi: 10.1088/0004-637X/767/2/116.
- Ziad Sakr, Stéphane Ilić, Alain Blanchard, Jamal Bittar, and Wehbeh Farah. Cluster counts: Calibration issue or new physics? *A&A*, 620:A78, November 2018. doi: 10.1051/0004-6361/201833151.
- J. A. Peacock and R. E. Smith. Halo occupation numbers and galaxy bias. *MNRAS*, 318(4):1144–1156, Nov 2000. doi: 10.1046/j.1365-8711.2000.03779.x.

- Uroš Seljak. Analytic model for galaxy and dark matter clustering. *MNRAS*, 318(1): 203–213, Oct 2000. doi: 10.1046/j.1365-8711.2000.03715.x.
- Asantha Cooray and Ravi Sheth. Halo models of large scale structure. *Phys. Rep.*, 372(1):1–129, Dec 2002. doi: 10.1016/S0370-1573(02)00276-4.
- A. J. Mead, J. A. Peacock, C. Heymans, S. Joudaki, and A. F. Heavens. An accurate halo model for fitting non-linear cosmological power spectra and baryonic feedback models. *MNRAS*, 454(2):1958–1975, Dec 2015. doi: 10.1093/mnras/stv2036.
- LSST Dark Energy Science Collaboration. Large Synoptic Survey Telescope: Dark Energy Science Collaboration. *arXiv e-prints*, art. arXiv:1211.0310, Nov 2012.
- Luca Amendola, Stephen Appleby, David Bacon, Tessa Baker, Marco Baldi, Nicola Bartolo, Alain Blanchard, Camille Bonvin, Stefano Borgani, Enzo Branchini, Clare Burrage, Stefano Camera, Carmelita Carbone, Luciano Casarini, Mark Cropper, Claudia de Rham, Cinzia Di Porto, Anne Ealet, Pedro G. Ferreira, Fabio Finelli, Juan García-Bellido, Tommaso Giannantonio, Luigi Guzzo, Alan Heavens, Lavinia Heisenberg, Catherine Heymans, Henk Hoekstra, Lukas Hollenstein, Rory Holmes, Ole Horst, Knud Jahnke, Thomas D. Kitching, Tomi Koivisto, Martin Kunz, Giuseppe La Vacca, Marisa March, Elisabetta Majerotto, Katarina Markovic, David Marsh, Federico Marulli, Richard Massey, Yannick Mellier, David F. Mota, Nelson J. Nunes, Will Percival, Valeria Pettorino, Cristiano Porciani, Claudia Quercellini, Justin Read, Massimiliano Rinaldi, Domenico Sapone, Roberto Scaramella, Constantinos Skordis, Fergus Simpson, Andy Taylor, Shaun Thomas, Roberto Trotta, Licia Verde, Filippo Vernizzi, Adrian Vollmer, Yun Wang, Jochen Weller, and Tom Zlosnik. Cosmology and Fundamental Physics with the Euclid Satellite. *Living Reviews in Relativity*, 16(1):6, Sep 2013. doi: 10.12942/lrr-2013-6.
- Dragan Huterer. Weak lensing and dark energy. *Phys. Rev. D*, 65(6):063001, Mar 2002. doi: 10.1103/PhysRevD.65.063001.
- Dragan Huterer and Masahiro Takada. Calibrating the nonlinear matter power spec-

- trum: Requirements for future weak lensing surveys. *Astroparticle Physics*, 23(4): 369–376, May 2005. doi: 10.1016/j.astropartphys.2005.02.006.
- Andrew P. Hearin, Andrew R. Zentner, and Zhaoming Ma. General requirements on matter power spectrum predictions for cosmology with weak lensing tomography. *J. Cosmology Astropart. Phys.*, 2012(4):034, Apr 2012. doi: 10.1088/1475-7516/2012/04/034.
- Marcel P. van Daalen, Joop Schaye, C. M. Booth, and Claudio Dalla Vecchia. The effects of galaxy formation on the matter power spectrum: a challenge for precision cosmology. *MNRAS*, 415(4):3649–3665, Aug 2011. doi: 10.1111/j.1365-2966.2011.18981.x.
- Marco Velliscig, Marcel P. van Daalen, Joop Schaye, Ian G. McCarthy, Marcello Cacciato, Amandine M. C. Le Brun, and Claudio Dalla Vecchia. The impact of galaxy formation on the total mass, mass profile and abundance of haloes. *MNRAS*, 442(3): 2641–2658, Aug 2014. doi: 10.1093/mnras/stu1044.
- Benjamin O. Mummery, Ian G. McCarthy, Simeon Bird, and Joop Schaye. The separate and combined effects of baryon physics and neutrino free streaming on large-scale structure. *MNRAS*, 471(1):227–242, Oct 2017. doi: 10.1093/mnras/stx1469.
- Volker Springel, Rüdiger Pakmor, Annalisa Pillepich, Rainer Weinberger, Dylan Nelson, Lars Hernquist, Mark Vogelsberger, Shy Genel, Paul Torrey, Federico Marinacci, and Jill Naiman. First results from the IllustrisTNG simulations: matter and galaxy clustering. *MNRAS*, 475(1):676–698, March 2018. doi: 10.1093/mnras/stx3304.
- N. E. Chisari, M. L. A. Richardson, J. Devriendt, Y. Dubois, A. Schneider, A. M. C. Le Brun, R. S. Beckmann, S. Peirani, A. Slyz, and C. Pichon. The impact of baryons on the matter power spectrum from the Horizon-AGN cosmological hydrodynamical simulation. *MNRAS*, 480(3):3962–3977, Nov 2018. doi: 10.1093/mnras/sty2093.
- Ian G. McCarthy, Simeon Bird, Joop Schaye, Joachim Harnois-Deraps, Andreea S. Font, and Ludovic van Waerbeke. The BAHAMAS project: the CMB-large-scale

- structure tension and the roles of massive neutrinos and galaxy formation. *MNRAS*, 476:2999–3030, May 2018. doi: 10.1093/mnras/sty377.
- Marcel P. van Daalen, Ian G. McCarthy, and Joop Schaye. Exploring the effects of galaxy formation on matter clustering through a library of simulation power spectra. *MNRAS*, 491(2):2424–2446, Jan 2020. doi: 10.1093/mnras/stz3199.
- Josh Barnes and Piet Hut. A hierarchical $O(N \log N)$ force-calculation algorithm. *Nature*, 324(6096):446–449, December 1986. doi: 10.1038/324446a0.
- R. W. Hockney and J. W. Eastwood. *Computer Simulation Using Particles*. 1981.
- J. P. Morris. A study of the stability properties of smooth particle hydrodynamics. *Publications Astronomical Society of Australia*, 13(1):97–102, January 1996.
- G. A. Dilts. Moving-least-squares-particle hydrodynamics—I. Consistency and stability. *Int. J. Numer. Meth. Engng.*, 44:1115–1155, 1999. doi: doi:10.1002/(SICI)1097-0207(19990320)44:8<1115::AID-NME547>3.0.CO;2-L.
- Benedict W. Ritchie and Peter A. Thomas. Multiphase smoothed-particle hydrodynamics. *MNRAS*, 323(3):743–756, May 2001. doi: 10.1046/j.1365-8711.2001.04268.x.
- S. Marri and S. D. M. White. Smoothed particle hydrodynamics for galaxy-formation simulations: improved treatments of multiphase gas, of star formation and of supernovae feedback. *MNRAS*, 345(2):561–574, October 2003. doi: 10.1046/j.1365-8711.2003.06984.x.
- Takashi Okamoto, Adrian Jenkins, Vincent R. Eke, Vincent Quilis, and Carlos S. Frenk. Momentum transfer across shear flows in smoothed particle hydrodynamic simulations of galaxy formation. *MNRAS*, 345(2):429–446, October 2003. doi: 10.1046/j.1365-8711.2003.06948.x.
- Oscar Agertz, Ben Moore, Joachim Stadel, Doug Potter, Francesco Miniati, Justin Read, Lucio Mayer, Artur Gawryszczak, Andrey Kravtsov, Åke Nordlund, Frazer Pearce, Vicent Quilis, Douglas Rudd, Volker Springel, James Stone, Elizabeth

- Tasker, Romain Teyssier, James Wadsley, and Rolf Walder. Fundamental differences between SPH and grid methods. *MNRAS*, 380(3):963–978, September 2007. doi: 10.1111/j.1365-2966.2007.12183.x.
- S. Kitsionas, C. Federrath, R. S. Klessen, W. Schmidt, D. J. Price, L. J. Dursi, M. Gritschneider, S. Walch, R. Piontek, J. Kim, A. K. Jappsen, P. Ciecielag, and M. M. Mac Low. Algorithmic comparisons of decaying, isothermal, supersonic turbulence. *A&A*, 508(1):541–560, December 2009. doi: 10.1051/0004-6361/200811170.
- Daniel J. Price and Christoph Federrath. A comparison between grid and particle methods on the statistics of driven, supersonic, isothermal turbulence. *MNRAS*, 406(3):1659–1674, August 2010. doi: 10.1111/j.1365-2966.2010.16810.x.
- Andreas Bauer and Volker Springel. Subsonic turbulence in smoothed particle hydrodynamics and moving-mesh simulations. *MNRAS*, 423(3):2558–2578, July 2012. doi: 10.1111/j.1365-2966.2012.21058.x.
- Debora Sijacki, Mark Vogelsberger, Dušan Kereš, Volker Springel, and Lars Hernquist. Moving mesh cosmology: the hydrodynamics of galaxy formation. *MNRAS*, 424(4):2999–3027, August 2012. doi: 10.1111/j.1365-2966.2012.21466.x.
- Daniel J. Price. Modelling discontinuities and Kelvin Helmholtz instabilities in SPH. *Journal of Computational Physics*, 227(24):10040–10057, December 2008. doi: 10.1016/j.jcp.2008.08.011.
- J. W. Wadsley, G. Veeravalli, and H. M. P. Couchman. On the treatment of entropy mixing in numerical cosmology. *MNRAS*, 387(1):427–438, June 2008. doi: 10.1111/j.1365-2966.2008.13260.x.
- Neal Katz, David H. Weinberg, and Lars Hernquist. Cosmological Simulations with TreeSPH. *ApJS*, 105:19, July 1996. doi: 10.1086/192305.
- Volker Springel and Lars Hernquist. Cosmological smoothed particle hydrodynamics simulations: a hybrid multiphase model for star formation. *MNRAS*, 339(2):289–311, February 2003. doi: 10.1046/j.1365-8711.2003.06206.x.

- Maarten Schmidt. The Rate of Star Formation. *ApJ*, 129:243, March 1959. doi: 10.1086/146614.
- Robert P. C. Wiersma, Joop Schaye, Tom Theuns, Claudio Dalla Vecchia, and Luca Tornatore. Chemical enrichment in cosmological, smoothed particle hydrodynamics simulations. *MNRAS*, 399:574–600, October 2009a. doi: 10.1111/j.1365-2966.2009.15331.x.
- Michael L. Balogh, Frazer R. Pearce, Richard G. Bower, and Scott T. Kay. Revisiting the cosmic cooling crisis. *MNRAS*, 326(4):1228–1234, October 2001. doi: 10.1111/j.1365-2966.2001.04667.x.
- Debora Sijacki, Christoph Pfrommer, Volker Springel, and Torsten A. Enßlin. Simulations of cosmic-ray feedback by active galactic nuclei in galaxy clusters. *MNRAS*, 387(4):1403–1415, July 2008. doi: 10.1111/j.1365-2966.2008.13310.x.
- Mark Vogelsberger, Shy Genel, Debora Sijacki, Paul Torrey, Volker Springel, and Lars Hernquist. A model for cosmological simulations of galaxy formation physics. *MNRAS*, 436(4):3031–3067, December 2013. doi: 10.1093/mnras/stt1789.
- Paul Torrey, Mark Vogelsberger, Shy Genel, Debora Sijacki, Volker Springel, and Lars Hernquist. A model for cosmological simulations of galaxy formation physics: multi-epoch validation. *MNRAS*, 438(3):1985–2004, March 2014. doi: 10.1093/mnras/stt2295.
- Robert A. Crain, Joop Schaye, Richard G. Bower, Michelle Furlong, Matthieu Schaller, Tom Theuns, Claudio Dalla Vecchia, Carlos S. Frenk, Ian G. McCarthy, John C. Helly, Adrian Jenkins, Yetli M. Rosas-Guevara, Simon D. M. White, and James W. Trayford. The EAGLE simulations of galaxy formation: calibration of subgrid physics and model variations. *MNRAS*, 450(2):1937–1961, June 2015. doi: 10.1093/mnras/stv725.
- Ian G. McCarthy, Joop Schaye, Simeon Bird, and Amandine M. C. Le Brun. The BAHAMAS project: calibrated hydrodynamical simulations for large-scale structure cosmology. *MNRAS*, 465:2936–2965, March 2017. doi: 10.1093/mnras/stw2792.

- Annalisa Pillepich, Volker Springel, Dylan Nelson, Shy Genel, Jill Naiman, Rüdiger Pakmor, Lars Hernquist, Paul Torrey, Mark Vogelsberger, Rainer Weinberger, and Federico Marinacci. Simulating galaxy formation with the IllustrisTNG model. *MNRAS*, 473(3):4077–4106, January 2018. doi: 10.1093/mnras/stx2656.
- Y. B. Zel'Dovich. Reprint of 1970A&A.....5...84Z. Gravitational instability: an approximate theory for large density perturbations. *A&A*, 500:13–18, March 1970.
- M. Joyce, B. Marcos, A. Gabrielli, T. Baertschiger, and F. Sylos Labini. Gravitational Evolution of a Perturbed Lattice and its Fluid Limit. *Phys. Rev. Lett.*, 95(1):011304, June 2005. doi: 10.1103/PhysRevLett.95.011304.
- Daniel J. Eisenstein. An Analytic Expression for the Growth Function in a Flat Universe with a Cosmological Constant. *arXiv e-prints*, art. astro-ph/9709054, Sep 1997.
- Antony Lewis, Anthony Challinor, and Anthony Lasenby. Efficient computation of CMB anisotropies in closed FRW models. *ApJ*, 538:473–476, 2000. doi: 10.1086/309179.
- Julien Lesgourgues. The Cosmic Linear Anisotropy Solving System (CLASS) I: Overview. *arXiv e-prints*, art. arXiv:1104.2932, April 2011.
- Oliver Hahn and Tom Abel. Multi-scale initial conditions for cosmological simulations. *MNRAS*, 415(3):2101–2121, August 2011. doi: 10.1111/j.1365-2966.2011.18820.x.
- Volker Springel. The cosmological simulation code GADGET-2. *MNRAS*, 364:1105–1134, December 2005. doi: 10.1111/j.1365-2966.2005.09655.x.
- Joop Schaye, Claudio Dalla Vecchia, C. M. Booth, Robert P. C. Wiersma, Tom Theuns, Marcel R. Haas, Serena Bertone, Alan R. Duffy, I. G. McCarthy, and Freeke van de Voort. The physics driving the cosmic star formation history. *MNRAS*, 402:1536–1560, March 2010. doi: 10.1111/j.1365-2966.2009.16029.x.

- Robert P. C. Wiersma, Joop Schaye, and Britton D. Smith. The effect of photoionization on the cooling rates of enriched, astrophysical plasmas. *MNRAS*, 393:99–107, February 2009b. doi: 10.1111/j.1365-2966.2008.14191.x.
- G. J. Ferland, K. T. Korista, D. A. Verner, J. W. Ferguson, J. B. Kingdon, and E. M. Verner. CLOUDY 90: Numerical Simulation of Plasmas and Their Spectra. *PASP*, 110(749):761–778, July 1998. doi: 10.1086/316190.
- F. Haardt and P. Madau. Modelling the UV/X-ray cosmic background with CUBA. In D. M. Neumann and J. T. V. Tran, editors, *Clusters of Galaxies and the High Redshift Universe Observed in X-rays*, page 64, January 2001.
- Joop Schaye and Claudio Dalla Vecchia. On the relation between the Schmidt and Kennicutt-Schmidt star formation laws and its implications for numerical simulations. *MNRAS*, 383:1210–1222, January 2008. doi: 10.1111/j.1365-2966.2007.12639.x.
- Gilles Chabrier. Galactic Stellar and Substellar Initial Mass Function. *PASP*, 115(809): 763–795, July 2003. doi: 10.1086/376392.
- Claudio Dalla Vecchia and Joop Schaye. Simulating galactic outflows with kinetic supernova feedback. *MNRAS*, 387:1431–1444, July 2008. doi: 10.1111/j.1365-2966.2008.13322.x.
- C. M. Booth and Joop Schaye. Simulations of the Growth of Black Holes and Feedback from Active Galactic Nuclei. In Sebastian Heinz and Eric Wilcots, editors, *American Institute of Physics Conference Series*, volume 1201 of *American Institute of Physics Conference Series*, pages 21–24, December 2009. doi: 10.1063/1.3293041.
- Volker Springel, Tiziana Di Matteo, and Lars Hernquist. Modelling feedback from stars and black holes in galaxy mergers. *MNRAS*, 361:776–794, August 2005. doi: 10.1111/j.1365-2966.2005.09238.x.
- M. Davis and P. J. E. Peebles. A survey of galaxy redshifts. V. The two-point position and velocity correlations. *ApJ*, 267:465–482, Apr 1983. doi: 10.1086/160884.

- Volker Springel, Simon D. M. White, Giuseppe Tormen, and Guinevere Kauffmann. Populating a cluster of galaxies - I. Results at $z=0$. *MNRAS*, 328:726–750, December 2001. doi: 10.1046/j.1365-8711.2001.04912.x.
- K. Dolag, S. Borgani, G. Murante, and V. Springel. Substructures in hydrodynamical cluster simulations. *MNRAS*, 399:497–514, October 2009. doi: 10.1111/j.1365-2966.2009.15034.x.
- Sanjib Sharma. Markov Chain Monte Carlo Methods for Bayesian Data Analysis in Astronomy. *ARA&A*, 55(1):213–259, August 2017. doi: 10.1146/annurev-astro-082214-122339.
- Simon Pfeifer, Ian G. McCarthy, Sam G. Stafford, Shaun T. Brown, Andreea S. Font, Juliana Kwan, Jaime Salcido, and Joop Schaye. The BAHAMAS project: Effects of dynamical dark energy on large-scale structure. *arXiv e-prints*, art. arXiv:2004.07670, April 2020.
- Antony Lewis and Sarah Bridle. Cosmological parameters from CMB and other data: A Monte Carlo approach. *Phys. Rev. D*, 66:103511, Nov 2002. doi: 10.1103/PhysRevD.66.103511.
- Planck Collaboration, N. Aghanim, M. Arnaud, M. Ashdown, J. Aumont, C. Baccigalupi, A. J. Banday, R. B. Barreiro, J. G. Bartlett, N. Bartolo, E. Battaner, K. Benabed, A. Benoît, A. Benoit-Lévy, J. P. Bernard, M. Bersanelli, P. Bielewicz, J. J. Bock, A. Bonaldi, L. Bonavera, J. R. Bond, J. Borrill, F. R. Bouchet, F. Boulanger, M. Bucher, C. Burigana, R. C. Butler, E. Calabrese, J. F. Cardoso, A. Catalano, A. Challinor, H. C. Chiang, P. R. Christensen, D. L. Clements, L. P. L. Colombo, C. Combet, A. Coulais, B. P. Crill, A. Curto, F. Cuttaia, L. Danese, R. D. Davies, R. J. Davis, P. de Bernardis, A. de Rosa, G. de Zotti, J. Delabrouille, F. X. Désert, E. Di Valentino, C. Dickinson, J. M. Diego, K. Dolag, H. Dole, S. Donzelli, O. Doré, M. Douspis, A. Ducout, J. Dunkley, X. Dupac, G. Efstathiou, F. Elsner, T. A. Enßlin, H. K. Eriksen, J. Fergusson, F. Finelli, O. Forni, M. Frailis, A. A. Fraisse, E. Franceschi, A. Frejsel, S. Galeotta, S. Galli, K. Ganga, C. Gauthier, M. Gerbino, M. Giard, E. Gjerløw, J. González-Nuevo, K. M. Górski, S. Gratton,

A. Gregorio, A. Gruppuso, J. E. Gudmundsson, J. Hamann, F. K. Hansen, D. L. Harrison, G. Helou, S. Henrot-Versillé, C. Hernández-Monteagudo, D. Herranz, S. R. Hildebrandt, E. Hivon, W. A. Holmes, A. Hornstrup, K. M. Huffenberger, G. Hurier, A. H. Jaffe, W. C. Jones, M. Juvela, E. Keihänen, R. Keskitalo, K. Kivi, J. Knoche, L. Knox, M. Kunz, H. Kurki-Suonio, G. Lagache, A. Lähteenmäki, J. M. Lamarre, A. Lasenby, M. Lattanzi, C. R. Lawrence, M. Le Jeune, R. Leonardi, J. Lesgourgues, F. Levrier, A. Lewis, M. Liguori, P. B. Lilje, M. Lilley, M. Lindén, V. Linder, V. Lindholm, M. López-Cañiego, J. F. Macías-Pérez, B. Maffei, G. Maggio, D. Maino, N. Mandolesi, A. Mangilli, M. Maris, P. G. Martin, E. Martínez-González, S. Masi, S. Matarrese, P. R. Meinhold, A. Melchiorri, M. Migliaccio, M. Millea, S. Mitra, M. A. Miville-Deschênes, A. Moneti, L. Montier, G. Morgante, D. Mortlock, S. Mottet, D. Munshi, J. A. Murphy, A. Narimani, P. Naselsky, F. Nati, P. Natoli, F. Noviello, D. Novikov, I. Novikov, C. A. Oxborrow, F. Paci, L. Pagano, F. Pajot, D. Paoletti, B. Partridge, F. Pasian, G. Patanchon, T. J. Pearson, O. Perdereau, L. Perotto, V. Pettorino, F. Piacentini, M. Piat, E. Pierpaoli, D. Pietrobon, S. Plaszczynski, E. Pointecouteau, G. Polenta, N. Ponthieu, G. W. Pratt, S. Prunet, J. L. Puget, J. P. Rachen, M. Reinecke, M. Remazeilles, C. Renault, A. Renzi, I. Ristorcelli, G. Rocha, M. Rossetti, G. Roudier, B. Rouillé d'Orfeuil, J. A. Rubiño-Martín, B. Rusholme, L. Salvati, M. Sandri, D. Santos, M. Savelainen, G. Savini, D. Scott, P. Serra, L. D. Spencer, M. Spinelli, V. Stolyarov, R. Stompor, R. Sunyaev, D. Sutton, A. S. Suur-Uski, J. F. Sygnet, J. A. Tauber, L. Terenzi, L. Toffolatti, M. Tomasi, M. Tristram, T. Trombetti, M. Tucci, J. Tuovinen, G. Umata, L. Valenziano, J. Valiviita, F. Van Tent, P. Vielva, F. Villa, L. A. Wade, B. D. Wandelt, I. K. Wehus, D. Yvon, A. Zacchei, and A. Zonca. Planck 2015 results. XI. CMB power spectra, likelihoods, and robustness of parameters. *A&A*, 594:A11, Sep 2016a. doi: 10.1051/0004-6361/201526926.

Lauren Anderson, Éric Aubourg, Stephen Bailey, Florian Beutler, Vaishali Bhardwaj, Michael Blanton, Adam S. Bolton, J. Brinkmann, Joel R. Brownstein, Angela Burden, Chia-Hsun Chuang, Antonio J. Cuesta, Kyle S. Dawson, Daniel J. Eisenstein, Stephanie Escoffier, James E. Gunn, Hong Guo, Shirley Ho, Klaus Honscheid, Cul-

- Ian Howlett, David Kirkby, Robert H. Lupton, Marc Manera, Claudia Maraston, Cameron K. McBride, Olga Mena, Francesco Montesano, Robert C. Nichol, Sebastián E. Nuza, Matthew D. Olmstead, Nikhil Padmanabhan, Nathalie Palanque-Delabrouille, John Parejko, Will J. Percival, Patrick Petitjean, Francisco Prada, Adrian M. Price-Whelan, Beth Reid, Natalie A. Roe, Ashley J. Ross, Nicholas P. Ross, Cristiano G. Sabiu, Shun Saito, Lado Samushia, Ariel G. Sánchez, David J. Schlegel, Donald P. Schneider, Claudia G. Scoccola, Hee-Jong Seo, Ramin A. Skibba, Michael A. Strauss, Molly E. C. Swanson, Daniel Thomas, Jeremy L. Tinker, Rita Tojeiro, Mariana Vargas Magaña, Licia Verde, David A. Wake, Benjamin A. Weaver, David H. Weinberg, Martin White, Xiaoying Xu, Christophe Yèche, Idit Zehavi, and Gong-Bo Zhao. The clustering of galaxies in the SDSS-III Baryon Oscillation Spectroscopic Survey: baryon acoustic oscillations in the Data Releases 10 and 11 Galaxy samples. *MNRAS*, 441(1):24–62, Jun 2014. doi: 10.1093/mnras/stu523.
- M. Betoule, R. Kessler, J. Guy, J. Mosser, D. Hardin, R. Biswas, P. Astier, P. El-Hage, M. König, S. Kuhlmann, J. Murrin, R. Pain, N. Regnault, C. Balland, B. A. Bassett, P. J. Brown, H. Campbell, R. G. Carlberg, F. Cellier-Holzem, D. Cinabro, A. Conley, C. B. D’Andrea, D. L. DePoy, M. Doi, R. S. Ellis, S. Fabbro, A. V. Filippenko, R. J. Foley, J. A. Frieman, D. Fouchez, L. Galbany, A. Goobar, R. R. Gupta, G. J. Hill, R. Hlozek, C. J. Hogan, I. M. Hook, D. A. Howell, S. W. Jha, L. Le Guillou, G. Leloudas, C. Lidman, J. L. Marshall, A. Möller, A. M. Mourão, J. Neveu, R. Nichol, M. D. Olmstead, N. Palanque-Delabrouille, S. Perlmutter, J. L. Prieto, C. J. Pritchett, M. Richmond, A. G. Riess, V. Ruhlmann-Kleider, M. Sako, K. Schahmanche, D. P. Schneider, M. Smith, J. Sollerman, M. Sullivan, N. A. Walton, and C. J. Wheeler. Improved cosmological constraints from a joint analysis of the SDSS-II and SNLS supernova samples. *A&A*, 568:A22, Aug 2014. doi: 10.1051/0004-6361/201423413.
- Adam G. Riess, Lucas Macri, Stefano Casertano, Hubert Lampeitl, Henry C. Ferguson, Alexei V. Filippenko, Saurabh W. Jha, Weidong Li, and Ryan Chornock. A 3% Solution: Determination of the Hubble Constant with the Hubble Space Telescope

- and Wide Field Camera 3. *ApJ*, 730(2):119, Apr 2011. doi: 10.1088/0004-637X/730/2/119.
- G. E. Addison, Y. Huang, D. J. Watts, C. L. Bennett, M. Halpern, G. Hinshaw, and J. L. Weiland. Quantifying Discordance in the 2015 Planck CMB Spectrum. *ApJ*, 818:132, February 2016. doi: 10.3847/0004-637X/818/2/132.
- Erminia Calabrese, Anže Slosar, Alessandro Melchiorri, George F. Smoot, and Oliver Zahn. Cosmic microwave weak lensing data as a test for the dark universe. *Phys. Rev. D*, 77(12):123531, Jun 2008. doi: 10.1103/PhysRevD.77.123531.
- Eleonora Di Valentino, Alessandro Melchiorri, and Joseph Silk. Reconciling Planck with the local value of H_0 in extended parameter space. *Physics Letters B*, 761: 242–246, Oct 2016. doi: 10.1016/j.physletb.2016.08.043.
- Fabrizio Renzi, Eleonora Di Valentino, and Alessandro Melchiorri. Cornering the Planck A_{lens} tension with future CMB data. *Phys. Rev. D*, 97(12):123534, Jun 2018. doi: 10.1103/PhysRevD.97.123534.
- Pavel Motloch and Wayne Hu. Tensions between direct measurements of the lens power spectrum from Planck data. *Phys. Rev. D*, 97(10):103536, May 2018. doi: 10.1103/PhysRevD.97.103536.
- Eleonora Di Valentino, Alessandro Melchiorri, and Joseph Silk. Planck evidence for a closed Universe and a possible crisis for cosmology. *Nature Astronomy*, 4:196–203, February 2020a. doi: 10.1038/s41550-019-0906-9.
- E. Macaulay, R. C. Nichol, D. Bacon, D. Brout, T. M. Davis, B. Zhang, B. A. Bassett, D. Scolnic, A. Möller, C. B. D’Andrea, S. R. Hinton, R. Kessler, A. G. Kim, J. Lasker, C. Lidman, M. Sako, M. Smith, M. Sullivan, T. M. C. Abbott, S. Allam, J. Annis, J. Asorey, S. Avila, K. Bechtol, D. Brooks, P. Brown, D. L. Burke, J. Calcinò, A. Carnero Rosell, D. Carollo, M. Carrasco Kind, J. Carretero, F. J. Castander, T. Collett, M. Crocce, C. E. Cunha, L. N. da Costa, C. Davis, J. De Vicente, H. T. Diehl, P. Doel, A. Drlica-Wagner, T. F. Eifler, J. Estrada, A. E. Evrard, A. V. Filippenko, D. A. Finley, B. Flaugher, R. J. Foley, P. Fosalba, J. Frieman, L. Galbany,

- J. García-Bellido, E. Gaztanaga, K. Glazebrook, S. González-Gaitán, D. Gruen, R. A. Gruendl, J. Gschwend, G. Gutierrez, W. G. Hartley, D. L. Hollowood, K. Honscheid, J. K. Hoormann, B. Hoyle, D. Huterer, B. Jain, D. J. James, T. Jeltema, E. Kasai, E. Krause, K. Kuehn, N. Kuropatkin, O. Lahav, G. F. Lewis, T. S. Li, M. Lima, H. Lin, M. A. G. Maia, J. L. Marshall, P. Martini, R. Miquel, P. Nugent, A. Palmese, Y. C. Pan, A. A. Plazas, A. K. Romer, A. Roodman, E. Sanchez, V. Scarpine, R. Schindler, M. Schubnell, S. Serrano, I. Sevilla-Noarbe, R. Sharp, M. Soares-Santos, F. Sobreira, N. E. Sommer, E. Suchyta, E. Swann, M. E. C. Swanson, G. Tarle, D. Thomas, R. C. Thomas, B. E. Tucker, S. A. Uddin, V. Vikram, A. R. Walker, P. Wiseman, and DES Collaboration. First cosmological results using Type Ia supernovae from the Dark Energy Survey: measurement of the Hubble constant. *MNRAS*, 486(2):2184–2196, June 2019. doi: 10.1093/mnras/stz978.
- Robert J. Scherrer and A. A. Sen. Thawing quintessence with a nearly flat potential. *Phys. Rev. D*, 77(8):083515, Apr 2008. doi: 10.1103/PhysRevD.77.083515.
- Takeshi Chiba. Slow-roll thawing quintessence. *Phys. Rev. D*, 79(8):083517, Apr 2009. doi: 10.1103/PhysRevD.79.083517.
- Gaveshna Gupta, Raghavan Rangarajan, and Anjan A. Sen. Thawing quintessence from the inflationary epoch to today. *Phys. Rev. D*, 92(12):123003, Dec 2015. doi: 10.1103/PhysRevD.92.123003.
- Robert J. Scherrer. Dark energy models in the w - w' plane. *Phys. Rev. D*, 73(4):043502, Feb 2006. doi: 10.1103/PhysRevD.73.043502.
- Takeshi Chiba. w and w' of scalar field models of dark energy. *Phys. Rev. D*, 73(6):063501, Mar 2006. doi: 10.1103/PhysRevD.73.063501.
- Martin Sahlén, Andrew R. Liddle, and David Parkinson. Quintessence reconstructed: New constraints and tracker viability. *Phys. Rev. D*, 75(2):023502, Jan 2007. doi: 10.1103/PhysRevD.75.023502.
- E. V. Linder and A. Jenkins. Cosmic structure growth and dark energy. *MNRAS*, 346(2):573–583, Dec 2003a. doi: 10.1046/j.1365-2966.2003.07112.x.

Kenneth C. Wong, Sherry H. Suyu, Geoff C. F. Chen, Cristian E. Rusu, Martin Millon, Dominique Sluse, Vivien Bonvin, Christopher D. Fassnacht, Stefan Taubenberger, Matthew W. Auger, Simon Birrer, James H. H. Chan, Frederic Courbin, Stefan Hilbert, Olga Tihhonova, Tommaso Treu, Adriano Agnello, Xuheng Ding, Inh Jee, Eiichiro Komatsu, Anowar J. Shajib, Alessandro Sonnenfeld, Roger D. Blandford, Leon V. E. Koopmans, Philip J. Marshall, and Georges Meylan. H0LiCOW XIII. A 2.4% measurement of H_0 from lensed quasars: 5.3σ tension between early and late-Universe probes. *arXiv e-prints*, art. arXiv:1907.04869, Jul 2020.

Planck Collaboration, P. A. R. Ade, N. Aghanim, M. Arnaud, M. Ashdown, J. Aumont, C. Baccigalupi, A. J. Banday, R. B. Barreiro, J. G. Bartlett, N. Bartolo, E. Battaner, R. Battye, K. Benabed, A. Benoît, A. Benoit-Lévy, J. P. Bernard, M. Bersanelli, P. Bielewicz, J. J. Bock, A. Bonaldi, L. Bonavera, J. R. Bond, J. Borrill, F. R. Bouchet, M. Bucher, C. Burigana, R. C. Butler, E. Calabrese, J. F. Cardoso, A. Catalano, A. Challinor, A. Chamballu, R. R. Chary, H. C. Chiang, P. R. Christensen, S. Church, D. L. Clements, S. Colombi, L. P. L. Colombo, C. Combet, B. Comis, F. Couchot, A. Coulais, B. P. Crill, A. Curto, F. Cuttaia, L. Danese, R. D. Davies, R. J. Davis, P. de Bernardis, A. de Rosa, G. de Zotti, J. Delabrouille, F. X. Désert, J. M. Diego, K. Dolag, H. Dole, S. Donzelli, O. Doré, M. Douspis, A. Ducout, X. Dupac, G. Efstathiou, F. Elsner, T. A. Enßlin, H. K. Eriksen, E. Falgarone, J. Fergusson, F. Finelli, O. Forni, M. Frailis, A. A. Fraisse, E. Franceschi, A. Frejsel, S. Galeotta, S. Galli, K. Ganga, M. Giard, Y. Giraud-Héraud, E. Gjerløw, J. González-Nuevo, K. M. Górski, S. Gratton, A. Gregorio, A. Gruppuso, J. E. Gudmundsson, F. K. Hansen, D. Hanson, D. L. Harrison, S. Henrot-Versillé, C. Hernández-Monteagudo, D. Herranz, S. R. Hildebrandt, E. Hivon, M. Hobson, W. A. Holmes, A. Hornstrup, W. Hovest, K. M. Huffenberger, G. Hurier, A. H. Jaffe, T. R. Jaffe, W. C. Jones, M. Juvela, E. Keihänen, R. Keskitalo, T. S. Kisner, R. Kneissl, J. Knoche, M. Kunz, H. Kurki-Suonio, G. Lagache, A. Lähteenmäki, J. M. Lamarre, A. Lasenby, M. Lattanzi, C. R. Lawrence, R. Leonardi, J. Lesgourgues, F. Levrier, M. Liguori, P. B. Lilje, M. Linden-Vørnle, M. López-Caniego, P. M. Lubin, J. F. Macías-Pérez, G. Maggio, D. Maino, N. Mand

olesi, A. Mangilli, M. Maris, P. G. Martin, E. Martínez-González, S. Masi, S. Matarrese, P. McGehee, P. R. Meinhold, A. Melchiorri, J. B. Melin, L. Mendes, A. Mennella, M. Migliaccio, S. Mitra, M. A. Miville-Deschênes, A. Moneti, L. Montier, G. Morgante, D. Mortlock, A. Moss, D. Munshi, J. A. Murphy, P. Naselsky, F. Nati, P. Natoli, C. B. Netterfield, H. U. Nørgaard-Nielsen, F. Noviello, D. Novikov, I. Novikov, C. A. Oxborrow, F. Paci, L. Pagano, F. Pajot, D. Paoletti, B. Partridge, F. Pasian, G. Patanchon, T. J. Pearson, O. Perdureau, L. Perotto, F. Perrotta, V. Pettorino, F. Piacentini, M. Piat, E. Pierpaoli, D. Pietrobon, S. Plaszczynski, E. Pointecouteau, G. Polenta, L. Popa, G. W. Pratt, G. Prézeau, S. Prunet, J. L. Puget, J. P. Rachen, R. Rebolo, M. Reinecke, M. Remazeilles, C. Renault, A. Renzi, I. Ristorcelli, G. Rocha, M. Roman, C. Rosset, M. Rossetti, G. Roudier, J. A. Rubiño-Martín, B. Rusholme, M. Sandri, D. Santos, M. Savelainen, G. Savini, D. Scott, M. D. Seiffert, E. P. S. Shellard, L. D. Spencer, V. Stolyarov, R. Stompor, R. Sudiwala, R. Sunyaev, D. Sutton, A. S. Suur-Uski, J. F. Sygnet, J. A. Tauber, L. Terenzi, L. Toffolatti, M. Tomasi, M. Tristram, M. Tucci, J. Tuovinen, M. Türlér, G. Umata, L. Valenziano, J. Valiviita, B. Van Tent, P. Vielva, F. Villa, L. A. Wade, B. D. Wandelt, I. K. Wehus, J. Weller, S. D. M. White, D. Yvon, A. Zacchei, and A. Zonca. Planck 2015 results. XXIV. Cosmology from Sunyaev-Zeldovich cluster counts. *A&A*, 594:A24, Sep 2016b. doi: 10.1051/0004-6361/201525833.

Alexie Leauthaud, Shun Saito, Stefan Hilbert, Alexandre Barreira, Surhud More, Martin White, Shadab Alam, Peter Behroozi, Kevin Bundy, Jean Coupon, Thomas Erben, Catherine Heymans, Hendrik Hildebrandt, Rachel Mandelbaum, Lance Miller, Bruno Moraes, Maria E. S. Pereira, Sergio A. Rodríguez-Torres, Fabian Schmidt, Huan-Yuan Shan, Matteo Viel, and Francisco Villaescusa-Navarro. Lensing is low: cosmology, galaxy formation or new physics? *MNRAS*, 467(3):3024–3047, May 2017. doi: 10.1093/mnras/stx258.

H. Hildebrandt, F. Köhlinger, J. L. van den Busch, B. Joachimi, C. Heymans, A. Kannawadi, A. H. Wright, M. Asgari, C. Blake, H. Hoekstra, S. Joudaki, K. Kuijken, L. Miller, C. B. Morrison, T. Tröster, A. Amon, M. Archidiacono, S. Brieden, A. Choi, J. T. A. de Jong, T. Erben, B. Giblin, A. Mead, J. A. Pea-

- cock, M. Radovich, P. Schneider, C. Sifón, and M. Tewes. KiDS+VIKING-450: Cosmic shear tomography with optical and infrared data. *A&A*, 633:A69, Jan 2020. doi: 10.1051/0004-6361/201834878.
- Baojiu Li, Gong-Bo Zhao, Romain Teyssier, and Kazuya Koyama. ECOSMOG: an Efficient COde for Simulating MODified Gravity. *J. Cosmology Astropart. Phys.*, 2012(1):051, Jan 2012. doi: 10.1088/1475-7516/2012/01/051.
- David F. Mota. Probing screened modified gravity with nonlinear structure formation. *International Journal of Modern Physics D*, 27(4):1830003, Jan 2018. doi: 10.1142/S0218271818300033.
- Sam G. Stafford, Ian G. McCarthy, Robert A. Crain, Jaime Salcido, Joop Schaye, Andreea S. Font, Juliana Kwan, and Simon Pfeifer. The BAHAMAS project: Effects of a running scalar spectral index on large-scale structure. *MNRAS*, *in press*, art. arXiv:1907.09497, Jul 2020.
- Simeon Bird. GenPK: Power spectrum generator, June 2017.
- Aurel Schneider, Romain Teyssier, Joachim Stadel, Nora Elisa Chisari, Amandine M. C. Le Brun, Adam Amara, and Alexandre Refregier. Quantifying baryon effects on the matter power spectrum and the weak lensing shear correlation. *J. Cosmology Astropart. Phys.*, 2019(3):020, March 2019. doi: 10.1088/1475-7516/2019/03/020.
- Stijn N. B. Debackere, Joop Schaye, and Henk Hoekstra. The impact of the observed baryon distribution in haloes on the total matter power spectrum. *MNRAS*, 492(2): 2285–2307, February 2020. doi: 10.1093/mnras/stz3446.
- Benedikt Diemer and Andrey V. Kravtsov. Dependence of the Outer Density Profiles of Halos on Their Mass Accretion Rate. *ApJ*, 789(1):1, July 2014. doi: 10.1088/0004-637X/789/1/1.
- C. Power, J. F. Navarro, A. Jenkins, C. S. Frenk, S. D. M. White, V. Springel, J. Stadel, and T. Quinn. The inner structure of Λ CDM haloes - I. A numerical convergence study. *MNRAS*, 338(1):14–34, January 2003. doi: 10.1046/j.1365-8711.2003.05925.x.

- Aaron D. Ludlow, Joop Schaye, and Richard Bower. Numerical convergence of simulations of galaxy formation: the abundance and internal structure of cold dark matter haloes. *MNRAS*, 488(3):3663–3684, September 2019. doi: 10.1093/mnras/stz1821.
- A. Savitzky and M. J. E. Golay. Smoothing and differentiation of data by simplified least squares procedures. *Analytical Chemistry*, 36:1627–1639, January 1964.
- J. S. Bullock, T. S. Kolatt, Y. Sigad, R. S. Somerville, A. V. Kravtsov, A. A. Klypin, J. R. Primack, and A. Dekel. Profiles of dark haloes: evolution, scatter and environment. *MNRAS*, 321:559–575, Mar 2001. doi: 10.1046/j.1365-8711.2001.04068.x.
- Vincent R. Eke, Julio F. Navarro, and Matthias Steinmetz. The Power Spectrum Dependence of Dark Matter Halo Concentrations. *ApJ*, 554:114–125, Jun 2001. doi: 10.1086/321345.
- Julio F. Navarro, Carlos S. Frenk, and Simon D. M. White. A Universal Density Profile from Hierarchical Clustering. *ApJ*, 490:493–508, Dec 1997. doi: 10.1086/304888.
- Andrea V. Macciò, Aaron A. Dutton, Frank C. van den Bosch, Ben Moore, Doug Potter, and Joachim Stadel. Concentration, spin and shape of dark matter haloes: scatter and the dependence on mass and environment. *MNRAS*, 378(1):55–71, Jun 2007. doi: 10.1111/j.1365-2966.2007.11720.x.
- Emilio Romano-Díaz, Yehuda Hoffman, Clayton Heller, Andreas Faltenbacher, Daniel Jones, and Isaac Shlosman. Evolution of Characteristic Quantities for Dark Matter Halo Density Profiles. *ApJ*, 657(1):56–70, Mar 2007. doi: 10.1086/509798.
- Angelo F. Neto, Liang Gao, Philip Bett, Shaun Cole, Julio F. Navarro, Carlos S. Frenk, Simon D. M. White, Volker Springel, and Adrian Jenkins. The statistics of Λ CDM halo concentrations. *MNRAS*, 381:1450–1462, Nov 2007. doi: 10.1111/j.1365-2966.2007.12381.x.
- Alan R. Duffy, Joop Schaye, Scott T. Kay, and Claudio Dalla Vecchia. Dark matter halo concentrations in the Wilkinson Microwave Anisotropy Probe year 5 cosmology. *MNRAS*, 390(1):L64–L68, Oct 2008. doi: 10.1111/j.1745-3933.2008.00537.x.

- Eleonora Di Valentino, Alessandro Melchiorri, and Joseph Silk. Cosmological constraints in extended parameter space from the Planck 2018 Legacy release. *J. Cosmology Astropart. Phys.*, 2020(1):013, January 2020b. doi: 10.1088/1475-7516/2020/01/013.
- Amol Upadhye. Neutrino mass and dark energy constraints from redshift-space distortions. *J. Cosmology Astropart. Phys.*, 2019(5):041, May 2019. doi: 10.1088/1475-7516/2019/05/041.
- Chung-Pei Ma, R. R. Caldwell, Paul Bode, and Limin Wang. The Mass Power Spectrum in Quintessence Cosmological Models. *ApJl*, 521(1):L1–L4, Aug 1999. doi: 10.1086/312183.
- Paul Bode, Neta A. Bahcall, Eric B. Ford, and Jeremiah P. Ostriker. Evolution of the Cluster Mass Function: GPC³ Dark Matter Simulations. *ApJ*, 551(1):15–22, Apr 2001. doi: 10.1086/320077.
- Ewa L. Łokas, Paul Bode, and Yehuda Hoffman. Cluster mass functions in the quintessential universe. *MNRAS*, 349(2):595–602, Apr 2004. doi: 10.1111/j.1365-2966.2004.07529.x.
- A. Klypin, A. V. Macciò, R. Mainini, and S. A. Bonometto. Halo Properties in Models with Dynamical Dark Energy. *ApJ*, 599(1):31–37, Dec 2003. doi: 10.1086/379237.
- E. V. Linder and A. Jenkins. Cosmic structure growth and dark energy. *MNRAS*, 346(2):573–583, Dec 2003b. doi: 10.1046/j.1365-2966.2003.07112.x.
- Marco Baldi. Dark Energy simulations. *Physics of the Dark Universe*, 1(1-2):162–193, Nov 2012. doi: 10.1016/j.dark.2012.10.004.
- Matthew J. Francis, Geraint F. Lewis, and Eric V. Linder. Can early dark energy be detected in non-linear structure? *MNRAS*, 394(2):605–614, April 2009. doi: 10.1111/j.1365-2966.2008.14286.x.
- J. Courtin, Y. Rasera, J. M. Alimi, P. S. Corasaniti, V. Boucher, and A. Füzfa. Imprints of dark energy on cosmic structure formation - II. Non-universality of the halo mass

- function. *MNRAS*, 410(3):1911–1931, Jan 2011. doi: 10.1111/j.1365-2966.2010.17573.x.
- Rahul Biswas, Katrin Heitmann, Salman Habib, Amol Upadhye, Adrian Pope, and Nicholas Frontiere. Effects of Massive Neutrinos and Dynamical Dark Energy on the Cluster Mass Function. *arXiv e-prints*, art. arXiv:1901.10690, Jan 2019.
- Luciano Casarini, Andrea V. Macciò, and Silvio A. Bonometto. Dynamical dark energy simulations: high accuracy power spectra at high redshift. *J. Cosmology Astropart. Phys.*, 2009(3):014, Mar 2009. doi: 10.1088/1475-7516/2009/03/014.
- J. M. Alimi, A. Füzfa, V. Boucher, Y. Rasera, J. Courtin, and P. S. Corasaniti. Imprints of dark energy on cosmic structure formation - I. Realistic quintessence models and the non-linear matter power spectrum. *MNRAS*, 401(2):775–790, Jan 2010. doi: 10.1111/j.1365-2966.2009.15712.x.
- Katrin Heitmann, Martin White, Christian Wagner, Salman Habib, and David Higdon. The Coyote Universe. I. Precision Determination of the Nonlinear Matter Power Spectrum. *ApJ*, 715(1):104–121, May 2010. doi: 10.1088/0004-637X/715/1/104.
- M. Cataneo, L. Lombriser, C. Heymans, A. J. Mead, A. Barreira, S. Bose, and B. Li. On the road to percent accuracy: non-linear reaction of the matter power spectrum to dark energy and modified gravity. *MNRAS*, 488(2):2121–2142, Sep 2019. doi: 10.1093/mnras/stz1836.
- Juliana Kwan, Suman Bhattacharya, Katrin Heitmann, and Salman Habib. Cosmic Emulation: The Concentration-Mass Relation for w CDM Universes. *ApJ*, 768(2):123, May 2013. doi: 10.1088/0004-637X/768/2/123.
- Katrin Heitmann, Earl Lawrence, Juliana Kwan, Salman Habib, and David Higdon. The Coyote Universe Extended: Precision Emulation of the Matter Power Spectrum. *ApJ*, 780(1):111, Jan 2014. doi: 10.1088/0004-637X/780/1/111.
- Mischa Knabenhans, Joachim Stadel, Stefano Marelli, Doug Potter, Romain Teyssier, Laurent Legrand, Aurel Schneider, Bruno Sudret, Linda Blot, Saeeda Awan, Carlo

- Burigana, Carla Sofia Carvalho, Hannu Kurki-Suonio, Gabriele Sirri, and Euclid Collaboration. Euclid preparation: II. The EUCLIDEMULATOR - a tool to compute the cosmology dependence of the nonlinear matter power spectrum. *MNRAS*, 484(4):5509–5529, Apr 2019. doi: 10.1093/mnras/stz197.
- Joachim Harnois-Deraps, Ben Giblin, and Benjamin Joachimi. Cosmic Shear Covariance Matrix in w CDM: Cosmology Matters. *arXiv e-prints*, art. arXiv:1905.06454, May 2019.
- C. Penzo, A. V. Macciò, L. Casarini, G. S. Stinson, and J. Wadsley. Dark MaGICC: the effect of dark energy on disc galaxy formation. Cosmology does matter. *MNRAS*, 442(1):176–186, Jul 2014. doi: 10.1093/mnras/stu857.
- U. Maio, K. Dolag, M. Meneghetti, L. Moscardini, N. Yoshida, C. Baccigalupi, M. Bartelmann, and F. Perrotta. Early structure formation in quintessence models and its implications for cosmic reionization from first stars. *MNRAS*, 373(2): 869–878, Dec 2006. doi: 10.1111/j.1365-2966.2006.11090.x.
- Till Sawala, Carlos S. Frenk, Robert A. Crain, Adrian Jenkins, Joop Schaye, Tom Theuns, and Jesus Zavala. The abundance of (not just) dark matter haloes. *MNRAS*, 431(2):1366–1382, May 2013. doi: 10.1093/mnras/stt259.
- Sam J. Cusworth, Scott T. Kay, Richard A. Battye, and Peter A. Thomas. Impact of baryons on the cluster mass function and cosmological parameter determination. *MNRAS*, 439(3):2485–2493, Apr 2014. doi: 10.1093/mnras/stu105.
- Marcel P. van Daalen, Joop Schaye, Ian G. McCarthy, C. M. Booth, and Claudio Dalla Vecchia. The impact of baryonic processes on the two-point correlation functions of galaxies, subhaloes and matter. *MNRAS*, 440(4):2997–3010, June 2014. doi: 10.1093/mnras/stu482.
- Alan R. Duffy, Joop Schaye, Scott T. Kay, Claudio Dalla Vecchia, Richard A. Battye, and C. M. Booth. Impact of baryon physics on dark matter structures: a detailed simulation study of halo density profiles. *MNRAS*, 405(4):2161–2178, July 2010. doi: 10.1111/j.1365-2966.2010.16613.x.

- Matthieu Schaller, Carlos S. Frenk, Richard G. Bower, Tom Theuns, Adrian Jenkins, Joop Schaye, Robert A. Crain, Michelle Furlong, Claudio Dalla Vecchia, and I. G. McCarthy. Baryon effects on the internal structure of Λ CDM haloes in the EAGLE simulations. *MNRAS*, 451(2):1247–1267, Aug 2015. doi: 10.1093/mnras/stv1067.
- Jonathan J. Davies, Robert A. Crain, Ian G. McCarthy, Benjamin D. Oppenheimer, Joop Schaye, Matthieu Schaller, and Stuart McAlpine. The gas fractions of dark matter haloes hosting simulated $\sim L^*$ galaxies are governed by the feedback history of their black holes. *MNRAS*, 485(3):3783–3793, May 2019. doi: 10.1093/mnras/stz635.
- A. J. Mead, C. Heymans, L. Lombriser, J. A. Peacock, O. I. Steele, and H. A. Winther. Accurate halo-model matter power spectra with dark energy, massive neutrinos and modified gravitational forces. *MNRAS*, 459(2):1468–1488, Jun 2016. doi: 10.1093/mnras/stw681.
- Weiguang Cui, Stefano Borgani, and Giuseppe Murante. The effect of active galactic nuclei feedback on the halo mass function. *MNRAS*, 441(2):1769–1782, Jun 2014. doi: 10.1093/mnras/stu673.
- Earl Lawrence, Katrin Heitmann, Juliana Kwan, Amol Upadhye, Derek Bingham, Salman Habib, David Higdon, Adrian Pope, Hal Finkel, and Nicholas Frontiere. The Mira-Titan Universe. II. Matter Power Spectrum Emulation. *ApJ*, 847(1):50, September 2017. doi: 10.3847/1538-4357/aa86a9.
- Euclid Collaboration, Mischa Knabenhans, Joachim Stadel, Stefano Marelli, Doug Potter, Romain Teyssier, Laurent Legrand, Aurel Schneider, Bruno Sudret, Linda Blot, Saeeda Awan, Carlo Burigana, Carla Sofia Carvalho, Hannu Kurki-Suonio, and Gabriele Sirri. Euclid preparation: II. The EUCLIDEMULATOR - a tool to compute the cosmology dependence of the nonlinear matter power spectrum. *MNRAS*, 484(4):5509–5529, April 2019. doi: 10.1093/mnras/stz197.
- Juliana Kwan, Katrin Heitmann, Salman Habib, Nikhil Padmanabhan, Earl Lawrence, Hal Finkel, Nicholas Frontiere, and Adrian Pope. Cosmic Emulation: Fast Pre-

dictions for the Galaxy Power Spectrum. *ApJ*, 810(1):35, September 2015. doi: 10.1088/0004-637X/810/1/35.

Zhongxu Zhai, Jeremy L. Tinker, Matthew R. Becker, Joseph DeRose, Yao-Yuan Mao, Thomas McClintock, Sean McLaughlin, Eduardo Rozo, and Risa H. Wechsler. The Aemulus Project. III. Emulation of the Galaxy Correlation Function. *ApJ*, 874(1): 95, March 2019. doi: 10.3847/1538-4357/ab0d7b.